Swansea University E-Theses

Surface characterisation of ZnO nanowires.

Barnett, Christopher Jonathan

How to cite:

Barnett, Christopher Jonathan (2015) *Surface characterisation of ZnO nanowires..* thesis, Swansea University.
http://cronfa.swan.ac.uk/Record/cronfa43027

Use policy:

This item is brought to you by Swansea University. Any person downloading material is agreeing to abide by the terms of the repository licence: copies of full text items may be used or reproduced in any format or medium, without prior permission for personal research or study, educational or non-commercial purposes only. The copyright for any work remains with the original author unless otherwise specified. The full-text must not be sold in any format or medium without the formal permission of the copyright holder. Permission for multiple reproductions should be obtained from the original author.

Authors are personally responsible for adhering to copyright and publisher restrictions when uploading content to the repository.

Please link to the metadata record in the Swansea University repository, Cronfa (link given in the citation reference above.)

http://www.swansea.ac.uk/library/researchsupport/ris-support/

Surface Characterisation of ZnO Nanowires

Christopher Jonathan Barnett

Submitted to Swansea University in fulfilment of the requirements for the Degree of Doctor of Philosophy

Swansea University

2015

ProQuest Number: 10821417

All rights reserved

INFORMATION TO ALL USERS
The quality of this reproduction is dependent upon the quality of the copy submitted.

In the unlikely event that the author did not send a complete manuscript
and there are missing pages, these will be noted. Also, if material had to be removed,
a note will indicate the deletion.

ProQuest 10821417

Published by ProQuest LLC (2018). Copyright of the Dissertation is held by the Author.

All rights reserved.
This work is protected against unauthorized copying under Title 17, United States Code
Microform Edition © ProQuest LLC.

ProQuest LLC.
789 East Eisenhower Parkway
P.O. Box 1346
Ann Arbor, MI 48106 – 1346

Abstract

Zinc oxide nanowires have received increased scientific attention in research years due to their novel properties and potential applications. One of the main features of these nanostructures that makes them attractive for devices such as bio and gas sensors is the large surface area to volume ratio which leads to the dominance of surface interactions. In this work ZnO nanowires have been synthesised aqueously and the effects of altering the initial growth conditions have been investigated. The nanowires have also had their surface characterised using STM and local transport measurements taken. STM is the most surface sensitive method of characterising a surface however in order to take these measurements both the surface of the nanostructures and the tungsten probe needs to be cleaned. Work has also be carried out to improve local probe measurements by creating a direct current annealing method to remove probe oxide and investigate the effect of the probe oxide on STS and contact measurements. The effects of the cleaning treatment have also been characterised using STS, two point probe, PL and XPS. It was found that the main defects present in untreated ZnO nanostructures are oxygen vacancies and are responsible for ZnO's n-type nature. It was seen that a light argon bombardment cleans the surface of impurities. It has also been found that the defects are mainly concentrated on the surface of the nanowires and that argon bombardment can remove the surface which reduces the number of defects observed with PL and increases the measured resistance. Similar results were also observed when annealing ZnO nanostructures with low temperature annealing removing surface contaminates and further annealing removing the surface via melting. This work has resulted in an effective method achieving near atomic resolution and methods of improving electrical contacts on ZnO nanostructures.

Declaration

This work has not previously been accepted in substance for any degree and is not being concurrently submitted in candidature for any degree.

Signed .... (candidate)

Date 17/11/15

STATEMENT 1

This thesis is the result of my own investigations, except where otherwise stated. Where correction services have been used, the extent and nature of the correction is clearly marked in a footnote(s).

Other sources are acknowledged by footnotes giving explicit references. A bibliography is appended.

Signed . ... (candidate)

Date 17/11/15

STATEMENT 2

I hereby give consent for my thesis, if accepted, to be available for photocopying and for inter-library loan, and for the title and summary to be made available to outside organisations.

Signed .. .. (candidate)

Date 17/11/15

Contents Page

	Page
Abstract	i
Declaration	ii
Contents Page	iii
Permissions	iv
List of Acronyms	v
Acknowledgements	vi
Chapter 1: Introduction	1
Chapter 2: Literature Review	5
Chapter 3: Scientific Methods	25
Chapter 4: Tip Oxide Effect	62
Chapter 5: Zinc Oxide Nanowire Growth	78
Chapter 6: Characterisation of ZnO Nanostructures	106
Chapter 7: Conclusions and Further Work	146
References	152

Permissions

Figure 2.1: Permission obtained from Elservier

Figure 2.2: Permission obtained from Elservier

Figure 2.3: Permission obtained from Elservier

Figure 2.4: Permission obtained from Elservier

Figure 2.5: Permission obtained from IOP Nanotechnology and the Author

All other figures do not require permission.

List of Acronyms

AES	Auger Electron Spectroscopy
AFM	Atomic Force Microscopy
BSEs	Back Scattered Electrons
CB	Conduction Band
EDX	Energy Dispersive X-ray Spectroscopy
HMTA	Hexamethylmelamine
LEED	Low Energy Electron Diffraction
NBE	Near Band Edge
PL	Photoluminescence
SAM	Scanning Auger Microscopy
SEM	Scanning Electron Microscopy
SEs	Secondary Electrons
STM	Scanning Tunnelling Microscopy
STEM	Scanning Transmission Electron Microscopy
STS	Scanning Tunnelling Spectroscopy
TEM	Transmission Electron Microscopy
VB	Valence Band
XPS	X-ray Photoelectron Spectroscopy
ZnO	Zinc Oxide

Acknowledgements

I would like to thank Dr Richard Cobley and Dr Thierry Maffeis for their advice, guidance and support throughout the completion of this thesis. I should also like to acknowledge and thank Dr Olga Kryvchenkova for her simulation work, Dr Nathan Smith for his expertise on the Nanoprobe, Dr Daniel Jones for his nanosheets contributions and Mr Luke Wilson, Mr Liam Kelleher, Dr Jon Evans and Dr Richard Brown for their assistance throughout this project.

This work was funded through an EPSRC studentship.

Chapter 1: Introduction

Zinc oxide (ZnO) is a transparent metal oxide wide direct band gap semiconductor, 3.37 eV at room temperature, which displays piezo electric properties due to its wurtzite structure [1]. ZnO has been used in number of devices such as gas sensors, field emission transistors and laser diodes [2]. ZnO nanowires have been the subject of much attention in recent years with both their fundamental properties and application being researched. The small size of nanowires mean that they have enhanced sensing capabilities but still allow contacts to be made to them so they can be incorporated into devices such as FETs, bio sensors, chemical sensors and nano-generators.

One of the main features of nano-science is the transition of bulk dominated effects to surface dominated effects as surface to volume ratio increases as the dimensions of a structure are decreased. Therefore it is important to understand the surface of ZnO nanowires so that they can be more efficiently used in devices. One of the most surface sensitive techniques available to study nanostructure surfaces is scanning tunnelling microscopy (STM). An explanation of STM and other techniques: low energy electron diffraction (LEED), x-ray photoelectron spectroscopy (XPS), scanning electron microscopy (SEM) and photoluminescence (PL), used in this thesis is given in Chapter 3. Although the atoms of the wurtzite structure have been seen using super scanning transmission microscopy (STEM) [3], atomic resolution of a ZnO nanowire has not been achieved using STM, even though several groups have attempted it [4, 5]. A literature review of experiments carried out using STM on ZnO in presented in Chapter 2. This thesis describes experiments carried out to take surface and low-dimensional measurements on ZnO nanowires and later nanosheets.

To achieve the overall goals of local transport measurements and atomic resolution using STM on ZnO nanowires three main objectives need to be attained. The first is optimising the STM system so that it has the best chance to achieve a steady image. The vital, controllable part of an STM system are the probes which are chemically

etched to form a near atomically sharp tip. STM probes are made from tungsten which forms a native oxide when it is exposed to air. This oxide is known to have a detrimental effect on stability of the tunnelling current. Chapter 4 covers a series of experiments which are based around making tungsten STM probes consistent by removing the native oxide. There are several methods available to remove the oxide once the tip is in the STM UHV system [6-10]. Here a method of direct current annealing is used to clean the tip by using a modified Omicron tip transfer plate which was first carried out by Yu et al. [11]. The first experiment covers annealing the tip using increasing currents; after each treatment the tip was removed from the UHV system and characterised using SEM to measure tip diameter and EDX to measure the tungsten to oxygen ratio. The second experiment examines the effect of the oxide coating on the STS spectra. Tips were loaded into the STM system and used to obtain STS spectra on cleaved GaAS. The tips were then cleaned using direct current annealing using the recipe found in the first part of the experiment. The STS spectra were then taken again and compared to the original spectra. Modelling, carried out by Olga Kryvchenkova [12], was then implemented to explain the difference and understand how the oxide coating affects the tunnelling. The final experiment examines the effects of tip oxide on contact measurement such as 2 point probe which has been implemented to measure the electrical properties of ZnO nanowires in Chapter 6. This contact experiment is a repeat of the second experiment, however, this time the tip is brought into contact with the sample and I-V measurements taken.

The second goal is to grow suitable ZnO nanowires by creating a recipe for growth which produces nanowires that are broad and long so that the STM tip can be landed onto them to enable a scan to be carried out. In order to achieve this, five variables of aqueous growth are examined in Chapter 5: precursor ratio, temperature of synthesis, time of synthesis, substrate material and growth technique. SEM was used to characterise any changes. The first experiment examines the effect of changing the precursor ratio which Sugunan et al. [13] predict will change the diameter of the ZnO nanowires due to the use of hexamethylmelamine (HMTA). The second experiment examines the effect of growth temperature which should alter the growth rate. This experiment also implements PL to examine whether the growth rate

affects the number of defects present. The third experiment examines how the time of growth affects the ZnO nanowires. It is fairly clear that increasing the growth time will increase the length of the nanowires. However, it is not known how long the solution will stay in saturation and whether the growth will continue indefinitely. This experiment will also examine whether the growth is continuous or whether there are stages that affect both the length and diameter. The final experiment in Chapter 5 covers two variables: substrate and growth type. The experiment continues work carried out by Brown et al. [14] who deposited different metals using the ZnO seed layer. Here, a layer of titanium, chromium or tungsten was deposited before the seed layer then the resulting growth characterised. The work published by Brown et al. found that the metal layer changed the grain size and roughness of the seed layer which altered the morphology of the ZnO nanowires grown [14]. The experiment was repeated using a microwave instead of a water bath to ascertain if microwave synthesis is more efficient than bath growth.

The third factor to achieve atomic resolution on a ZnO nanowire is to adapt the cleaning recipe. Since many of the applications of ZnO nanowires rely on the surface it is important and to understand the effects of the treatment on the surface. Chapter 6 is the final experimental chapter and uses the results from the previous chapters to try to achieve atomic resolution on ZnO nanowires and take local transport measurements. The first experiment covers trying to reproduce the results obtained by Dulub et al. [15] who achieved near atomic resolution using STM on single crystal ZnO by removing surface contaminants and to obtain a surface reconstruction using argon bombardment and annealing. This experiment was not successful since a clear LEED pattern was not obtained. The second and third experiments study the effects of heating and argon bombardment on ZnO nanowires. These experiments were primarily designed to assess whether the recipe used by Dulub et al. [15] was being followed and whether it would be successful when applied to nanowires and measure the effects of the treatment on local transport measurements. These experiments were furthered by studying the effects of the treatment on the defects. Defects play an important role in ZnO as they influence the electrical properties and there has been much debate as to the exact nature of the defects. Therefore PL, XPS, STS and 2 point probes were implemented to examine

the effects of argon bombardment and heating on the defects present and measure the change in electrical resistance. A review of literature relating to experiments on the defects in ZnO and treatment of ZnO is presented in Chapter 2. Chapter 6 continues with a revised recipe which was used to clean single crystal ZnO and the ZnO nanowires before STM was carried out.

The final experiment reported in this thesis moves away from nanowires and onto ZnO nanosheets. Nanosheets are a relativity new form of ZnO which can easily be synthesised in large quantities in solution in a commercially available microwave and deposited onto devices. Their natural large surface area means they are ideally suited to gas sensing and solar cells. Therefore Chapter 6 also reports an annealing experiment on ZnO nanosheets to examine whether their properties are similar to ZnO nanowires and if they can be altered for improved device application.

Chapter 2: Literature Review

This chapter reviews the literature relating to the experiments carried out in Chapters 4, 5 and 6. This chapter first reviews general STM and its uses to obtain atomic resolution on silicon and other materials such as gallium arsenide. The chapter then reviews literature that has been published on how the tip can affect the measurements taken. It also covers methods of cleaning the tip and removing the native oxide. Studies of cleaning and STM on both single crystal ZnO and nanostructures of ZnO have also been reviewed. This chapter then moves on to review ZnO nanowire growth which includes aqueous synthesis, which was used for experiments reported in the final two results chapters, and other methods of growth such as CVD.

The chapter also reviews the literature published by groups that studied the defects and treatment of ZnO nanowires. A table is presented that contains the published defects that have been observed and information about their energy transitions and corresponding wavelength. The chapter finishes with a short review of work carried out on ZnO nanosheets. These are a relatively new form of ZnO and there has been little work carried out on them.

2.1 STM

The overall goal of this thesis is to study the surface of ZnO nanostructures by taking low-dimensional local transport measurements using STM probe style systems. A description of the instrumentation and theory of STM is given in Chapter 3. This technique was first carried out by Binnig et al. [16] in 1982 in the IBM Zurich Research Laboratory. They used tungsten or molybdenum tips to image the surface topography of gold (110), silicon (111) and gallium arsenide (111) and observed the roughening of a gold surface when the sample was heated to 300 °C and the disappearance of the surface reconstructions at 400 °C while annealing and cleaving Si led to different reconstructions and different types of steps [16].

Silicon 7x7 is used in the experiment carried out Chapter 6 to test the quality of the STM tips. Figure 2.1 below shows the STM atomic resolution obtained on Si(111) by Nuffer et al. [17] when studying dopants. STM images were reported using both positive tip bias, which images the filled states of Si when electrons are extracted from the valence band (VB), and negative tip bias which images the empty states of Si by injecting electrons from the tip into the conduction band (CB) of the sample. Both display the 7x7 reconstruction of silicon atoms with boron atoms shown by arrows. Similar results have also been reported by Baski et al. [18], who studied both Si (001) and Si (111).

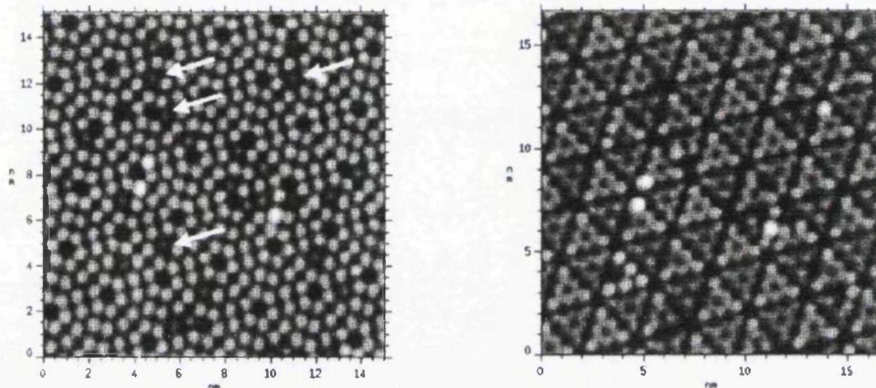

Figure 2.1: STM images for SI (111) (7x7) showing boron dopant atoms. Left: positive tip bias, right: negative tip bias, by Nuffer et al. [17]

In Chapter 4 an experiment is carried out in order to assess the effects of oxide on a STM tip by carrying out STS on GaAs. Depuydt et al. [19] used STM and STS to study Te doped GaAs single crystals. In order to produce a clean surface, the crystal was cleaved along the (110) surface in vacuum to prevent the native oxide growing. The groups used STS to measure the band gap to be ≈2 eV. They noted this is much higher than the 1.52 eV band gap at 5 K and 1.43 eV at 300 K, but state that the difference is due to voltage induced band bending. This is backed up by Feenstra et al. [20] who noted the effects of tip induced band bending due to the presence of an electric field generated by the STM probe. Observations by Tiwari et al. [21] also state that changes in the measured band gap of GaAs is caused by the doping concentration. They state that lower doping concentrations give a larger measured band gap. Gaan et al. [22] also found that n-type GaAs can appear to be p-type when taking STS measurements due to surface states.

2.2 Tip Cleaning

Part of achieving atomic resolution on ZnO requires producing high quality tungsten probes. Details are presented in Chapter 3 on a method to make STM probes based on Ibe et al. [23] who states that there are two ways to etch metal electrodes: alternating-current (ac) etching or direct-current (dc) etching and Chapter 4 describes experiments that observe the effects of probe oxide and how to remove it.

There have been several reports of the effects of probe oxide and other contaminates on the measurements taken using STS. Gimzewski et al. [24] observed that leaving an iridium tip to degrade in ultra-high vacuum (UHV) changed the STS curve of a silver sample from Ohmic to rectifying. They suggested that carbon or oxygen contamination of the tip caused an extra barrier to transport resulting in a higher voltage needed to initialise tunnelling. The effect on the STS spectra when CO was absorbed onto a tungsten STM tip was examined by Bartels et al., [25] while studies carried out by Shen et al. [26] and Clemens et al. [27] show the effect on the STS spectra when a layer of indium oxide is deposited on InGaAs. Both studies noted that the band edges shifted down in energy when a monolayer of In_2O was deposited on n-type InGaAs and only the CB edge shifted towards the Fermi level when p-type InGaAs was used. Shen et al. suggests that this behaviour is due to surface band bending caused by surface dipoles or surface states. This shift in the spectra is similar to that observed in Chapter 4 when carrying out STS with a tip with probe oxide and with the probe oxide removed.

Several groups have heated tungsten tips using the previously mentioned methods to remove the oxide layer using temperatures ranging from 1223 K to 2200 K [6-8, 28, 29]. Cricenti et al. [6] used electrochemical etched tungsten tips which were characterized using SEM and scanning Auger microscopy. The tips were annealed to 1800 K which removed most of the native oxide. Albrektsen et al. [7] heated their tips to 1223 K, measured using an optical pyrometer ,which partially desorbed the oxygen. Lucier et al. [8] heated STM tips to 1300 K which was indicated by an orange glow while Bode et al. [28] annealed to temperatures greater than 2200 K. Kim et al. [29] reported that tungsten tips had to be heated to temperatures greater

than 2000 K in order to sublimate the oxide layers but noted that temperatures above 2500 K caused the tips to blunt. Staufer et al. [9] also reported blunting of the tip, however, this was at a much lower temperature of 2000 K.

For the experiments carried out in Chapter 4, the tips were annealed using a method put forward by Yu et al.[11] who modified a tip transfer plate, shown in Figure 2.2 (a) to clean STM probes by direct current heating. They welded a contact carrier made from a loop of tantalum to the legs of an Omicron plate which allows the bottom of the shaft of the STM tip to contact the tantalum so that a retractable contact can pass a current through the probe to anneal it, Figure 2.2 (b). There are several other methods for annealing tips such as that carried out by the Argonne National Laboratory which modified a tip plate to clean tungsten probes by heating via an electron-beam to 2200K [10]. Their tips were then coated in Fe for spin-polarized imaging. Ishida et al. used a similar method to clean tips using electron bombardment to heat the probe [30].

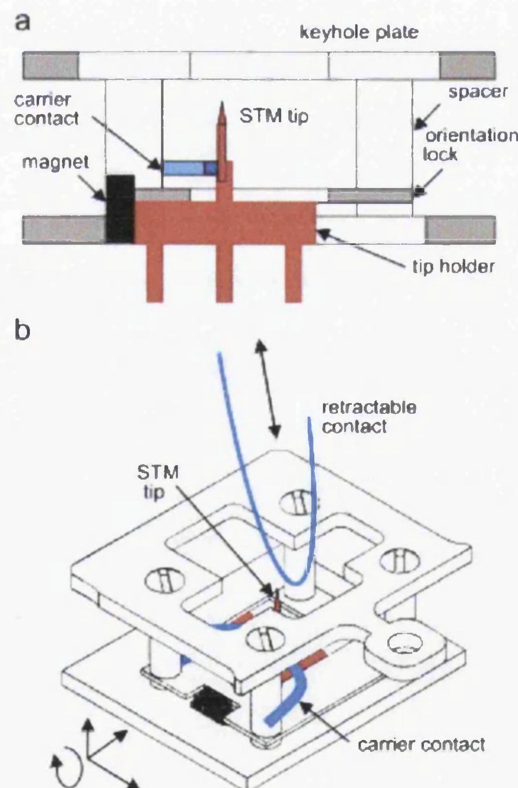

Figure 2.2: Schematic of Yu et al. modified transfer plate for direct current annealing of STM tips [11].

The results presented in Chapter 4 show that the probe oxide modifies the electrostatic force between the tip and sample. Studies have shown that the tip can influence the surface of the sample, with tip induced quantum dots being of particular interest [31-35]. More recently, tip surface interactions have been used to permanently alter the surface of graphene and to cause and measure oscillations in graphene [36]. Surface tip interactions are also governed by tip shape which also depends on probe oxide. Probes used for AFM have been modelled by Wright et al., who found that tip shape is reflected in the frequency shift and higher harmonics maps [35]. Tip shape also effects sub-micron 4 point probe measurements as thinner tips apply more pressure that can break through oxide layers on a surface [37]. It is generally thought that tip shape is determined by the etching process. However, the effects of oxide layers on probe shape and interaction have not been widely discussed.

2.3 Cleaning and STM of ZnO

ZnO is a metal oxide semiconductor with a wide direct band gap of 3.37 eV at room temperature and a large excition binding energy of 60 meV [38]. It has lattice parameters of $a = 0.325\ nm$ and $c = 0.5206\ nm$. It is a n-type material with a wurtzite crystal structure and has attracted much scientific attention due to its wide range of properties including: piezoelectricity, high transparency, room-temperature ferromagnetism, insulating to metallic conductivities (depending on doping) and chemical-sensing effects [39]. These properties make this material very appealing for use in nanoscale devices which rely on the surface properties. STM is one of the most surface sensitive characterisation techniques; however, no one has yet achieved atomic resolution on a ZnO nanostructure.

To achieve atomic resolution on a surface, the surface has to be cleaned. There have been several reports on the cleaning of single crystal ZnO. Valtiner et al. implemented chemical etching to clean the surface of single crystal ZnO. They carried out three cleaning processes using NaOH to etch 0001 single crystal ZnO [40]. The first treatment used only etching in 3 M NaOH; the second treatment involved annealing in a humid oxygen atmosphere after etching and the third treatment involved a dry oxygen atmosphere after NaOH etching. The group carried

out AFM, LEED and ToF-SIMS and found that all three treatments produced a clear six fold LEED pattern. However, they concluded that annealing in a humid oxygen atmosphere was the best treatment as the AFM results show large flat terraces while annealing in a dry oxygen atmosphere produced a structure that was not well ordered. It was also noted that the first treatment also produced flat terraces but only ~100nm wide. These groups therefore concluded that water plays an important role in the reorganisation process. However, this process will only work for (0001) surfaces as it is a polar surface. The side facets ($10\bar{1}0$) of the nanowires are non-polar and therefore an alternative cleaning is needed.

In 1983 Zwicker et al. [41] cleaned (0001) and ($000\bar{1}$) ZnO single crystals in order to study bonding Cu onto the surface. They used argon bombardment and annealing to clean the ZnO, then carried out LEED to assess the surface order. A description of interrupting LEED patterns is presented in Chapter 3. Dulub et al. [15] also carried out LEED on single crystal ZnO (0001), ($000\bar{1}$), ($11\bar{2}0$), and ($10\bar{1}0$), and their image is shown below in Figure 2.3 and will be used later as a comparison for the results in Chapter 6.

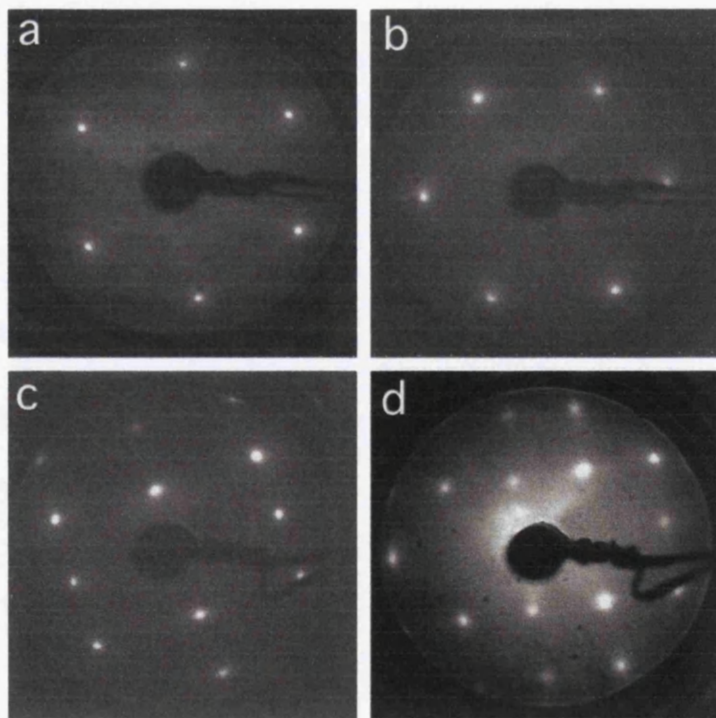

Figure 2.3: LEED of single crystal ZnO a) (0001)-Zn, b) ($000\bar{1}$)-O, c) ($10\bar{1}0$) and d) ($11\bar{2}0$) [15].

Dulub et al. [15] also carried out STM on (0001), ($000\bar{1}$), ($11\bar{2}0$), and ($10\bar{1}0$) faces of ZnO single crystals. Oxygen terminated surfaces etch more rapidly than zinc terminated surfaces. The samples were cleaned using cycles of 1–2 keV Ar sputtering and annealing at 600–750°C for 5–30 minutes in UHV. The group found that annealing at higher temperatures led to a high rate of Zn and O sublimation which in turn led to surface roughening. The ZnO ($000\bar{1}$) O terminated surfaces usually required more cleaning cycles than the ZnO (0001) Zn terminated surfaces. All samples were prepared by a final 1 keV Ar sputtering cycle for 15 min and annealing at 700 °C for 5 minutes to repair any sputter damage. This cleaning technique was used by Dulub et al. [15] in order to form wide terraces. STM was carried out on all the samples and the group achieved near atomic resolution observing bright and dark rows on the ($10\bar{1}0$) ZnO sample in the ($\bar{1}2\bar{1}0$) direction. The group used a setting of 1-2.5 V and a tunnelling current of ~1.0 nA. The terraces can be thought of as the steps and layers in High Order Pyrolytic Graphite (HOPG). The group's STM images for the (0001) Zn terminated sample shows triangle shaped terraces and islands separated by a single layer step while the oxygen terminated sample display hexagon shape structures separated by a double layer step height. The ($000\bar{1}$) sample was imaged to show flat steps of single layer depth.

Parker et al. [42] has also carried STM of single crystal ZnO with orientations (0001) and ($000\bar{1}$). This group used HCl etching to determine the orientation of the crystal and similarly to Dulub et al. [15] they also cleaned the sample in UHV using Ar bombardment and annealing. The cleaning process was carried out in cycles, however, the group gave no details in the paper about the power of the Ar bombardment. Dulub et al. [15] and Parker et al. [42] then annealed the crystals for 20 mins at 1200 K. This cycle was repeated until 1x1 low energy electron diffraction (LEED) patterns were obtained. The crystal was then annealed in Oxygen at 900 K for 5 mins. Parker et al. [42] then allowed the samples to cool in O_2 to restore the surface stoichiometry. Parker et al. [42] achieved images similar to Dulub et al. [15], the (0001) facet showed the triangle shaped feature when using a tunnelling current of 0.4 nA and a voltage of 3.5 V and is shown in Figure 2.4.

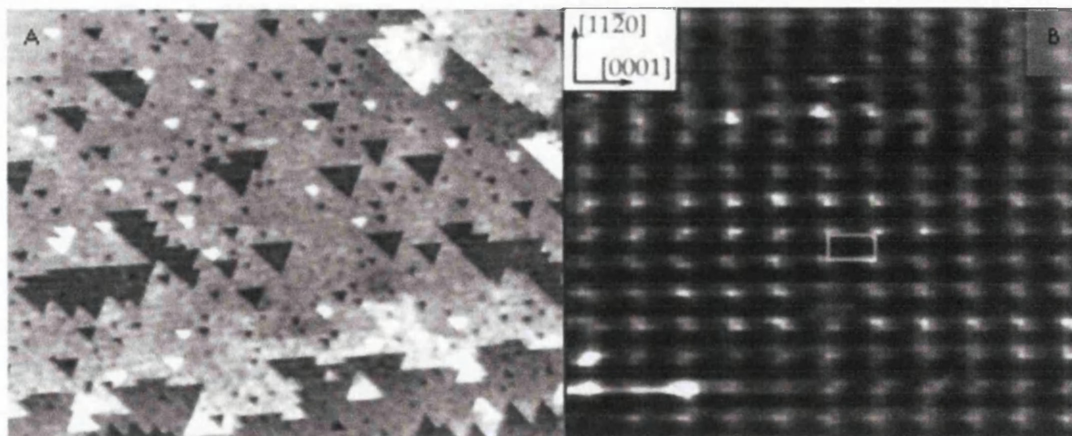

Figure 2.4: A) STM of the (0001) for ZnO single Crystal B) STM of the ($10\bar{1}0$) for ZnO single Crystal [42].

Several groups have attempted to carry out STM/STS and other probing techniques on ZnO nanostructures. Ericsson et al. [43] carried out spectroscopic photoemission and LEED of assorted ZnO nanostructures that were supplied by Alfa Aesar GmbH & Co KG. The nanostructures were dispersed in ethanol and spin coated onto Si/SiO. The substrate was modified using the Shiraki method to make it hydrophilic [43]. Ericsson et al. found that the nanostructures were of a rod like form with a diameter of ~70 nm and length ranging between tens and hundreds for nanometers. To clean the ZnO nanostructures, the group annealed the samples using an electron beam aimed at the back of the sample substrate. The samples were heated to temperatures ranging from 480°C to 650°C for times of up to 105mins in a vacuum with a pressure of 7.5×10^{-10} mbar or lower. This temperature was used since it is below the temperature that distorts SiO_2. The group concluded that heating for longer times at high temperatures produced clearer LEED images.

Maffeis et al.[44] carried out AFM, STM and STS on ZnO nanobelts. Their STS results showed that ZnO nanobelts have a 3.3 eV band gap with near flatband conditions. They did not achieve any form of atomic resolution but were able to detect physical defects in the structure. The group grew the nanobelts using CVD and dispersed the nanostructures in ethanol and deposited them onto silicon using a micropipette. The samples were then heated at 300°C in air for 60 mins.

Herrera-Zaldivar et al. [4] carried out STM and STS on ZnO nanorods grown via a hydrothermal technique. Using a set point of 1nA and a sample bias of 2V, the

group achieved STM images of the terraces and gained a structure of prismatic nanorods. They did not achieve atomic resolution on the nanorods and, like Maffeis et al. [5], they do not state any cleaning method. This suggests that a cleaning method is needed and Dulub et al.'s [15] recipe using argon bombardment and heating provides the bases for the experiments carried out in Chapter 6.

2.4 ZnO Nanowire Growth

ZnO can form a number of different nanostructures such as 2-dimensional nanosheets and nanobelts, 1-dimensional nanowires and nanorods and 0-dimensional quantum dots [44-46]. Studies have been carried out using ZnO nanowires as micro lasers, field emitters, piezo generators and as cantilevers in scanning probe microscopes [47-49].

ZnO nanowires have been synthesised using several different techniques. The most common methods to grow nanowires are chemical vapour deposition (CVD) and aqueous growth. Wagner et al. [50] used CVD to grow Si nanowires by the vapour-liquid-solid (VLS) mechanism. They deposited small particles of gold on a silicon wafer to act as a catalyst and exposed it to a vapour of hydrogen and SiCl at 950 °C. A similar method has been used to produce ZnO nanowires. Ramgir et al. [51] produced nanowires with pencil like tips on alumina substrates by heating pure zinc to 950 °C in a mixture of argon and oxygen. Huang et al. [52] have also produced ZnO nanowires using VLS CVD on gold coated silicon and heating a 1:1 mixture of ZnO powder and graphite to 950 °C for 5-30 min under a constant flow of argon. They produced 10-20 μm long nanowires with diameter 80-120 nm with Zn/Au alloy tips. A similar method was used by Greyson et al. [53] in 2004 who used lithography to etch the metal film to produce clusters of ZnO nanowires. A variation on this method was carried out by Jie et al. [54] who synthesised nanowires using epitaxial growth. They produced highly aligned growth using CVD with 1:1 ZnO and graphite powder on a ZnO film.

A low cost, large scale method of synthesis is aqueous growth which was first carried out in 1990 by Verges et al.[55]. They used a mixture of zinc nitrate, zinc chloride and hexamethylenetetramine (HMTA) heated in a water bath at 80 °C to

synthesise prisms and pebble like ZnO nanostructures. Vayssieres et al. [56] used this technique to grow ZnO nanowires in a conducting glass and Si substrates. They produced nanowires of up to 10 μm by growing for up to 10 hours at 80 °C. Both groups used ZnO seed layers to initialise the growth.

An in-depth discussion of the aqueous growth mechanism was given by Jacobs et al. [39] in 2010 and examined the chemistry of the reaction of HTMA and zinc nitrate with water through to the end product of ZnO. They also studied the pH as the mass of Zn^{2+} converted from liquid to solid as a function of growth solution temperature. They found that the amount of Zn^{2+} in solution and the pH decreased sharply when the temperature was above 90 °C. However, they also found that the amount of Zn^{2+} solid gradually increased when the temperature was increased and state that the pH of the growth solution is ~10. Schmidt-Mende et al. [1] summarised the reaction into three simple chemical equations which are given below.

$$(CH_2)6N_4 + 6H_2O \leftrightarrow 6HCHO + 4NH_3 \qquad (2.1)$$

$$NH_3 + H_2O \leftrightarrow NH_4 + OH^- \qquad (2.2)$$

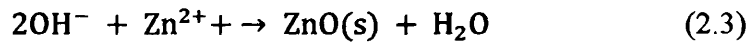

$$2OH^- + Zn^{2+} + \rightarrow ZnO(s) + H_2O \qquad (2.3)$$

In order to carry out STM on a ZnO nanowire in Chapter 6, it was thought that a large diameter nanowire was needed so that it would be easier to approach the tip onto the area of interest. Sugunan et al. [13] state that the diameter of a nanowire is dependent on the ratio of the precursors when they examined the role of HMTA in their paper in 2005. They suggest that HMTA caps the non-polar side of ZnO nanowires and therefore only allows growth on the (001) plane.

Sugunan et al's [13] theory of the HMTA sticking to the sides of the ZnO nanowires has not been widely discussed and was disproved by McPeck et al. [57] who showed that HMTA did not attach to the sides of the nanowires and acts only as a source of OH^- ions and as a pH buffer of 5.7 to maintain the ZnO saturation index. Another explanation of the change in morphology due to precursor concentration was given

by Sun et al. [58] who presented a theory based on the local chemistry around the tips of the nanowires as they are grown.

Greene et al. [59] has controlled the aspect ratio of aqueously grown nanowires by adding low molecular weight poly-ethylenimine (PEI) and sodium citrate to the growth solution. They found that PEI increases the aspect ratio by increasing the length of nanowires to 25μm from 2 μm while sodium citrate produced ZnO platelets. They also used a 1:1 molar ratio of zinc nitrate and HTMA, using 0.025 M at 90 °C.

Studies have also shown that the seed layer and substrate have an effect on the morphology of ZnO nanowires grown. Brown et al. [14] deposited different metals, Au and Ni, onto silicon substrates before depositing the ZnO seed layer. They found that the substrate affects the grain size and roughness of the seed layer which changes the diameter of the nanowires. They state that using Si substrates resulted in the longest and widest nanowires, followed by Ni then Au. They found that a ZnO seed layer on Si was the least rough and had the smallest grain size while the Au sample was the most rough with the largest grain size. A similar study has been carried out in Chapter 5 in order to create a recipe that would produce long wide nanowires to probe with STM.

Song et al. [60] have also studied the effects of the seed layer on ZnO nanowire growth. They produced 4 different seed layers: 2 types of ZnO, Al-doped ZnO (AZO) and Ga-doped ZnO (GZA). They also studied the effects of the seed layer thickness using seed layers of 200 nm, 330 nm, 603 nm and 950 nm. They found that thicker seed layers produced smaller diameter ZnO nanowires with longer lengths.

Groups have tried to speed up the aqueous process to grow ZnO nanowires by using commercially available microwave ovens. Unalan et al. [61] found that using higher power microwaves increased the growth rate of ZnO nanowires. They found they could produce similar lengths to traditional aqueous synthesised nanowires grown for 90 mins in less than 6 mins using 700W. However, their nanowires were much

shorter compared to the nanowires grown by others using the aqueous technique discussed above at around 30 nm. A study was carried out in Chapter 5 to grow longer nanowires using a microwave.

2.5 ZnO defects and treatment

Defect chemistry of ZnO has been widely discussed but agreement on the origin and effects of defects has not yet been reached. Numerous studies have been carried out in which the defects have been measured after treatments such as argon bombardment and heating. These two treatments are carried out in Chapter 6 when the nanowires are cleaned therefore the defect chemistry of the nanowires will change during the cleaning process. Any change in the defects will alter the properties of the nanowires and therefore alter the working of any device that the nanowires are incorporated into.

An often used method of measuring defects is photoluminescence (PL); the theory of PL is presented in Chapter 3. All studies involving PL of ZnO have seen a peak centred around 377 nm which is the exciton and is often referred to as the near band edge (NBE) and equates approximately to the band gap [61-63]. Studies also show a second large PL peak which is much broader and is centred around 550 nm which is commonly known as the deep energy level (DEL) or green luminescence defect band [64]. The origin of this peak has been widely debated but it is generally agreed that it consists of multiple defect components. Liu et al. [65], Schmidt-Mende et al. [1] and Lin et al. [66] have all publish diagrams showing the defect transitions within the band gap. The table below compiles a list of some of the defects that have been published with their transition energies and the corresponding wavelengths relative to the CB, VB and other defects. The table also states whether the defect is a donor or an acceptor. It should also be noted that some defects appear more than once, this highlights the continued debate about the origin of the defects and the positions within the band gap are not know. Details of origin of energy transitions observed using PL are given in Chapter 3.

Table 2.1: Some of transitions within the band gap on ZnO.

Name	Energy (eV)	Wavelength (nm)	Transition
NBE	3.36	377	Exciton NBE
Zn_i^o	3.25	381	Zn_i^o (donor state) to VB [65]
V_{Zn}^-	3.12	398	CB to V_{Zn}^- (acceptor state) [65]
V_{Zn}	3.06	405	CB to V_{Zn} (acceptor state)[66, 67],
Zn_i	2.90	427	Zinc Interstitial (donor state) to VB [66]
Zn_i^+	2.80	443	Zn_i^+(donor state) to VB [65]
Zn_i V_{Zn}^{2-} /V_{Zn}^-	2.74	452	Zn_i (donor state) to V_{Zn}^{2-} /V_{Zn}^- (acceptor state)[1, 65, 67, 68]
O_i^-	2.64	470	CB to O_i^-(acceptor state) [65]
V_O^+	2.48	500	V_O^+ (donor state) to VB [69]
O_{Zn}	2.38	520	CB to O_{Zn} (acceptor state) [65-67]
V_O	2.30	539	V_O (acceptor state) to VB[65, 70]
O_i	2.28	543	CB to O_i (acceptor state) [66, 67, 71, 72]
V_O Zn_i	2.16	574	V_O (donor state) to Zn_i (acceptor state) [67]
V_O^{++}/ V_O^+ O_i	2.00	595	V_O^{++}/ V_O^+ (donor state) to O_i (acceptor state) [1, 69, 71, 73]
V_O^+ V_O	1.94	633	V_O^+ (donor state) to V_O (acceptor state) [74]
V_O	1.75	691	V_O (acceptor state) to VB [67]
V_O	1.62	765	CB to V_O (acceptor state)[66-68]
O_{Zn}	1.49	832	O_{Zn} (acceptor state) to VB [67]
V_{Zn}^-	0.8	1549	V_{Zn}^- (acceptor state) to VB [1]
V_{Zn}^{2-}	0.56	2214	V_{Zn}^{2-} (acceptor state) to VB[71]
Zn_i	0.5	2480	CB to Zn_i (donor state)[71]
Zn_i^+	0.2	6199	CB to Zn_i^+ (donor state)[70]
Zn_i^{++}	0.15	8266	CB to Zn_i^{++} (donor state)[1]
V_O^+	0.05	24797	CB to V_O^+ (donor state)[71]
Zn_i^+ /Zn_i^X	0.05	24797	CB to Zn_i^+ /Zn_i^X (donor state)[1]
H_i	0.03-0.05	41328	CB to H_i (donor state) [71, 75]

The literature suggests at positively charge oxygen vacancies are deep level donor states and migrate to the surface of ZnO nanostructure to minimise lattice energy and increase the negative surface charge and give rise to the n-type nature of ZnO [76-78]. The literature also suggests oxygen interstitials are deep level acceptor states which also migrate to the surface of ZnO nanostructure [79]. This suggests that altering these defects will alter the conductivity, which was seen during the experiments reported in Chapter 6. Zn interstitials are also donor state however they are shallow and unstable at room temperature and anneal out at 170 K and therefore are not observed under room temperature PL [64]. Zn vacancies are shallow level acceptors and can be observed under illumination at low temperatures [64]. It has been suggested that hydrogen forms shallow level donors throughout the bulk of ZnO and sit very close to the CB giving rise to the n-type nature of ZnO [75].

There have been several studies in which the surface of ZnO nanowires have been modified using plasma, similar to ion bombardment which is carried out in Chapter 6, and the defects and conductivity measured after treatment. Ra et al. [80] exposed ZnO nanowires to oxygen and hydrogen plasma for two minutes and observed that oxygen plasma decreased conductivity from 28.3 to 0.2 Scm^{-1} while hydrogen increased it from 26.4 to 174.7 Scm^{-1}. They took I-V measurements on single ZnO nanowires by rubbing the nanowires onto Ti and Au electrodes. Ti/Au was then deposited on top to obtain a better contact. They argue that the drop in conductivity is due to a decrease in donor like defects or an increase in electron trapping species near the surface such as O^-, O^{2-}, and OH^- (shown by SIMS) which are adsorbed onto the surface. This species extract electrons from the CB therefore reducing the carrier concentration reducing conduction. They also state that H is a shallow donor.

Ra et al. [77] has also used oxygen plasma to modify the surface of ZnO nanowires that had been incorporated in a FET and observed a shift in the threshold voltage from -38 to -3 V. They also used Ti/Au as the electrodes for the source and drain with a SiO_2 back gate. They found the carrier concentration and mobility of the ZnO nanowires decreased as exposure time to oxygen plasma was increased. They carried out SIMS that showed that the concentration of O^- and OH^- had increased with plasma treatment.

Law et al. [81] have shown that oxygen plasma reduces the carrier concentration of ZnO nanowires by creating two samples which consisted of an interconnected mesh of ZnO nanowires that contacted electrode pads. The first sample was exposed to an oxidizing gas of O_2 while the second sample was treated with a reducing gas of NH_3. They found that O_2 plasma treatment reduced the conductivity of the nanowires while the reducing treatment increased the conductance. They found that the oxidizing gas plasma reduce the negative surface charge that reduced the electron concentration on the surface of the nanowires which caused upwards band bending, illustrated in Figure 2.5 a),b) and c). The reducing gas plasma increase the negative surface charge on the nanowires increasing the electron concentration at the surface which caused downwards band bending, illustrated in Figure 2.9 d),e) and f). They also carried out XPS, the theory of XPS is explained in Chapter 3, and fitted two curves under the O1s peak. They attributed the lower energy curve of 529-530.7 eV to O^{2-} in bulk of ZnO and called it O1 while the higher energy curve of 531-532 eV was assigned to the O^{2-} of the surface which they called O2. They found that the O1/O2 ratio decreased from 0.51 to 0.40 when the nanowires were treated with oxygen plasma indicating that an increase in O^{2-} on the surface after treatment was caused by the oxidizing gas bonding to the surface. The O1/O2 ratio after NH_3 plasma treatment increased to 0.78 which they state is caused by NH_3 plasma reacting with O^{2-} on the surface and removing electrons and therefore reducing the carrier concentration.

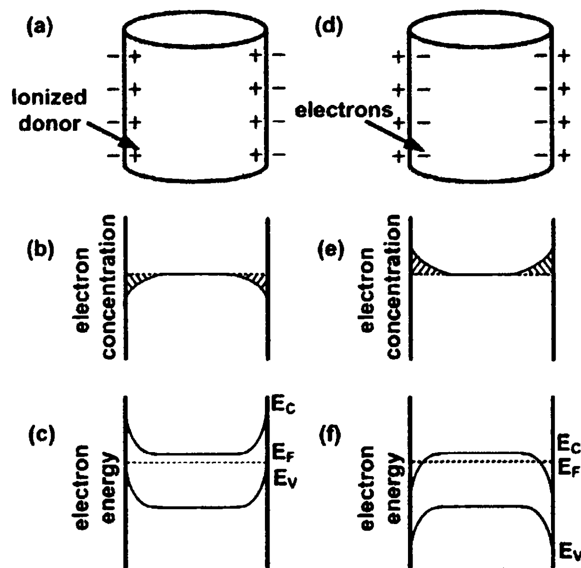

Figure 2.5: Space–charge layer on a ZnO nanowire after exposure to an oxidizing gas plasma: (a) distribution of charges, (b) electron concentration, and (c) band structure. Space–charge layer on a ZnO nanowire after exposure to a reducing gas plasma: (d) distribution of charges, (e) electron concentration, and (f) band structure [81].

Ra et al. [78] has also studied the effects of Ar ion bombardment on ZnO nanowires by creating a single nanowire FET similar to that discussed above and calculating the mobility and carrier concentration before and after treatment. They observed that the mobility, carrier concentration and conductivity increased after Ar plasma treatment. They also carried out PL which showed that the defects band increased in intensity after treatment and SIMS which showed that Zn concentrations did not change. Therefore the change in conductivity was due to a decrease in the electron trapping species on the surface.

Ha et al. [82] also observed a shift in the defects band when carrying out PL on ZnO nanowires. They found annealing ZnO nanowires at 900 °C in Ar and O_2 reduced the intensity of the defects band relative to the NBE peak that was centred at 376 nm. They observed that annealing in O_2 reduced the defects band the most and a peak at 524 nm became more pronounced. They fitted three curves under the defects band centred at 479, 524 and 595 nm for the as-grown sample while fitting curves centred at 466, 515 and 583 nm for annealed samples. They cited that the blue peak is caused by O and Zn vacancies or interstitials, the green band is associated with a single positively charged oxygen vacancy and the yellow band peak is caused by a

single negatively charged interstitial oxygen ion, however, this does not agree with other authors' assignments as per Table 2.1.

Banerjee et al. [83] carried out photoluminescence of ZnO nanowires and found that oxidizing the nanowires in an oxidation furnace at 700°C increased the intensity of the defects band when measured using PL. The defect band was further increased by annealing the oxidised nanowires in vacuum. The defect band was increased again by annealing in hydrogen after oxidation and vacuum annealing. They attributed these changes to graphite from the synthesis.

Cross et al. also observed a change in the defects band after annealing ZnO nanowires in different environments [84]. They found annealing in O_2 at 400 °C for 30 minutes reduced the defects band observed in PL. Annealing in vacuum at 1 x 10^{-3} Torr at 400 °C for two hours reduced the intensity of the defect band more. However, annealing in a 10% hydrogen 90 % argon environment at 400 °C for 30 mins reduced the defects band the most.

As part of the cleaning recipe, carried out in Chapter 6, the nanowires were annealed at different temperatures and STS was carried out to observe any change in conductivity. There is no literature which reports on experiments where ZnO nanowires were annealed and characterised using STS. However, Maffeis et al. [5] carried out STS on annealed nano-ribbons and found that annealing UHV for one hour at 600 °C and 700 °C shifted the STS spectra and the gradient of curves increased which indicated reduced surface band bending and an increase in conductivity. They also observed after annealing at 800 °C that the STS curve showed a large increase in tunnelling current at negative sample bias and a narrowing of the apparent surface band gap. They suggest that this is could be due to a loss of lattice oxygen leading to partial metallisation of the surface.

2.6 ZnO Nanosheets

ZnO nanosheets are another form of ZnO nanostructure but little research has been conducted into their properties. ZnO nanosheets, unlike ZnO nanowires, can be reproducibly synthesised in large quantities in a short period of time and their large surface area to volume ratio makes them ideal for sensor device application. Hu et

al. synthesised micrometer-sized single crystalline ZnO nanosheets by thermally decomposing ZnS powder in an induction furnace at 1500 °C at ~2 x 10^{-1} torr for 1.5 hours [85]. They also produced nanosheets by oxidation of Zn nanosheets in air using a resistance furnace at 350 °C for 4 hours. They carried out XRD to confirm that the sheets were ZnO and calculated the lattice constants to be $a=0.3244\ nm$ and $c=0.5201\ nm$.

Bai et al. [86] have also created sheet-like structures from ZnO by solvothermal decomposition of zinc chloride and ammonia on a copper plate. They too carried out XRD to confirm that the nanostructures produced were ZnO and also carried out PL. They observed that the sample, as grown, had an NBE peak centred at 383 nm and a large defect band centred at 510 nm. Annealing the sample in air reduced the size of the defects peak relative to the exciton peak and both peaks shifted to 380 nm and 495 nm. Annealing in oxygen removed the defect peak and the near band edge shifted to 378 nm. They explained these changes as removal of ionised vacancies and interstitial impurities in the crystal which is similar to the results observed when annealing ZnO nanowires.

Tarat et al. [87] have created ZnO nanosheets, shown in Figure 2.6, by synthesising layered basic zinc acetate (LBZA) nanosheets and annealing them to convert them to nanocrystalline ZnO.

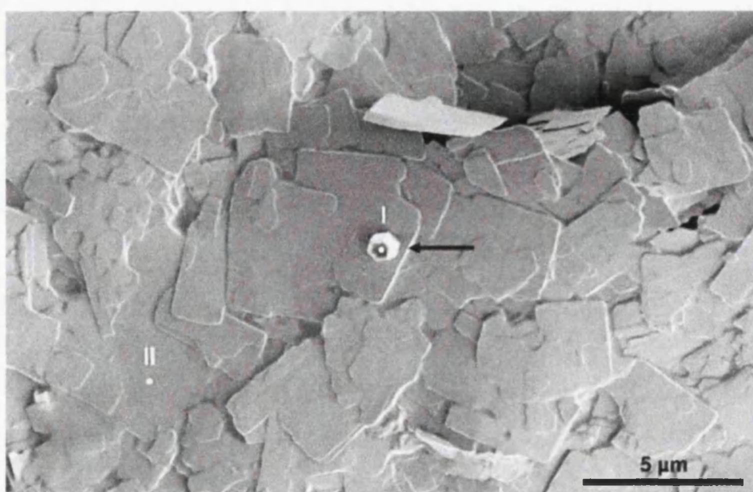

Figure 2.6: SEM of ZnO nanosheets grown by Tarat el al. [87].

They used a microwave to heat a solution of zinc acetate, zinc nitrate and HMTA for 2 mins. They then deposited the LZBA nanosheets onto silicon and annealed for 10 mins in air at different temperatures ranging from 200 °C to 1000 °C to convert it to ZnO and found that complete conversion occurs at 400 °C by using XRD. The ZnO nanosheets produced were polycrystalline and that increasing the temperature of annealing increased the grain size from 15.8 nm at 200 °C to 104 nm at 1000 °C. They also measured the thickness of the nanosheets using AFM and found that the thickness ranged from 20-100 nm. Their PL result is shown in Figure 2.7 and shows that annealing to different temperatures changed the shape of the defects band. Their results show that increasing the annealing temperature from 400 °C to 600 °C causes the area of the defect peak to increase relative to the NBE peak which was centred at 381 nm. Further annealing at 800 °C causes a slight reduction in the defect peak area and annealing to 1000 °C causes a shift in the main defect from ~650 nm to ~490 nm which is similar to the results reported by Bai et al [86].

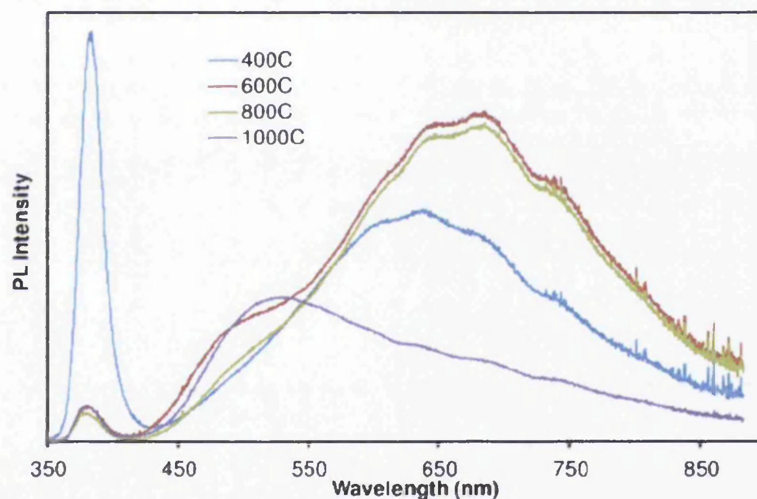

Figure 2.7: PL of ZnO nanosheets annealed at different temperatures [87].

Tarat et al. [87] also annealed the ZnO at 400 °C for varying amounts of time. They found that the defects band increased in intensity with annealing time which is shown below in Figure 2.8. They went on to use their nanosheets as gas sensors.

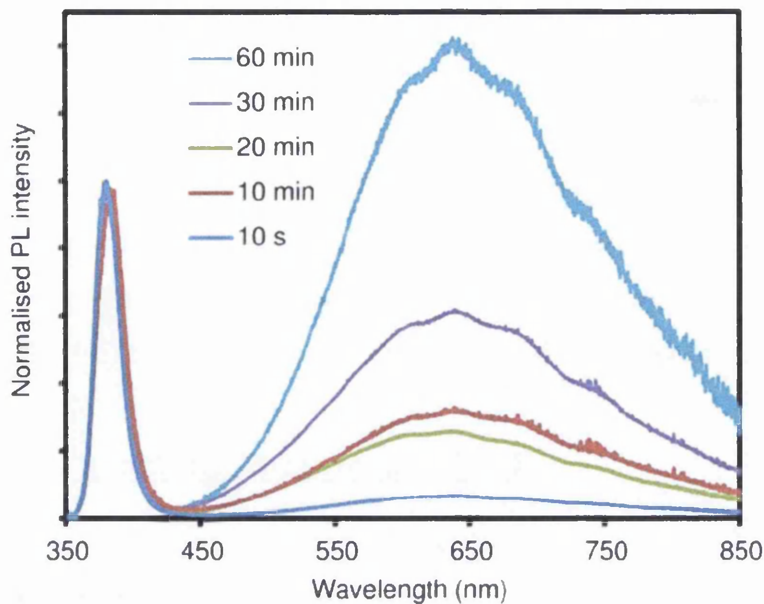

Figure 2.8: PL of ZnO nanosheets annealed at 400 °C for varying amounts of time [87].

Chapter 3: Scientific Methods

This chapter introduces the scientific methods used to carry out characterisation throughout the experiments described in this thesis. For each scientific method there is an explanation of the theory involved and the instrumentation used. The methods described are STM/STS, LEED, SEM/EDX, XPS/SAM/AES and PL.

3.1 Scanning Tunnelling Microscopy (STM)

3.1.1 Introduction

Scanning tunnelling microscopy (STM) is a probing technique that can provide atomic scale topography, with up to 0.1 nm lateral resolution and up to 0.01 nm depth resolution [88], and electrical information on a sample by using quantum tunnelling from a sharp biased tip. STM was invented by Heinrich Rohrer and Gerd Binnig in 1981 while working for IBM Zurich and were awarded half the Nobel prize in Physics in 1986 "... for their design of the scanning tunnelling microscope", the other half was won by Ernst Ruska for his work on electron optics [89]. In 1982 STM was used to determine the atomic structure of Si (111), as 7 x 7, after 25 years of debate [90]. STM images of atomic resolution on Si (111), as 7 x 7, are shown in Chapter 2 and is often used to test the quality of the probes.

3.1.2 Theory

STM relies on the quantum mechanical phenomenon of tunnelling. Tunnelling is the process by which a particle passes through a classically forbidden barrier. Classically a particle with energy, E, cannot surmount a potential with barrier height greater than E. However, quantum particles such as electrons, demonstrate a wavelike nature which can be shown to pass through such potential barriers known as tunnelling.

3.1.2.2 Potential Barrier

STM relies on tunnelling taking place from a tip to a sample via an air gap. This can be considered as a potential barrier of width a that represents the tip sample separation and the measured tunnelling current is related to the transmission

probability at point a. The energy and wavefunction diagram is shown below in Figure 3.1. The diagram shows that the wavefunction decays through the barrier before being transmitted as a wave.

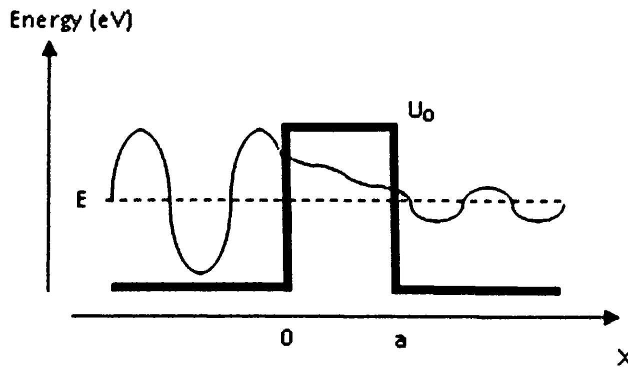

Figure 3.1: Depiction of a particle in a finite potential well.

In order to calculate the transmission probability of the particle through the potential barrier, the wavefunction must be calculated at point a. This is done by solving of the Schrodinger's equation, given in equation (3.1).

$$\frac{-\hbar^2}{2m}\frac{\partial^2\Psi(x)}{\partial x^2} = (E - V)\Psi(x) \tag{3.1}$$

Where $\hbar$ is Planck's constant divided by 2π, m is the mass of the particle and Ψ is the wavefunction. Inside the barrier equation (3.1) becomes,

$$\frac{\partial^2\Psi(x)}{\partial x^2} = -{k_b}^2\Psi(x) \tag{3.2}$$

Where,

$${k_b}^2 = \frac{2m_b(U_0 - E)}{\hbar^2} \tag{3.3}$$

Where m_b is he effective massive of the tunnelling electron in the barrier and U_o is the barrier height.

The solution inside the potential barrier is of the form,

$$\Psi(x) = Be^{-k_b x} \qquad \text{for } 0 < x < a \qquad (3.4)$$

Equation (3.5) is used to find the transmission probability, T.

$$T = |\Psi_b(x)|^2 \qquad (3.5)$$

Equation (3.4) in (3.5) gives at a,

$$T = |B|^2 e^{-2k_b a} \qquad (3.6)$$

The transmission probability proportional to tunnelling current and it can be seen from equation (3.6) that it is dependent on the barrier width or in the case of STM the separation between the sample and the closest part of the tip, which in some cases may not be the apex of the tip, and the energy of the particle.

3.1.2.3 Local density of states (LDOS) and Fermi Function

So far only the possibility of an electron passing through the vacuum gap has been considered. Another factor affecting the measured tunnelling current when carrying out STM is the local density of states (LDOS) [91]. LDOS is the number of states that are unoccupied at each energy level that the electron can tunnel into. LDOS differs from density of states (DOS) since small perturbations caused by potentials in crystal give rise to spatially dependent states. LDOS can be predicted using computational methods such as density functional theory (DFT).

As shown in Figure 3.2 DOS are dependent on the dimensions of the sample and zero dimensional structures have discrete energy levels [92]. For zero dimensional structures such as quantum dots, the exciton Bohr radius (distance in an electron-hole pair) is in the same order of size the semiconductor. This results confinement of the exciton in all directions and has discrete, quantised energy levels [93]. The

experiments carried out Chapter 4 show a tip induced quantum dot forms under the probe with empty discrete states present in the VB above the Fermi level that allow tunnelling to take place.

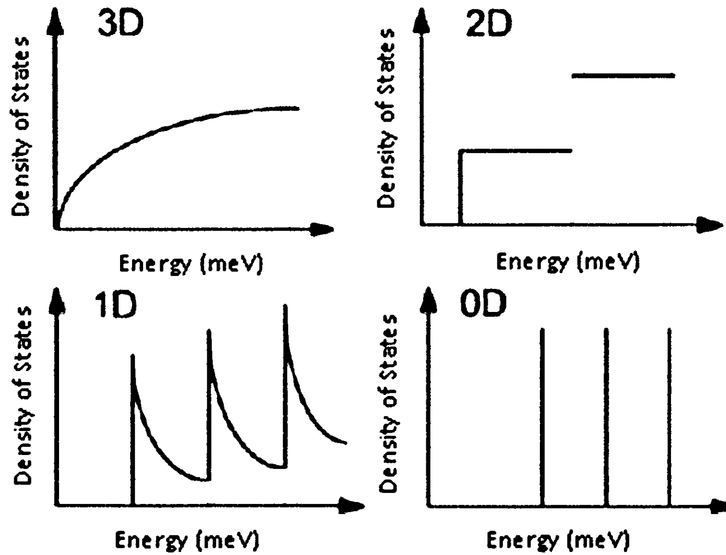

Figure 3.2: Graph of DOS against Energy for bulk, 2D, 1D and 0D materials.

Another factor that is needed to explain tunnelling current in a STM is the Fermi function which describes the probability that an electron will occupy an energy state at a given temperature [94]. In other words the Fermi function is used to predict how many electrons have high enough energy to tunnel. The Fermi function, *f((E)*, comes from Fermi-Dirac statistics [95] and can be derived from the grand canonical ensemble and is expressed in equation (3.7) below.

$$f(E) = \frac{1}{e^{(E-E_F)/kT}+1} \qquad (3.7)$$

Where E_F is the Fermi level, k is Boltzmann's constant, and T is the absolute temperature. The Fermi level is the highest electron energy in a material at absolute zero. In metals the Fermi level sits in the CB and in semiconductors the Fermi level sits in the middle of the band gap. In a semiconductor at absolute zero no electrons can exist above the VB since there are no free states in the band gap. As the temperature increases some electrons have energy above the Fermi level and at high

temperatures there is a possibility that some electrons can exist in the CB and is shown if Figure 3.3.

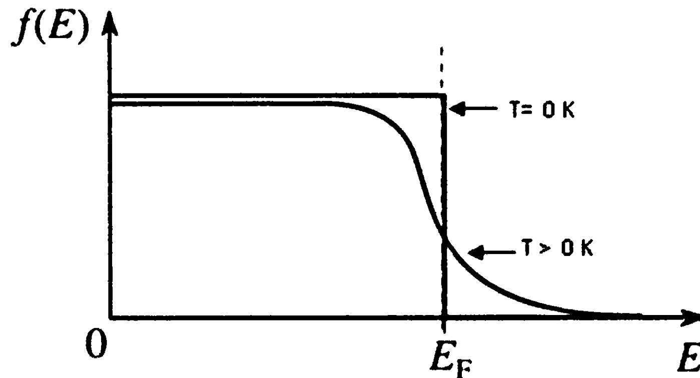

Figure 3.3: Graph of Fermi Function against Energy.

3.1.2.5 STM

The probability of tunnelling, DOS and the Fermi function all affect measurements taken when carrying out STM. With these factors in mind the process of STM will now be discussed and it is assumed the tip is close enough for tunnelling to take place and the sample is an n-type semiconductor at 0 K.

Figure 3.4A shows that when no bias is applied between the sample and the tip the Fermi levels, E_{FT} and sample E_{FS}, shift so that they are equal. No tunnelling takes place from the tip since there are no free states in the band gap on the semiconductor and no electrons can tunnel from the sample into the tip since electrons only exist in the VB which is at a lower energy than the Fermi level in the tip. When negative voltage is applied to the tip and therefore positive voltage applied to the sample, as show in Figure 3.4B, the Fermi level of the tip is increased due to the increase in potential energy of the electrons in the tip. The Fermi level of the sample also decreases due to the decrease in potential energy of the electrons in the sample. This results in an increase in E_{FT} relative to the E_{FS}. If the voltage is high enough the $E_{FT} > E_C$ and tunnelling will occur which is shown as an arrow pointing from the tip to the sample CB and therefore the CB is imaged. When a positive voltage is applied to the tip, Figure 3.4C), E_{FS} increases relative to the E_{FT}. If the voltage is high enough then $E_{FT} < E_V$ and tunnelling will occur from the VB of the sample into the tip and the VB is imaged.

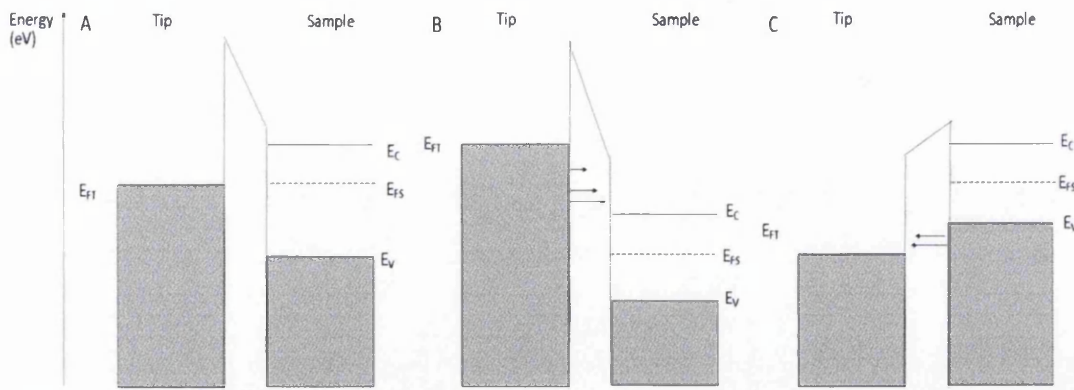

Figure 3.4: A) Band diagram of tip and sample when no bias is applied, B) Band diagram of tip and sample when negative bias is applied to the tip and C) Band diagram of tip and sample when negative bias is applied to the sample.

When carrying out STM a sharp tip with a bias applied is approached onto the sample until a set current, known as the set point, is measured. Increasing the voltage will increase tunnelling current for a given tip sample separation, therefore, when first approaching the tip onto the sample a high voltage can be used to prevent a tip making physical contact with the sample, known as a tip crash. For the same reason rough surfaces are initially scanned at high voltages. It can be seen from equation (3.6) that reducing the tip-sample separation, a, exponentially increases the tunnelling current causing the tip to become closer to the sample. Decreasing the voltage and increasing the set point will result in a greater signal to noise ratio.

3.1.2.6 STM Analysis

STM can be used to measure atomic position and it can be seen from equation (3.6) how changes in topography of the sample will alter tip-sample separation and therefore the measurement current. As the tip is scanning across a rising step either the tip will retract to maintain tunnelling current in which case the tip will trace out the topography of the sample (known as constant current mode), or the current will increase in which case the tunnelling current maps out the topography (known as constant height mode). However, similar results can arise from an increase in conductivity in the sample since there are more free states that the tunnelling electrons can occupy. Therefore the tunnelling current will increase and cause the tip sample separation to increase similar to a rising step. The difference between a topography feature and a change in conductivity of a sample can be determined by changing the height of the tip by changing the set point. Steps in the surface will

cause the tip height to change by the same amount independently of the set point while changes in conductivity will cause the step in STM line profile to change depending on set point

Similarly n-type materials have more states to tunnelling than a p-type material. Therefore n-type materials will cause a step in the STM line profile. These features can be different from topographic steps by changing the bias from negative to positive. Topographic steps will appear with the same magnitude with both negative and positive sample bias, however, the step will be inverted if the sample has transitioned from n-type to p-type.

3.1.2.7 Tip Effects

It was stated earlier that STM relies on a sharp tip, typically stated to be atomically sharp and ideally to end in a single atom. Tunnelling takes place at the least tip-sample separation, in other words the apex of the tip and the sample. If the tip is blunt or too short, information about the sample can be lost as shown in Figure 3.5 where it can be seen that the least separation may not be between the apex and the lowest point of the sample when scanning a trough. Instead tunnelling will take place between the side of the tip and the side of the trough which will result in a trough appearing less deep or appearing to have sloped sides and resolution is lost. Similar effects are seen if the tip is blunt therefore the tip should taper to a very sharp point. However, as discussed in Chapter 2, annealing of the tip to remove oxide can result in blunting therefore in the experiments carried out in Chapter 4 blunting is also examined.

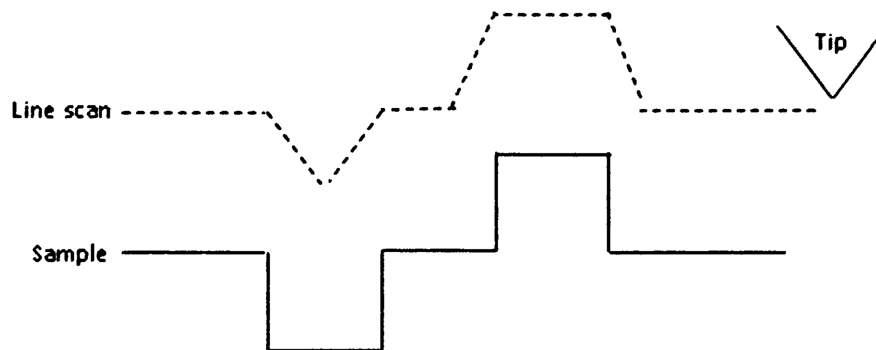

Figure 3.5: Illustration of a tip which is too short and broad, therefore, cannot resolve deep features.

Another tip artefact that is commonly seen on STM scans is the effect of a double tip. A double tip and the resulting line profile is shown below in Figure 3.6. It can be seen that a double tip can result in an area of the sample not being scanned. It can also result in the doubling of some features and these shadows on the scan are used to indicate double tips.

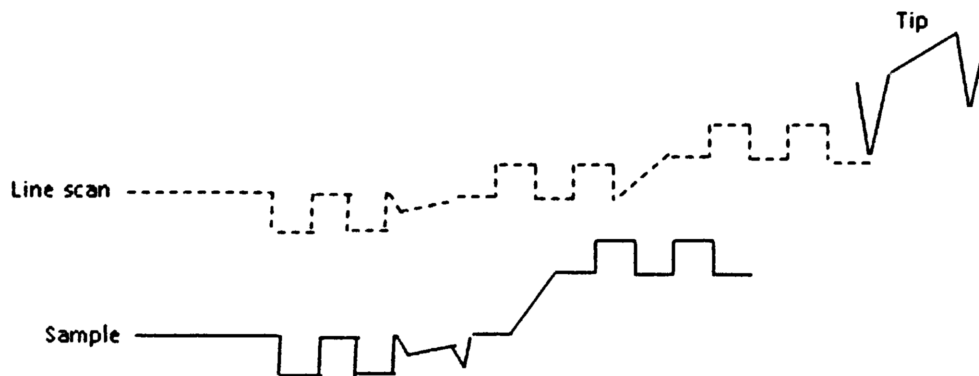

Figure 3.6: Illustration of a double STM tip above a surface and the resulting line profile.

These tip effects can be caused by poor etching or caused by oxide coating. Tip oxide has been discussed in the literature review chapter. So far, the physical properties of the tip have been discussed but the tip also interacts with the sample and this coupling can make changes to the STM scan. Since the tip is biased there is an electric field surrounding the tip. At high voltages the electric field can be strong enough to cause tip induced band bending and this is seen in Chapter 4 when carrying out STS with a tip that has not had the native oxide removed from the shank. Band bending was observed when carrying out two point probe on ZnO nanowires in Chapter 6.

3.1.2.8 Band Bending

Band bending will occur when a semiconductor (here n-type) and a metal (here tip) are brought into contact, the Fermi levels equalize causing an internal electric field at the interface and is shown in Figure 3.7. The CB in an n-type semiconductor is higher in energy so electrons will flow into the metal, assuming the temperature is high enough so that electrons in the semiconductor are present in the CB. This results in the probability density of electrons in the CB to fall near the interface and

leaves holes (ionised donors) in the semiconductor and electrons in the metal, the increase in electrons in the metal is negligible. This causes the CB to move away from the Fermi level and creates a depletion zone, w. The increase in the CB and VB energies near the interface causes a potential barrier, U_D, known as a Schottky barrier. The change in the bands near the contact is known as upward band bending. In a p-type semiconductor the bands bend downwards.

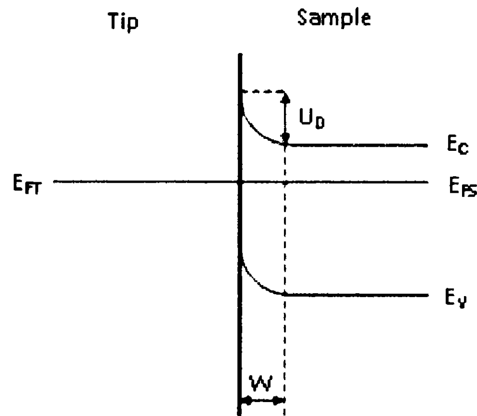

Figure 3.7: Diagram of band bending when metal is brought into contact with a n-type semiconductor.

The near contact of tip and sample in STM cause the same effect to happen. However, the bias applied between the tip and sample also affects the amount of band bending. When an n-type sample is negatively biased the barrier height reduces, known as forward bias. Under forward bias electrons are supplied to the sample which reduces the depletion region and pushed the CB back towards the Fermi level. The same happens to a p-type sample to which a positive bias is applied. When a positive bias is applied to an n-type sample the barrier height is increased, known as reverse bias. Reserve bias causes the depletion region to increase which causes a reduction in the likelihood of tunnelling. The same happens to a p-type sample to which a negative bias is applied.

Under high reverse bias the band bending can result in the formation of a tip induced quantum dot in the sample, as seen in the results in Chapter 4. The small potential well formed at the interface can act as a quantum dot with discrete energy states. The effects of band bending can be seen when carrying out scanning tunnelling spectroscopy [91].

3.1.2.9 Scanning Tunnelling Spectroscopy

Scanning tunnelling spectroscopy (STS) is a method that is an extension of STM that is used to provide further electronic information about the sample. Using STS it is possible to record spectroscopic and topographic data simultaneously. The tip is moved over a feature of interest on the sample and the feedback control is turned off so that the tip remains stationary in all directions and the bias on the sample is swept from negative to positive and the tunnelling current is plotted as a function of voltage. An example of a STS I-V curve on a ZnO nanowire is shown in Figure 3.8.

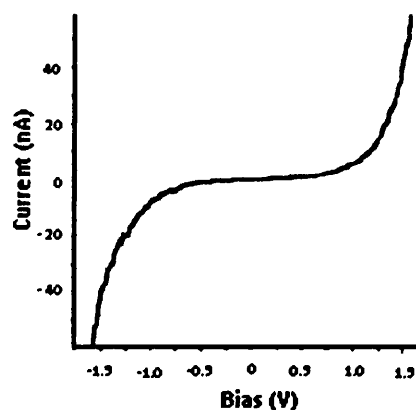

Figure 3.8: STS I-V curve from a ZnO nanowire.

It has already been discussed in Section 3.1.2.6 that when a high enough negative bias is applied to the sample electrons tunnel from the VB into the tip since E_{FS} increase relative to E_{FT}. Therefore as the bias is swept from negative to zero the VB is sampled. When the bias causes the energy level of the VB to drop below the Fermi level of the tip tunnelling does not occur since there are no free states in the band gap. As the voltage increases the Fermi level of the tip becomes greater than the energy of the CB and tunnelling occurs.

STS can be used to investigate the doping of a semiconductor sample by comparing relative positions of CB and VB with the Fermi level of the sample which is set as the voltage being zero on an I/V graph. To investigate the shifts in the CB and VB caused by probe oxide in Chapter 4, the STS data is plotted as a $\log_{10}$ of the current against voltage which gives a clearer indication of where the VB and CB edges lie.

The STS data in Chapter 6 is also plotted in this too so that any changes in the apparent band gap can be compared.

Another common technique to accurately measure the band gap is to plot dI/dV against V, which is done by taken the differential of the I-V data. The structure of the dI/dV against V is associated with the density of states. Tunnelling probability is considered to increase smoothly with tip bias therefore any changes are due to changes in DOS. DOS can be analysed using a WKB approximation and fitting straight lines to the slope. However at $V=0$, dI/dV diverges which prevents analysis of the electronic structure near the Fermi level. Feenstra et al. [96] argue that dividing dI/dV by I/V minimises the effect of the voltage on tunnelling probability and removes the influence of the tip sample separation. A correction factor is used to prevent a large spike at V=0.

STS can be influenced by a number of factors. Tip induced band bending can result in barriers to tunnelling and therefore reduces the current measured. Also thermal fluctuations in the system lead to changes in the Fermi function causing loss of spatial resolution.

3.1.3 The instrument

Figure 3.9 shows the STM system that will be used in the experiments carried out throughout this thesis. The STM is housed in an ultra-high vacuum (UHV) system made from electroflux stainless steel which allows samples to be prepared in situ and prevents contamination such as oxidation of prepared samples.

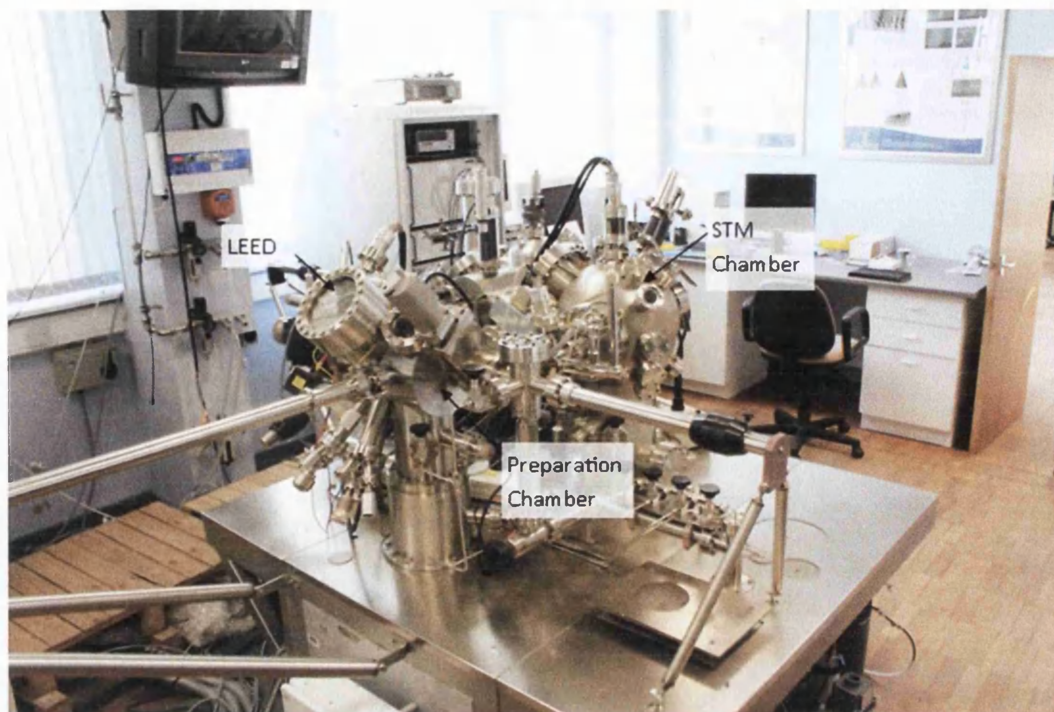

Figure 3.9: Omicron STM/AFM VT STM System at Swansea University showing the preparation chamber containing the LEED and STM chamber.

The pressure in the system is maintained at 10^{-10} mbar which is measured using ion gauges that consist of a coil or filament which produce electrons through thermionic emissions that are accelerated by a positively charged grid that surrounds a negatively charged collector [97]. Any gas molecules inside the grid that collide with the electrons become positively charged and are attracted to the collector which is negatively charged. The number of collisions with the collector is directly proportional to the number of molecules inside the vacuum chamber.

The filament in the ion gauge can only operate at low pressures since pressures above 10^{-3} mbar can cause it to burn out. Pirani gauges are used to measure higher pressures by measuring electrical resistance of a wire. When gas molecules collide with the wire heat is removed and the resistance decreases. Calibration shows a correlation between pressure and resistance.

The system shown in Figure 3.9 is maintained at UHV using a number of pumping methods which include roughing pumps, turbo pumps, titanium sublimation pumps (TSPs) and ion pumps. The system is also baked after it is vented to improve pump

down time after venting and when 10^{-10} mbar has been achieved the roughing and turbo pumps are switched off to prevent vibrations.

Vibrations (of the system) can cause loss of resolution when carrying out STM. STM systems have numerous methods to reduce vibrations including brackets on the side of the system that pin any wires running from the rack units, as well as air legs that reduce mechanical noise coupling to the system. The STM module sits on an Omicron eddy current dumping system that consists of a ring of copper fins that intersects a magnetic ring. Any vibration at this stage causes an eddy current to be created in the copper which generates an electric field that opposes movement that has created it and dampens the vibration.

STM requires an atomically sharp metal tip, usually made from platinum-iridium (PtIr) alloy or tungsten if used in vacuum. PtIr, usually in a ratio of 90:10, is used since it does not oxidise and can easily be cut into a sharp point by cutting at 45° while pulling the cutters away from the wire, however, PtIr wire is expensive and this method of cutting is not reproducible.

Tungsten is much harder than PtIr and frays when cut, therefore it has to be electro-chemically etched. All STM probes used in the experiments carried out in Chapters 4 and 6 were made using the same method based on that devised by Ibe et al. [23]. They state that ac etched tips have conical shapes with larger cone angles while dc etched tips have a hyperboloid shape which is much sharper and preferable for high resolution STM imaging therefore dc etching was used in this dissertation.

Electro-chemical etching involves lowering tungsten wire into a conductive beaker contain an electrolyte solution such as 2M KOH. A negative bias applied to the beaker causes the tungsten wire to be dissolved in the shape of the meniscus and produces a sharp probe. The etching step used to make the tips also has a circuit which turns off the voltage when a resistance change is measured which is an indication that the tip has etched.

Tungsten oxidises therefore the tip has to be cleaned in a vacuum system. There are several method of cleaning tips including heating and ion milling. Details of these methods have been given previously in Chapter 2.

Once the tip is in the system and the oxide has been removed, it is placed on the tip stage and approached onto the sample using piezoelectric tubes for fine movement and a stepper motor for course movements. The computer applies a set bias between the tip and sample and looks for the set point which is typically 0.1 nA - 1 nA. Once the set point current has been detected, the tip approach is stopped and the tip is said to be in tunnelling contact with the sample and scanning begins.

STM has two imaging modes: constant height and constant current. When using constant height mode, the tip is kept at constant height above the sample as it is scanned across the sample. The change in tunnelling current is measured and is used to create an image of current against tip position. The image can show topographical changes in the sample and changes in the electrical properties of the materials and details of this are given in Section 3.1.2. Constant height mode should only be used on flat, smooth surfaces to prevent the tip crashing into surface features.

Constant current mode relies on a feedback loop to measure changes in current adjusting the tip height to return the current to the set point. The feedback loop contains a series of amplifiers which gains have to be set to prevent the tip reacting too quickly or too slowly to changes in the sample.

3.2 Low Energy Electron Diffraction (LEED)

3.2.1 Introduction

LEED is a surface sensitive technique that involves bombarding a surface with a beam of low energy electrons and observing the diffraction pattern [98]. From the diffraction pattern it is possible to determine surface structure of crystalline materials [98].

The wavelike nature of electrons allowed Davisson and Germer to perform the first electron diffraction experiments in 1927 with somehwat apparatus similar to modern LEED systems [98]. However, due to low energies few reflected electrons from the sample surface contributed to the diffracted pattern and surface artefacts modified the diffraction patterns observed. Therefore it was not until the 1960s, with the development of vacuum technology and surface cleaning by ion bombardment and heat that LEED was commonly used [98].

3.2.2 Theory

LEED is a highly surface sensitive technique due the low penetration depth of low energy electrons. It is assumed that the intensity of the primary electron beam follows an exponential decay given by equation (3.8).

$$I(d) = I_o e^{-d/\Lambda(E)} \tag{3.8}$$

Where I_o is the initial intensity, d is the depth of penetration and $\Lambda(E)$ is the inelastic mean free path which is defined as the distance travelled by an electron before its intensity decreases by a factor of 1/e. The inelastic mean free path is heavily dependent on energy but not material therefore for a low energy electron it is typically in the range of 0.5-5 nm. This means that only a few atomic layers contribute to the diffraction pattern.

Low energy electrons are well suited to being diffracted by lattices of atomic dimensions since the wavelength of low energy electrons are of the order of atomic spacing. Using the de Broglie wavelength, equation (3.9) where λ is the wavelength, h is Planck's constant and p is the momentum of the electron. The momentum of the electron is calculated using equation (3.10). Where m is the electron mass, v is the velocity, E_k is the kinetic energy, e is the charge on an electron and V is acceleration voltage.

$$\lambda = \frac{h}{p} \tag{3.9}$$

Where

$$p = mv = (2mE_k)^{1/2} = (2meV)^{1/2} \qquad (3.10)$$

Using equations (3.9) and (3.10) an electron beam with energy 200 eV has a wavelength of 0.87 Å.

In the simplest case of a chain of atoms with separation a with the electron beam incident at right angles to the chain the backscattered electrons at a well-defined angle θ have a path difference d as shown in Figure 3.10.

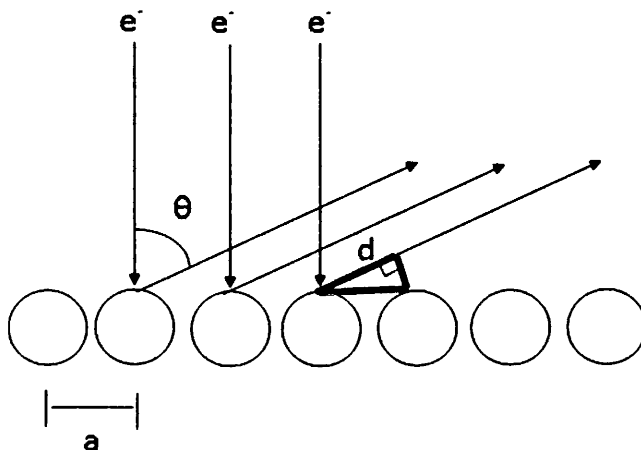

Figure 3.10: Diagram for back scatter electrons from a chain of atoms with separation *a*.

It is clear for constructive interference to occur at the detector, the path difference must equal an integral number of wavelengths. This condition is known as the "Bragg condition" and is given in equation (3.11). For large periodic arrays the diffracted intensity is only significant when this is satisfied exactly. This also means that the diffraction pattern is symmetric around θ = 0.

$$d = a\sin\theta = n\lambda \qquad (3.11)$$

An example of a LEED pattern from a fcc(110) (a two dimensional extension of Figure 3.10) surface is shown below in Figure 3.11. This is the first order diffraction pattern where n=1 in equation (3.11). It can be seen that the diffraction pattern shows the same rectangular symmetry as the sample surface but this is

stretched with interspacing a′. This stretching is due to viewing the reciprocal lattice in momentum space or k space.

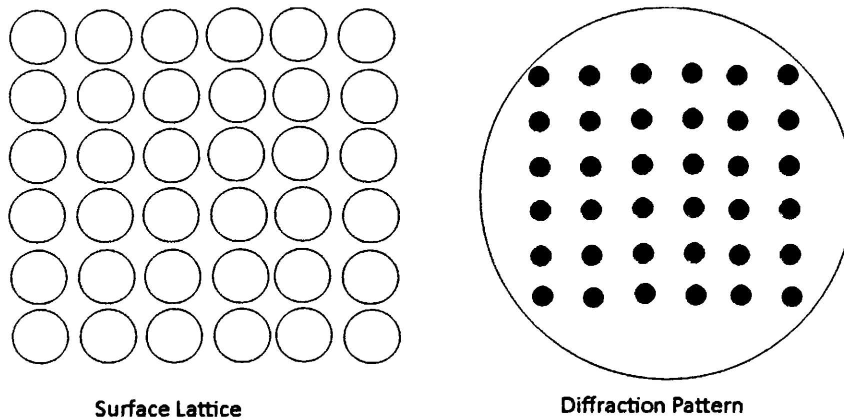

Figure 3.11: Diagram of a fcc(100) surface and the observed diffraction pattern.

K-space is the Fourier transform of real space. It is convention to define the wavenumber as the reciprocal of the wavelength, equation (3.12).

$$k = \frac{2\pi}{\lambda} \tag{3.12}$$

Using equation (3.9) in equation (3.12) it can be shown that k is a measure of momentum. Therefore the spacing observed in the diffraction pattern is stretched by a factor of 2π.

Using the Bragg condition in equation (3.11) and doubling the electron beam energy results in half the wavelength and observation of the second order diffraction pattern where n=2. This results in twice as many spots being seen in Figure 3.12.

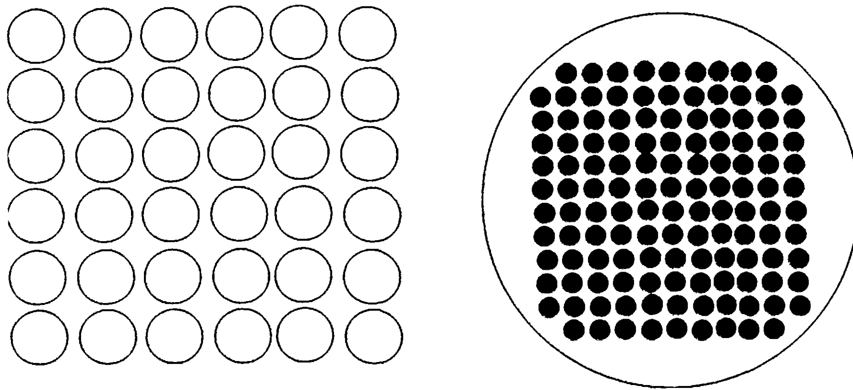

Figure 3.12: Diagram of a fcc(100) surface and the observed 2nd order diffraction pattern.

Assuming lattice vectors are $\boldsymbol{a_1}$ and $\boldsymbol{a_2}$ for the surface then the reciprocal lattice are $\boldsymbol{a_1'}$, and $\boldsymbol{a_2'}$ and are defined by equations (3.13).

$$\begin{aligned} \boldsymbol{a_1} \cdot \boldsymbol{a_2'} &= 0 \\ \boldsymbol{a_2} \cdot \boldsymbol{a_1'} &= 0 \\ \boldsymbol{a_1} \cdot \boldsymbol{a_1'} &= 1 \\ \boldsymbol{a_2} \cdot \boldsymbol{a_2'} &= 1 \\ \boldsymbol{a_1} \cdot \boldsymbol{a_1'} &= |\boldsymbol{a_1} \times \boldsymbol{a_1'}| cos\alpha \end{aligned} \qquad (3.13)$$

These equations imply that $\boldsymbol{a_1'}$, and $\boldsymbol{a_2'}$ are perpendicular and $\boldsymbol{a_1'}$, and $\boldsymbol{a_1'}$ have an inverse relationship. Also when α is 0 $\boldsymbol{a_1'}$ is parallel. Examples of real surface lattices and their corresponding diffraction patterns are shown below in Figure 3.13.

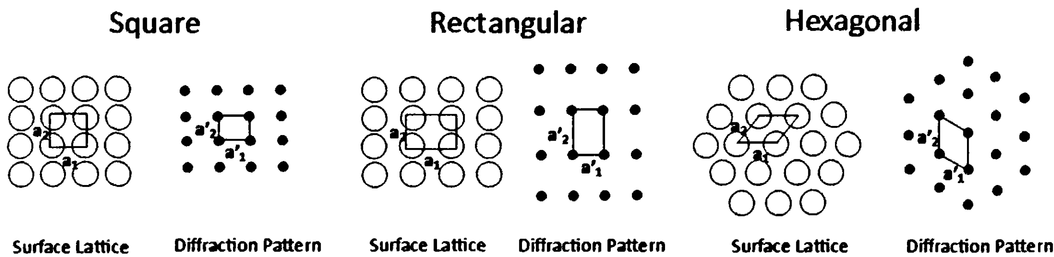

Figure 3.13: Diagram of some different surface lattices and their diffraction pattern.

Adsorbents on the surface also have an effect on the observed diffraction pattern. The adsorbent lattice, $\boldsymbol{b}$, and reciprocal lattice, $\boldsymbol{b'}$, follow the same equations (3.13) as the surface. Two examples of 2 x 2 adsorbent lattices overlaid on a fcc(100) surface are shown in Figure 3.14 below.

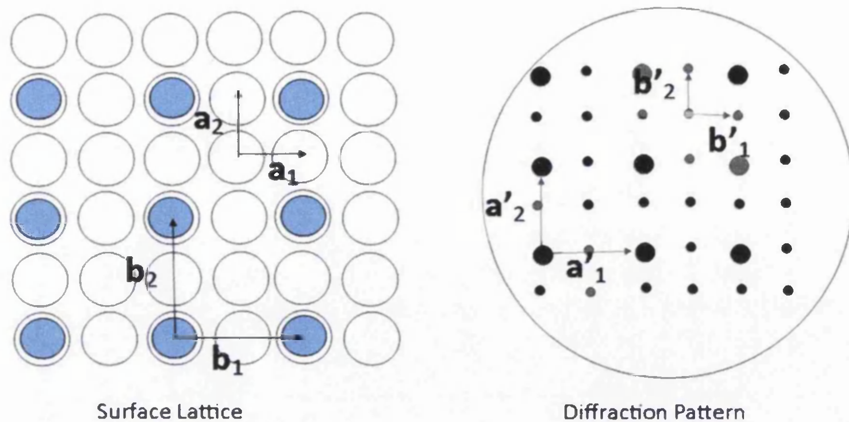

Figure 3.14: Diagram of 2x2 adsorbent overlaying fcc (100) surface and the diffraction pattern.

The diffraction pattern of the adsorbents lattice seen in Figure 3.14 shows the different atomic lattices contribute to different intensity dots. It can also be seen in Figure 3.12 that different surface lattices can produce the same diffraction pattern. Therefore it is not always possible to reconstruct the correct surface lattice from LEED patterns only. This was the case with the structure of silicon 7x7, which was not confirmed until the invention of STM to image the atomic structure.

3.2.3 The Instrument

The instrument used in Chapter 6 to determine whether the single crystal had been cleaned is situated in the preparation chamber of the system shown in Figure 3.9 which also houses the STM. The preparation chamber also contains the argon gun and heaters that were used to clean the sample (see Chapter 6).

LEED systems consist of an electron gun that produces a monoenergetic beam of electrons which is focussed using a series of lens so that it has a typical width of between 0.1-1 mm with energies ranging between 0-1000 eV. The gun contains a heated cathode made from tungsten that acts as an electron source. The beam is accelerated away from the cathode but a grid biased at up to -30 V controls the current from the gun.

A typical LEED setup is shown in Figure 3.15 and comprises a series of hemispherical grids and a phosphor screen that detects the diffracted electrons with the electron gun set in the middle. The grids filter electrons that have been in elastically scattered and lost less the 1-2 eV of their original energy and the screen is biased with a large accelerating voltage of the order 2 keV to provide the diffracted electrons with enough energy to excite the phosphor. A camera is then used to image of the diffraction pattern and analyse the spots positions. More modern systems use photo diodes instead of a phosphor screen that provide better resolution and accuracy.

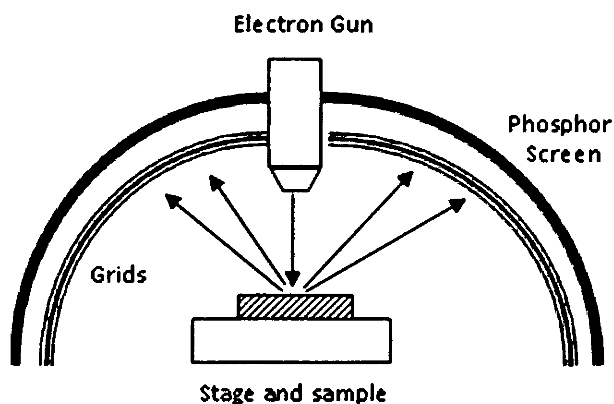

Figure 3.15: LEED setup showing electron gun, sample, filtering grids and phosphor screen.

3.3 Scanning Electron Microscope (SEM) and Energy Dispersion X-Ray Spectroscopy (EDX)

3.3.1 Introduction

Scanning electron microscopy uses a scanning beam of focused electrons to produce a 2D image of a sample and the Hitachi S4800 system used to in experiments described in Chapters 4, 5 and 6 has resolution of 1 nm. A SEM instrument can also be used for chemical analysis using energy dispersion x-ray spectroscopy (EDX) where incident electrons can cause electron transitions that produce characteristic x-rays which can be analysed to produce elemental maps and quantitative data [99].

M. Knoll first described the concept of scanning electron microscopy in 1935 and in 1938 M.von Ardenne added scanning coils to a transmission electron microscope (TEM) to make the first scanning transmission electron microscope (STEM). RCS Laboratories were the first to scan the surface of a solid sample with SEM in 1942. The Engineering Department at Cambridge University then made several prototypes and advancements during the 1950s to create the original models for modern instruments.

3.3.2 Theory

When the incident electron (primary) beam interacts with the sample many different types of electrons and photons are produced as shown in Figure 3.16. SEMs use electrons emitted from the sample to form an image. The electrons detected are classified as either back scattered electrons (BSEs), secondary electrons (SEs) or Auger electrons, which are discussed in the XPS section below. Incident beam electrons interaction with surface can also produce characteristic x-rays which are used in energy dispersive X-ray spectroscopy (EDX) to carry out chemical analysis.

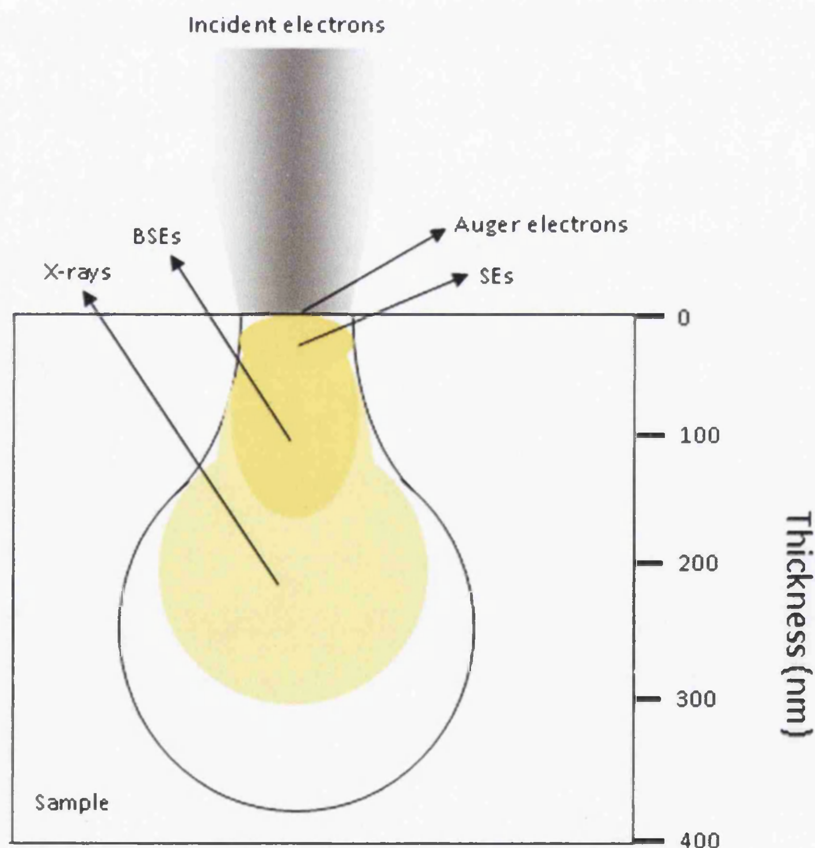

Figure 3.16: Schematic representing the processes resulting from electron bombardment.

BSEs are incident beam electrons that have been elastically scattered from the nuclei at the sample's surface that have high energies ranging from 50eV to near the energy of initial electron beam. Images produced using BSE can vary greatly depending on the detector position.

SEs are generated by ionization as a result inelastic collisions of the incident electron beam or BSE. SEs have less energy than BSEs, typically 3-5 eV and therefore only SEs produced near the surface are detected and therefore give better resolution of the surface compares BSEs. For this reason images were collected in the results chapters using SE detectors.

The quality of SEM images are dependent on the incident beam energy and in nanotechnology application low beam energies, 1-10 keV, are used to improve surface detail by reducing beam penetration depth and prevent sample charge and beam induced damage. However, higher beam energies are easier to focus due to less beam deviation through the column and also allow greater magnification. Unlike optical microscopes, SEM magnification is not a function of objective lens power but instead maximum magnification is dependent on spot size and raster of the beam. Therefore magnification is limited by the current supplied to the scanning coils. The maximum magnification of the Hitachi S4800 used in the experiments described in Chapters 4, 5 and 6 in 800 k.

Higher energy incident electrons can cause characteristic x-ray emission in the sample, in a process shown in Figure 3.17, that can be analysed to gain composition and stoichiometry chemical information. An x-ray is produced when an electron from a higher shell undergoes transition to a lower energy vacant shell in which an electron has been removed by the incident beam.

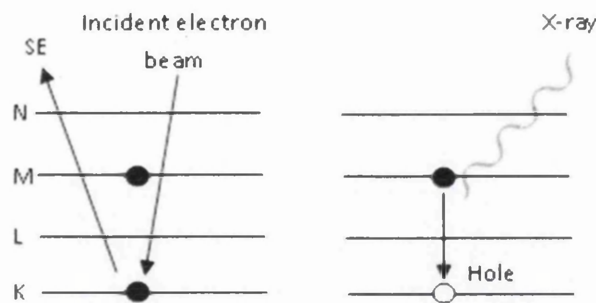

Figure 3.17: Characteristic X-ray generation process.

The energy difference between the two orbits is unique to each element and therefore x-rays emitted are unique and characteristic. The acceleration voltage is generally greater for EDX than SEM since the energy of the incident beam needed to remove the core electron must be greater than its binding energy.

There are typically 3 types of characteristic x-ray known as the K, L and M lines. Each is named after the shell in which the transition electron finishes, as shown in Figure 3.17. The K lines have the largest energy followed by the L lines and the M lines. X-rays are also produced when the incident beam is decelerated and deviated by the electrostatic field of a nucleus and are known as continuous x-rays or white x-rays. The energies of white x-rays are not unique to an element and contribute to the background and appear as an underlying hump. Characteristic x-rays are displayed as sharp lines.

The spatial resolution of EDX is dependent on the interaction volume and x-ray generation area which is shown in Figure 3.16. Penetration depth is dependent on the incident beam energy, lower beam energy results in a smaller x-ray generation area, however as discussed, the energy needs to be high enough to ionise the sample. Smaller atoms have lower binding energies and therefore the ionisation energy is less than larger atoms. This means that the incident electron beam energy can be reduced from samples containing smaller atoms.

EDX can be used to measure the ratios of elements in a sample by calculating the concentration, C_A, of each element. C_A is calculated by taking the ratio of the x-ray intensity, I_A, of the sample and the x-ray intensity, I_S, of a standard sample such as

silicon. The ratio is then multiplied by a factor to take into account the ZAF effects where the "Z" effect describes the variation in occurrence of the characteristic x-ray with the mean atomic number, the "A" effect describes the self-absorption of the characteristic x-ray until it escapes into the vacuum and the "F" effect describes the generation of characteristic x-rays caused by fluorescence excitation by other x-rays. This calculation becomes more complicated when the sample contains multiple elements, therefore it is normally carried out by computer software linked to the system. It is also common to carry out standardless quantitative analysis using a database of x-ray intensities of known elements.

3.3.3 The Instrument

The SEM, a Hitachi S4800, used throughout this dissertation is shown in Figure 3.18 and consists of an electron gun and a variety of electron detectors and an Oxford Instruments X-ray detector housed in a vacuum chamber.

Figure 3.18: Hitachi S4800 SEM with EDX X-ray detector at Swansea University.

An electron beam is generated using a cold field emission (CFE) gun which emits electrons from a sharp tip usually made from tungsten which has a high field applied

to it and operation is independent of temperature. However, to prevent the build-up of contaminants the tip has to be kept in vacuum of 10^{-8} -10^{-9} Pa and flashed.

Figure 3.19 is a diagram of an SEM and shows that the electron beam is then accelerated away from the source using an anode that has a bias of 1-30 KV and de-magnified by an electromagnet condenser lens that sits below the electron source. The beam is de-magnified further and focused onto the sample by the objective lens. Depending on the detector position, lens design and type changes to include magnetic lens and surround electrostatic lens. Lens aberrations limit the resolution of the system, if greater than the diffraction limit, and causes the electron beam to become elliptical, therefore a pair of quadrupole lenses are placed near the pole piece of the electromagnetic objective lenses to correct for astigmatism.

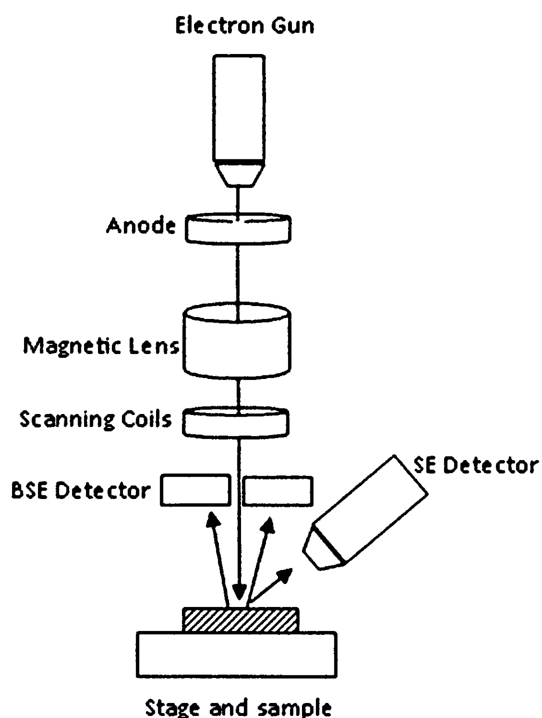

Figure 3.19: Diagram of the main components of a SEM.

The objective lens usually contains the scanning coil which is used to raster the beam by deflecting via the magnetic field and the Lorentz force so that it traces across the sample surface a rectangular area. This allows the software to generate the image from the positon of the electron.

There are two different types of detectors commonly used in SEM: Solid state detectors (SSDs) and Everhart-Thornley detectors (ETDs). ETDs are used on the Hitachi S4800. SSDs are made from semiconducting material that creates electron/hole pairs when impinged by electrons. The detector is biased so the electrons and holes flow in opposite directions causing charge to build up on an external electrode so that the scattered electron signal can be processed. SSDs can be made very thin and can be positioned under the pole piece of the objective lens and requires the incident electron beam to be of high energy and therefore suited best to back scattered electrons. ETDs consist of scintillators that emit light when high energy electrons impinge on it which is converted back to electrons using a photomultiplier and the signal amplified and processed to produce the image. ETDs have high gains with little degradation due to noise. The scintillators can be coated in a metal grid that can be positively biased to accelerate secondary electrons in order to give them enough energy to create photos in the scintillator. The grid can also be negatively biased to filter electrons so they only detect back scattered electrons.

Many SEMs also have an x-ray detector to carry out EDX which are generally SSDs made from p-type silicon diffused with Li^+ ions which are several millimetres thick so that energies ranging from a few hundred eV to tens of keV can be detected. The ion diffusion creates an intrinsic layer in which electron hole pairs are generated when x-rays are incident on the detector. The semiconductor is reverse biased so that the electron hole pairs migrate and cause a current which is amplified and its waveform shaped by a proportional amplifier and is sent to a multi-channel pulse height analyser. A multi-channel pulse height analyser detects the pulse heights which are proportional to x-ray energy.

3.4 X-Ray Photoelectron Spectroscopy (XPS) and Scanning Auger Microscopy (SAM)

3.4.1 Introduction

X-ray photoelectron spectroscopy, (XPS) is a surface sensitive technique that is used to quantitatively find the elemental composition, empirical formula (the simplest

integer ration of atoms present in a compound) and chemical and electronic states of a sample. X-ray bombardment of the sample causes emission of photoelectrons and analysis of the kinetic energy of these electrons allows information to be ascertained about the surface.

XPS relies on the photoelectric effect which was first observed by Heinrich Rudolf Hertz in 1887 and explained by Einstein in 1905, for which he won the 1921 Nobel Prize in Physics. Photoelectron velocity was first measured using a magnetic field hemisphere and photographic plates in 1907 but it was not until 1954 that a research group in Uppsala first carried out high energy resolution XPS of sodium chloride. In 1969 Hewlett-Packard produced the first commercial monochromatic XPS system and the 1981 Nobel Prize for Physics was awarded to K. Siegbahn for his work on a comprehensive study of XPS undertaken in 1967 and his work with Hewlett-Packard.

3.4.2 Theory

The photoelectric effect, originally worked on by Einstein, provides the basis of photoemission theory. Electrons are emitted from a surface with kinetic energy, E_K, when the energy of the incident x-ray beam, hv, is greater than the sum of the binding energy, E_b, and the work function, Φ and follows equation (3.14).

$$E_K = hv - E_b - \Phi \quad (3.14)$$

The photoemission process is described by a model called the Three Step Model which focuses on elastically scattered electrons; where the kinetic energy of electrons is conserved but the direction of travel is altered, but ignores main body effects such as electron-electron interactions and inelastic scattering. Three stages of photoemission are described which are all dependent on the initial electron energy, E, and the energy of the incident x-ray. The three stages are: photoexcitation of the electron, $P(E, hv)$, propagation through the solid, $T(E,hv)$, and escape from the solid surface into the vacuum, $D(E,hv)$[100-102]. These stages are combined in equation (3.15) to give the resulting intensity of the resulting photocurrent $I(E,hv)$.

$$I(E, hv) = P(E, hv)T(E, hv)D(E, hv) \quad (3.15)$$

P(E,hv) is calculated using the Hamiltonian energy operator, *H*, for a system perturbed by the absorption of a photon and is given in equation (3.16) [103]. A Hamiltonian is an operator used to calculate the sum of kinetic and potential energies of particles in a system.

$$H = \frac{1}{2m}\left[p + \frac{e}{c}A\right]^2 + V(r) \quad (3.16)$$

Where p is the momentum operator and is used to calculate the momentum vector of the electron and is given in equation (3.17), m is the mass of the electron, A is the vector potential of the electromagnetic wave that has perturbed the system, e is the charge on an electron, c is the speed of light and $V(r)$ is the self-consistent screening potential energy operator.

$$p = -i\hbar\nabla \quad (3.17)$$

When equation (3.16) is expanded it becomes:

$$H = H_o + W \quad (3.18)$$

Where W is the electron-radiation interaction Hamiltonian. By applying the dipole approximation only linear terms in A apply, therefore W given in by [104]:

$$W = \frac{e}{2mc}(pA + Ap) \quad (3.19)$$

and H_o is the Hamiltonian energy operator of an unperturbed system given by [104]:

$$H_o = \frac{p^2}{2m} + V(r) \quad (3.20)$$

The transition rate between the initial state and the final state due to the electron-x-ray interaction is given in equation (3.21) which is Fermi Golden Rule expression in 1st order perturbation theory [104].

$$P(E, hv) = \frac{2\pi}{\hbar} \sum_i |\langle \Psi_f | W | \Psi_i \rangle|^2 \delta(E_f - E_i - hv) \qquad (3.21)$$

Where Ψ_i is the initial state wavefunction, Ψ_f is the final state wavefunction, E_f is the energy of the final state and E_i is the energy of the initial state. δ is the Dirac delta function use ensure that there is energy conservation between ***hv*** and the transition energy $(E_f - E_i)$.

The excited electron has travelled through the sample to the surface. The electron will be scattered resulting in a modified photocurrent. Therefore $T(E, hv)$, is expressed in terms of the inelastic mean free path $\lambda(E)$, which is defined as the average distance an electron with energy E can travel through a solid before being inelastically scattered, and the distance, x, the photoelectron has to travel to the surface. If N_o is the number of the electrons excited at distance x, then the number of electrons that reach the surface without changing energy, N, is given by equation in (3.22) assuming no collection geometry.

$$N = N_0 e^{\frac{-x}{\lambda(E)}} \qquad (3.22)$$

Therefore the propagation probability can be written as equation (3.23) [100].

$$T(E, hv) = e^{\frac{-x}{\lambda(E)}} \qquad (3.23)$$

This propagation term describes why XPS is a surface sensitive technique. At low energies scattering is dictated by single particle electron excitations. At higher energies λ, becomes large than x and plasmon scattering arises and starts to dominate. Electrons with kinetic energy 40 eV typically have a mean free path of ~5 Å [105]. Therefore XPS typically samples the top most monolayers of the sample.

The probability of the electron escaping the surface of a conductor or semi-conductor, $D(E)$, is zero when electron energy is lower than needed to escape and one when the energy is higher. For insulators, charging must be considered as this alters the energy need for an electron to escape the surface. However, surface

charging is not considered by the three step model which is not applicable to conducting and semi-conducting samples. This means the final expression for the photoelectron current is given below in equation (3.24).

$$I(E,h\nu) = \frac{2\pi}{\hbar}\sum_i |\langle\Psi_f|W|\Psi_i\rangle|^2\,\delta(E_f - E_i - h\nu)e^{\frac{-x}{\lambda(E)}}D(E) \quad (3.24)$$

Figure 3.20 shows a XPS spectra of zinc with the core electron binding energies for Zn $2p_{3/2}$ and Zn $2p_{1/2}$ peaks. XPS can be used to determine structural, chemical or electronic information about the sample by analysing shifts in the observed peaks and the peak shape.

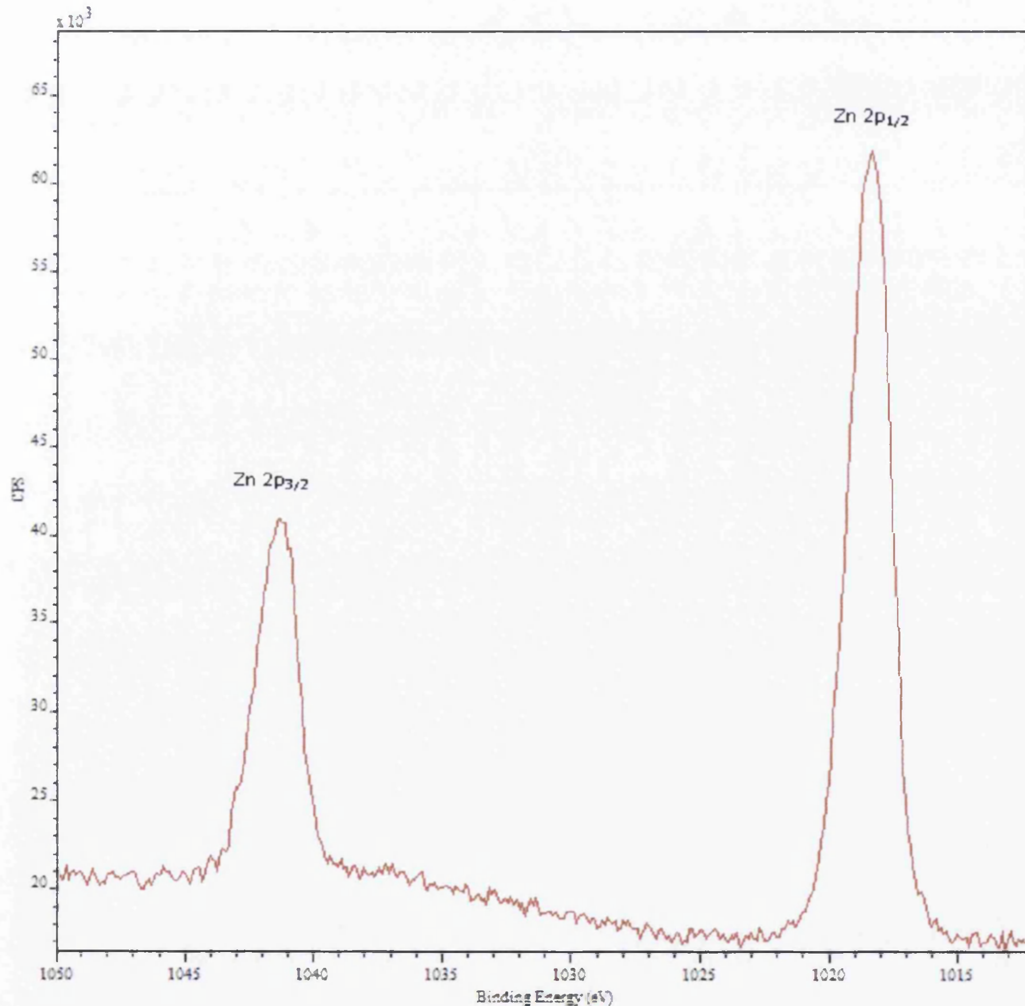

Figure 3.20: XPS spectra of zinc.

Properties of the atoms in the bulk of a sample differ from those at the surface due to termination of the periodicity. Due to relaxation and reconstructing to minimise the

surface energy the binding energies of the electrons emitted from the surface are different from those emitted from the bulk. Therefore the observed peak will be made of several surface components and bulk components. Bulk components can be minimised by changing the angle of the sample to the gun or the electron analyser [105]. Tilting the sample away from the detector increased the distance that the electron has to travel to the surface. Therefore the propagation probability term in equation 3.41 reduces resulting in lower emission from elements in the bulk of the sample.

Chemical shifts also causes a shift in the binding energy as the chemical environment is modified the valence charge is redistributed. This may result in a shift of the peak if all sampled atoms have undergone a reaction or the peak shape will change due to the introduction of an extra component. Curve fitting software, such as CasaXPS, is used to determine the contribution of each component. An example of curve fitting under an O 1s peak from a SiO_2 sample is given in Figure 3.21. It shows a fit of three components attributed to Si-O , O-H and C-O bonds.

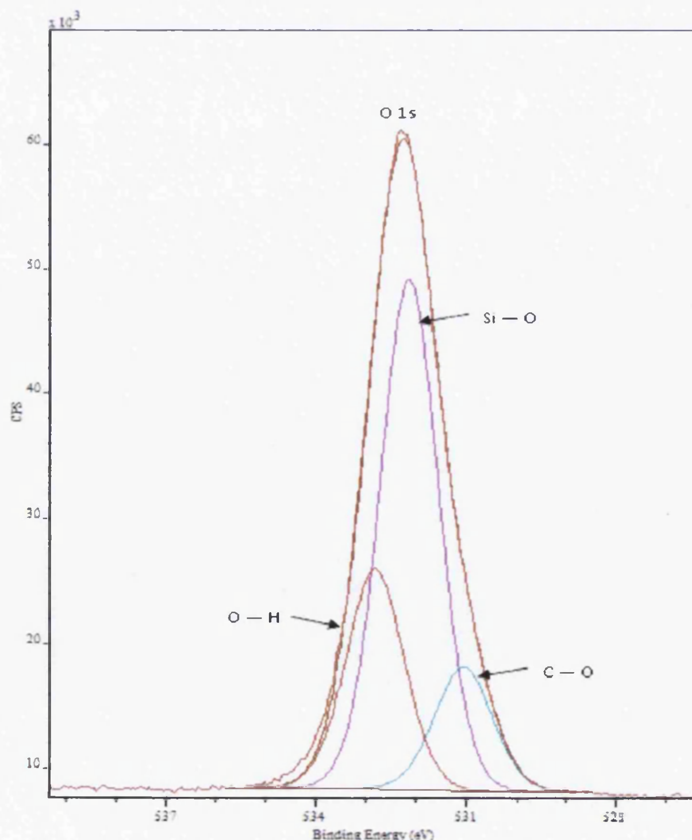

Figure 3.21: Example of curve fitting under an O 1s peak.

By comparing the ratio of different element peaks and applying a correction factor arising from the excitation cross section of the element it is possible to generate the chemical formula of the sample. The excition cross section, σ, arises from the $<\Psi_f$ W $\Psi_i>$ matrix element and is a measure of the interaction of the photon with the atom and its excitation. Yeh et al. have experimentally collected values for σ for individual core levels [106].

It is usual for the background to increase with binding energy. This background is caused by electrons that have been inelastically scattered while propagating to the surface.

XPS spectra often display satellite peaks and ghost peaks which can be reduced by using a monochromated X-rays [107]. Satellite peaks are caused by core electrons photo-excited by X-rays caused by transitions in the other than the main photo lines in the x-ray target. Ghost peaks are due to excitation arising from impurities in the X-ray source such as the exposed copper backing of the target.

3.4.3 Auger Microscopy

Auger electrons are ejected from shallow shells of an atom, shown in Figure 3.22, when the excess energy caused by an electron in an inner shell undergoing transition to a hole left by a photo ionized electron [105, 107]. These electrons have discrete energies and are collected together with the photoelectrons and give rise to Auger lines. The energy of Auger electrons are independent on the X-ray energy, therefore it is possible to discern Auger peaks from core peaks by changing the x-ray source.

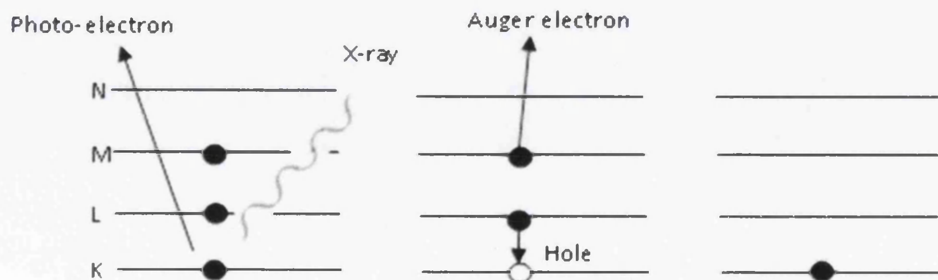

Figure 3.22: Auger electron process.

Auger electrons can also be generated by an electron beam instead of an x-ray source and can be rastered across the sample to produce spatially resolved chemical images of the sample as well as single point spectroscopy. These techniques are known as scanning Auger microscopy (SAM) and Auger electron spectroscopy (AES). However, using an incident electron beam to ionise the sample and result in back scattered electrons which can mask the shape of auger electron peak. This means chemical composition analysis cannot be performed by curve fitting but instead semi-analytical methods are used in Chapter 6 to analyse chemical shifts caused by annealing ZnO nanosheets. The obtained spectra and peaks have to be compared to those of known samples to give an indication of surface composition.

3.4.4 The Instrument

XPS instruments consist of an x-ray gun/tube/source and an electron energy analyser housed in a UHV system similar to that shown in Figure 3.9. X-rays sources produce x-rays by the bombardment of a target, either magnesium or aluminium, with high energy electrons. X-rays generated from aluminium targets have an energy of 1486.6 eV and a line width of 0.85 eV and x-rays generated from a magnesium target have an energy of 1253.6 eV and a line width of 0.7 eV. X-ray sources usually have both targets acting as anodes and are made from copper covered in a film of magnesium or aluminium and are cooled with water to prevent inter-diffusion of the targets and agglomeration that may cause the copper to be exposed which can lead to ghost peak as discussed above. An aluminium window is situated under the target anodes to prevent stray electrons impacting the sample.

There are two common electron energy analysers; cylindrical mirror analysers (CMA) and concentric hemispherical analysers (CHA). The XPS experiments carried out Chapter 6 used a CHA detector in the XPS system. A schematic of a CMA is shown below in Figure 3.23. CMA consists of 2 coaxial cylinders of radii r_1 and r_2, the outer cylinder is negatively biased while the inner is at ground. The photoelectrons enter at point S and are focused onto a photomultiplier at point F. The photomultiplier measures intensity and counts the number of the electrons

impacting at point F. The bias applied to the outer cylinder is swept so that electrons of different energies are focused onto the photomultiplier.

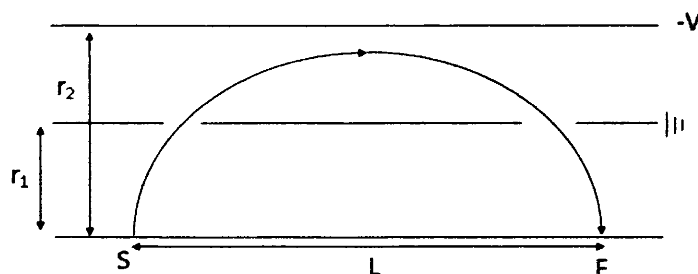

Figure 3.23: Schematic of a CMA.

The energy of the photoelectron, E, can be calculated using equation (3.25), where K is a characteristic constant of the detector.

$$E = \frac{Ke}{\ln\left(\frac{r_2}{r_1}\right)} V \tag{3.25}$$

A CMA, shown in Figure 3.24, consists of two hemispheres of radii r_1 and r_2. The inner hemisphere is biased at $-V_1$ and the outer at $-V_2$. There is also a third hemisphere of radius r_1 and biased at $-V_o$ that links the source, S, to the focus point, F.

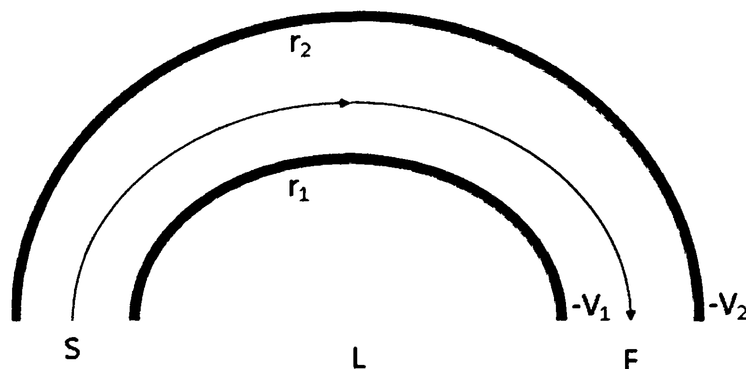

Figure 3.24: Schematic of a CHA.

A photomultiplier is situated at the focus point and by varying the difference between $-V_1$ and $-V_2$ it is possible to obtain directly the energy distribution of electrons passing through the analyser using equation (3.26).

$$E = Ke\Delta V \tag{3.26}$$

The x-ray source, sample and detector are housed in an ultra-high vacuum system to prevent changes to the surface of the sample caused by reactions with air and interference with electrons as discussed in the STM section.

3.5 Photoluminescence

3.5.1 Introduction

Photoluminescence is an optical technique that measures the photon emission intensity from a sample which has absorbed electromagnetic radiation [95]. PL is used to measure near band edge emission that gives a good indication of the band gap and can be used to detect defects.

3.5.2 Theory

When light is incident on a semiconductor, photons are absorbed by electrons which gains energy and move to an excited states. When the electron relaxes to a lower state/shell it loses energy in the form of a photon if the transition is direct. A direct transition occurs when the k-vectors of the higher and lower energy states are the same.

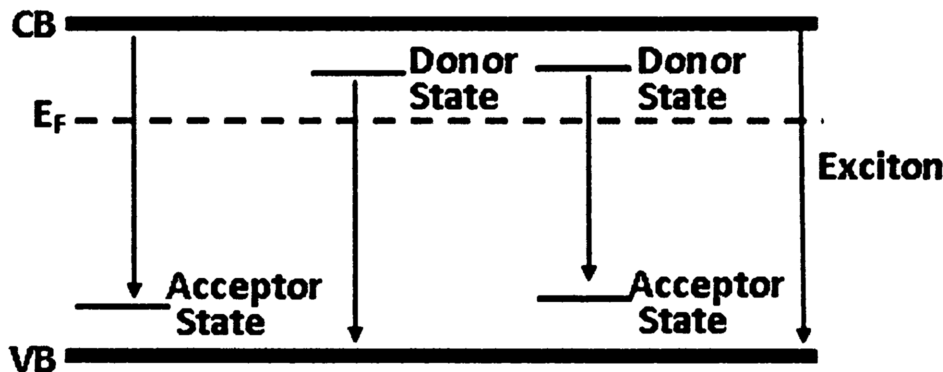

Figure 3.25: Possible photon emitting transitions.

Figure 3.25 shows the possible photon emitting transition when carrying PL. Light from the laser causes non-resonant photo excitation causing electrons to be promoted into a higher energy state and move from the VB into the CB. This causes holes to be left in the VB. Electrons form pairs with holes which are known are excitons. The electrons sit at the bottom of the CB and the holes at the top of the VB. When undergoing recombination the energy loss is nearly the same as the band gap. The difference in energy emitted and the band gap is due to a small binding energy of the exciton. This emission is known as the NBE and is mark on the PL spectra for ZnO nanowires in Figure 3.26 (this spectra is taken from the PL results discussed in Chapter 6). Photon emissions can also be caused by tranissions from the CB to acceptor states, donor states to VB and from donor states to acceptor states. Acceptor states are caused by defects that introduce holes into the lattice while donor states are caused by defects that introduce extra electron into the lattice and details of the defects in ZnO are given in Chapter 2. These transitions result in peaks the PL spectra known as the deep level (DLE) emission peaks which have higher wavelengths than NBE peaks. The DLE peak from ZnO nanowires is marked in Figure 3.26 and is made up of many transitions therefore curve fitting, similar to that of XPS data, is needed to analyse each defect energy.

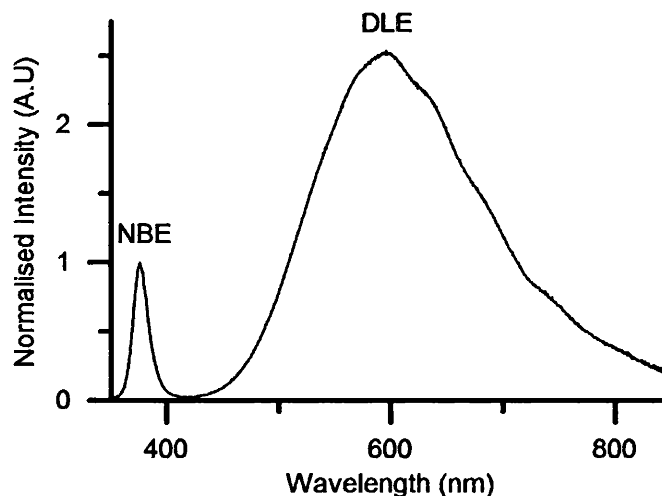

Figure 3.26: Room temperature PL spectra of ZnO nanowires with NBE and DLE peaks marked.

3.5.3 The Instrument

The set-up for PL is relatively simple and consists of a radiation source to excite the sample, usually a laser and a spectrometer to measure the emitted light. In order to excite an electron from the VB to the CB the energy of the incident photon has to be greater than the band gap. Therefore to ensure PL can be used on a range of samples with wide band gaps the lasers used have a low wavelength and are monochromatic. For the PL experiments carried out in Chapters 4 and 6, a He-Cd 325 nm laser was used. Figure 3.27 shows a schematic of the setup used.

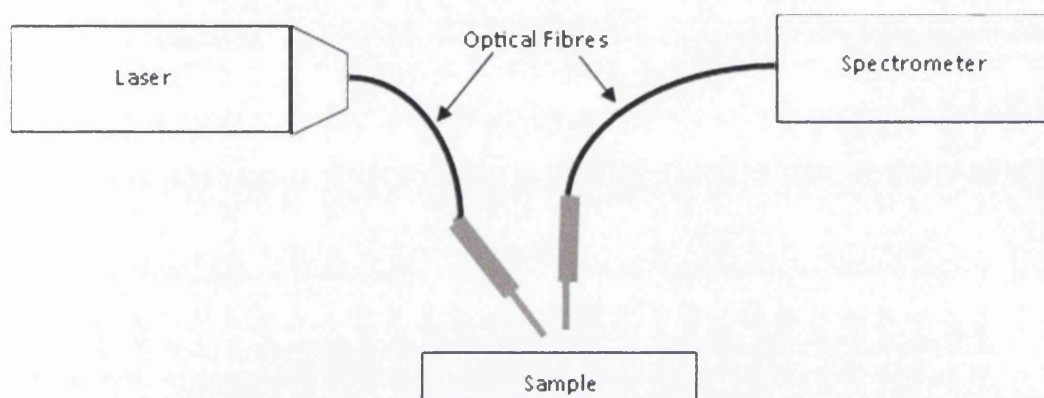

Figure 3.27: Schematic of PL setup

The light from the laser is directed onto the sample using optical fibres. This allows for spatial resolution of the spot size by focusing the light on an area of interest. The emitted light is also collected by an optical fibre positioned close to the excited area of the sample. This fibre takes the light to a photo-multiplier that measures the intensity of light over a range of energies. The resolution of the record spectra is dependent on the size of the energy interval of the detector.

Chapter 4: Tip Oxide Effects

This chapter reports the results of experiments designed to find a cleaning recipe for tungsten probes and understand the effects of tip oxide on STS and I-V measurements. It was discussed in Chapter 2 that the tip or probe plays a vital role in carrying out STM and STS and probe oxide can affect any measurements taken. The first experiment uses SEM and EDX to quantify the tungsten to oxygen ratio and tip diameter before and after direct current annealing for tungsten probes. Once a suitable recipe was found the second experiment uses it to understand the effects of tip oxide on STS measurement on cleaved GaAs. STS spectra were taken using tips with an oxygen coating then repeated after the oxide had been removed using direct current annealing. Modelling was then used to understand the reasons behind the observed shifts in the STS measurements. The final experiment reported in this chapter is a repeat of the second experiment, however, in this experiment the tip is brought in contact with the GaAs sample. This gives an insight into the effect of probe oxide on contact measurement such as 4 point probe which it is generally assumed is not affected by contact type between the sample and the tip. These results and discussions have been published in APL [108] and JAP [109].

4.1 Tip Cleaning Experiment

4.1.1 Method

A description of the theory of tip etching is given in Chapter 3 and for this experiment 0.25mm diameter tungsten wire was cut into pieces 6.5 mm long and placed in a tip etching rig, shown in Figure 4.1 below. The tip was lowered 2 mm, 1.75 turns, into a solution of 2 M potassium hydroxide (KOH) which was made by mixing 56.11g of KOH in 500 ml of DI water. 12 V was then applied across the tip to chemically etch the tungsten wire into a sharp tip with a hyperboloid shape. A circuit was used to turn off the power supply when a change in resistance was detected, using the design by Ibe et al. [23]. The tip was then removed from the solution and rinsed in DI water and viewed under an optical microscope; tips that were too long or distorted, i.e. did not have a hyperboloid shape, were rejected. The

tip was then spot welded onto an Omicron gold tip holder and placed onto the SEM sample holder that had been modified to hold the tip.

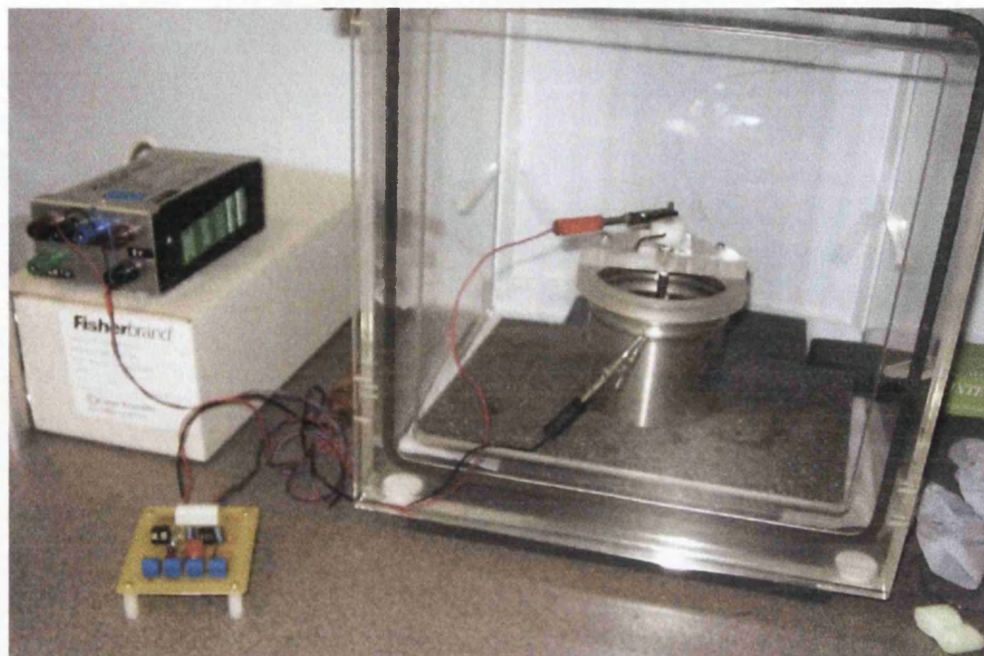

Figure 4.1: Tip etching rig consisting of a metal beaker to act as the anode and tip holder to act the cathode.

An Hitachi S-4800 FE SEM, shown in Chapter 3, with an Oxford Instruments X-Max 50 analyzer was used to image the tip at magnifications 150k, 50k and 250 times. EDX spectra were also taken along the tip at 150 nm intervals starting at the tip end to characterise the tungsten to oxygen ratio (W:O) after being calibrated using silicon. An accelerating voltage of 10 keV with a probe current of 10 μA was used to reduce the interaction volume the electron beam. The working distance at the end of the tip was ~15 mm and liquid nitrogen was used to remove contaminants from the SEM chamber via a cold finger. To ensure the EDX spectra was taken in the same place after each anneal a modified SEM sample holder was used.

The tip was then transferred into a modified Omicron Tip transfer plate that could be used to direct current anneal the probe, the design for which is similar to Yu et al's shown in Chapter 2 [11]. The tip was then placed in an Omicron VT AFM/STM system and left over night for the pressure to recover back to 10^{-10} mbar.

The tantalum contact was then lowered to just touch the top of the shaft of the tip and the current was slowly increased through the tip until the tip started to visable

glow by eye to ensure the current was running through the tip and not shorting on the system.. A current of 6 A was then passed through the tip for 8 s. The tip was allowed to cool for 15 minutes before being removed from the vacuum system and was placed back in the SEM sample holder. The tip was then re-imaged and characterized using the SEM and EDX. The tip was moved back into the Omicron vacuum system and the pressure allowed to recover to below 5×10^{-10} mbar. The tip was then flashed again at 6 A for 8 s then flashed at 7 A for 8 s after the pressure had recovered to below 5×10^{-10} mbar. Again the tip was removed and characterised. This process was repeated for 7.5 A and 8 A flashes. This was repeated for 6 tips.

To measure the temperature of the tip a piece of un-etched tungsten wire was spot welded onto a tip holder and placed into the modified tip transfer plate. The tip was then placed in the system and flashed at 6 A, 7 A, 7.5 A and 8 A. The voltage across the tip was measured during the annealing and the resistance of the tip was measured as the tip cooled as well as before annealing using a Keithley 2601 source meter. A linear resistivity approximation was used to calculate the temperature of the tip at each annealing current. The approximation is given in Equation 4.1 below

$$p(T) = p_0[1 + \alpha(T - T_0)] \quad (4.1)$$

Where p_0 is the known resistivity at temperature T_0, T is the temperature reached by the tip during annealing and α is a constant temperature co-efficient; for tungsten $\alpha = 0.0045\ K^{-1}$. Since the length and diameter of the wire is assumed to remain constant resistivity can be replaced with resistance, R, giving Equation 4.2.

$$R(T) = R_0[1 + \alpha(T - T_0)] \quad (4.2)$$

4.1.2 Results

Table 4.1.:Table of tip flashing current and temperature of the tip

Current (A)	8	7.5	7	6
Resistance before Annealing (Ω)	0.415	0.387	0.395	0.387
Resistance after Cooling (Ω)	0.363	0.360	0.368	0.371
Temperature during flashing (K)	2051	1714	1405	545

Table 4.1 above shows the temperature, calculated using equation 4.2, of the tip during flashing at different currents. The temperature of the tip before annealing was assumed to be the same as the temperature of the system which was measured to be 294.9 K. R_0 was chosen to be the lowest resistance after cooling, 0.360 Ω less the resistance of the cables used to measure the resistance which was found to be 4.08 x 10^{-3} Ω. Table 4.1 shows that the resistance before each anneal was higher than the lowest resistance after the annealing. It was observed that as the tip cooled the resistance would decrease, then the resistance would increase back up to the value before flashing. This is due to increased contact resistance cause by the dummy tip coming out of contact with the tantalum contact as it cooled and shrunk. The resistance during flashing was calculated using the voltage measured across the tip when the current was passed though the dummy probe. The voltage used was to calculate to resistance was allowed to stabilise so that overshot from the power supply was not a factor.

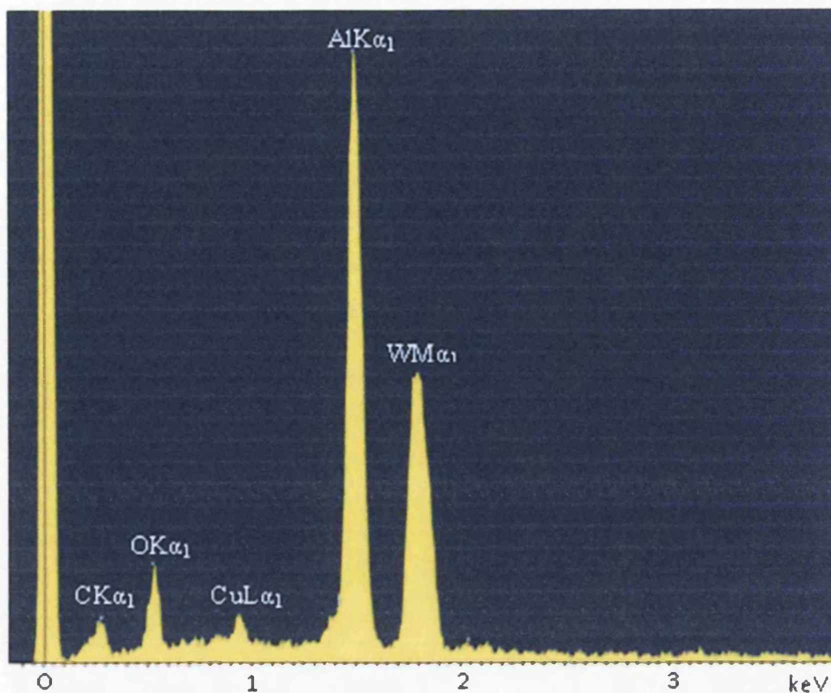

Figure 4.3: EDX spectra for a tip before annealing.

Figure 4.3 shows an example of the EDX spectra of the tip and shows that the elements present are tungsten, oxygen, aluminium and copper from the SEM sample holder and carbon contamination. For further analysis copper and carbon were removed from the spectra using the INCA software and a graph of the W:O ratio along the tip is shown in Figure 4.4 below.

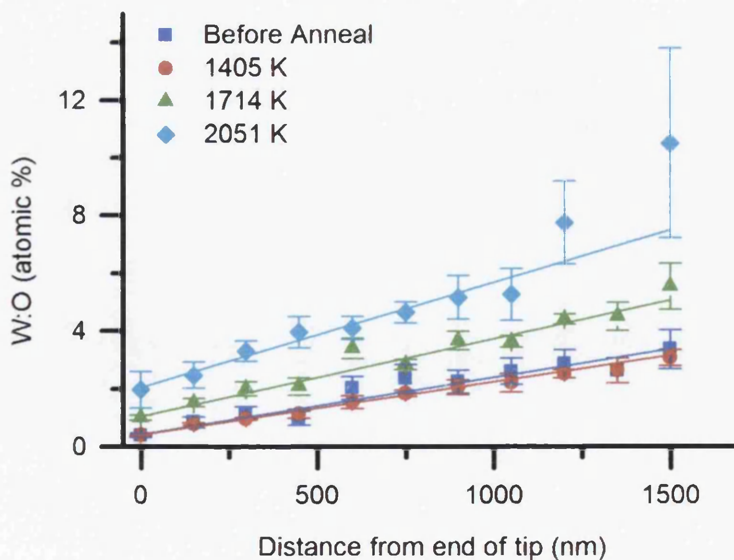

Figure 4.4: Tungsten to oxygen ratio measured by EDX as a function of distance along the tip, before annealing (0 A), and after annealing at 1405 K (7 A), 1714 K (7.5 A) and 2051 K (8 A). Error bars show the standard error, and each set has a least squared linear fit overlaid.

Figure 4.4 shows the W:O ratio against the distance along the tip from the apex for the different flashing currents. The W:O ratio was calculated using the INCA software using the atomic percentage measured by the EDX in the manner described in Chapter 3 and the errors bars were calculated using standard error. Figure 4.4 shows that the amount of tungsten relative to oxygen increased with the distance from the apex of the tip in a linear fashion shown be the linear least squared fit, R^2 values (calculated using Pearson's r in Orgin Pro): 0.970, 0.991, 0.950 and 0.915 for the before anneal, 1405 K and 1714 K and 2051 K respectively. It can also be seen that flashing the tip at higher currents sublimated more oxygen from the tip and is shown more clearly in Figure 4.5 below.

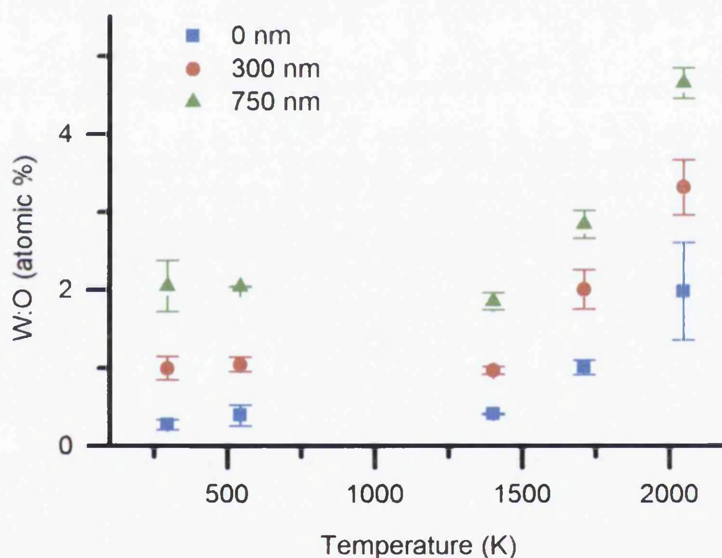

Figure 1.5: Tungsten to oxygen ratio measured by EDX as a function of the tip annealing temperature, at the end of the tip (0nm) and at 300 and 750 nm from the tip end. Error bars show standard error.

Figure 4.5 shows that the W:O ratio is increased when the tip is annealed at higher temperatures for all distances from the probe's apex. The graph shows that, for all points along the tip, annealing at 545 K (6 A) does not reduce the amount of oxide. Annealing at 1405 K (7 A) does reduce the average amount of oxide present on the tip, however, the overlapping error bars show that this reduction is not statistically significant. Flashing the tip at 1714 K (7.5 A) and 2051 K (8 A) does result in a statistically significant increase in the W:O ratio. This is does not agree with some of results discussed in Chapter 2 who annealed their tips to less than 1700 K to

remove the oxide [7, 8]. However, the results do agree with those who annealed their tips above 1700 K [6, 28, 29]. The results shown in Figure 4 also show that not all the oxide is removed from the end of the tip as the ration has not gone to infinity.

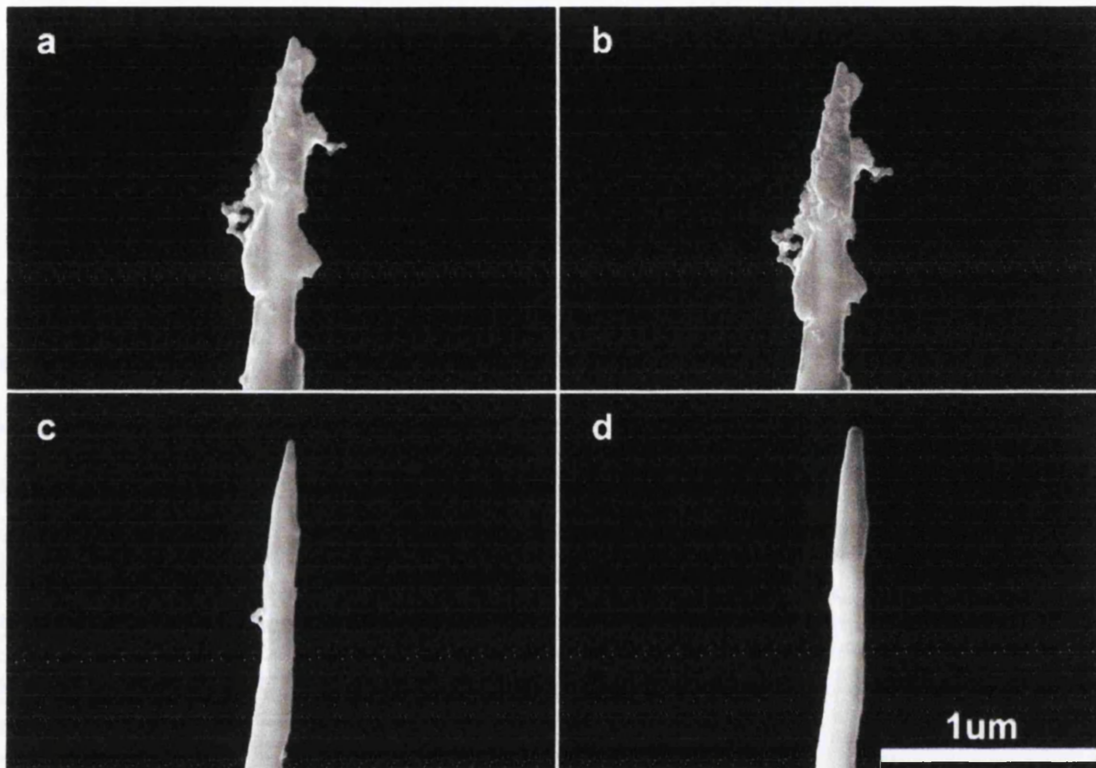

Figure 4.6: SEM images of an aged tip (a) before annealing, and after annealing at currents of (b) 7 A, (c) 7.5 A and (d) 8 A [108].

The SEM images, shown in Figure 4.6, show an aged tungsten tip before annealing and after flashing at 1405 K, 1714 K and 2051 K. The images are in agreement with the results in Figure 4. They show that flashing the tip at 1405 K (7 A) does not significantly reduce the amount of oxide present while flashing at 1714 K (7.5 A) does remove most of the oxide that was present on the probe. Annealing the tip at 2051 K (8 A) further reduces the quantity of oxide on the tip, however, the end of the tip appears broader due to atomic diffusion.

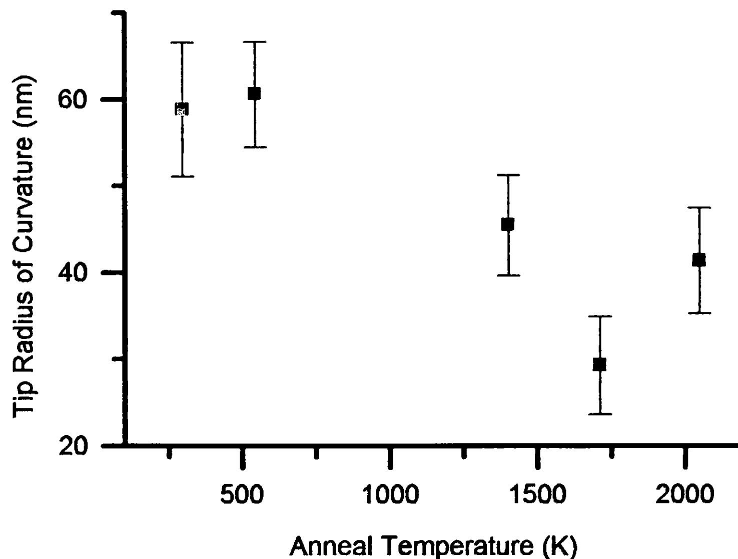

Figure 4.7: Tip radius of curvature measured using SEM, before being annealed (298 K) and after annealing for eight seconds at 545 K (6 A), 1405 K (7 A), 1714 K (7.5 A) and 2051 K (8 A). Error bars show the standard error.

Figure 4.7 shows the radius of curvature at the end of the tip that was measured by fitting a circle to the SEM images and measuring the radius. The results show that flashing at 545 K (6 A) does not significantly change the radius of the tip, this is due to the temperature being too low to sublimate the oxide. This is a reduction in tip radius when the tip was flashed at 1405 K (7 A) and a statistically significant reduction, P-value 0.0214, when the tip was annealed at 1714 K (7.5 A). This is caused by the significant reduction in tip oxide seen in Figure 4 and Figure 5. Figure 4.7 also shows that on average the diameter of the tip increased when the tungsten probe was annealed at 2051 K although the increase is not significant. This Figure agrees with Staufer et al. [9] who found that tungsten probes blunted at 2000K but is lower than Kim et al. [29] who found that blunting occurred above 2500 K.

4.1.3 Conclusion

In order to sublimate the oxide from a tungsten STM tip, the probe has to be annealed to at least 1714 K or flashed at 7.5 A. Flashing at higher currents will remove more of the oxide from the surface of the probe and increase in the W:O ratio. However, when the tip was flashed at 8 A, which was calculated to be 2051 K, it was seen that the end of the tip started to broaden. Therefore there is a trade-off between the sharpness of the STM probe and the amount of oxide covering the end of the tip. The effects of tip oxide on image quality has been observed in the

literature and it is necessary to have a sharp tip to obtain high resolution images. However, there has been little work done on how the quantity of oxygen surrounding a tungsten probe affects the electronic data than can be obtained by STS.

4.2 Effect of oxide on scanning probe microscopy (SPM) tip when carrying out STS

4.2.1 Method

The experiment reported above showed that a small amount of probe oxide remains after cleaning, however, little work has been done to understand the effects of this oxide on STS measurements. Knowing these effects is important in analysing the results in Chapter 6 when STS was carried out on ZnO nanowires after they were annealed. To understand the effect on measurements a tip was etched and characterised in the same way as previously described and placed in the UHV system. Highly doped gallium arsenide (GaAs:Zn), with doping concentration 9.2×10^{17} cm^{-3} from the Institute of Electronic Materials Technology, was thinned to a thickness of 250 μm by sticking a 10 x 2.5 mm wafer onto a grinding block with a 250 μm recess with paraffin wax. After grinding the sample using sand paper and water the sample was freed from the grinding block using hot trichloroethylene and cleaned in acetone and then isopropanol. The thinned sample was then placed in a custom built cross sectional sample holder and loaded in the Omicron VT system and the sample was cleaved using the system's wobble stick to leave a protruding, clean, flat surface.

The pre-annealed tip was then approached onto the GaAs surface using a gain of 10%, set point current of 0.1nA and a gap voltage of +3 V. The gain was then reduced until a stable scan was achieved and spectroscopy was carried out in a ten by ten grid while checking for continuity in the spectra and the image; the scan direction remained constant to ensure that the tip properties did not change during the measurements.

The sample was then moved to another UHV chamber to prevent contamination during the tip flashing. The tip was flashed at 6 A (545 K), 7 A (1405 K) and then

7.5 A (1714 K) for 8 sec, flashing the probe at higher currents or temperatures greater than 1714 K has been found to cause blunting of the tip. After the tip had cooled and the pressure in the chamber had recovered, the sample was moved back onto the scanning stage and rescanned with the clean tip. The tip was then taken out of vacuum and characterised using SEM and EDX to ensure that it had been cleaned. This was repeated for three more tips and twice on low doped GaAs 1.7×10^{16} cm^{-3}.

In order to analyse and understand the results a model was created by Ogla Kryvchenkova [12, 110]. The 2D structure of the tip-sample system was modelled self-consistently using the simulation tool Atlas [110, 111][110, 111][110, 111][110, 111][110, 111]. A regular triangular mesh was used, with the tunnelling current calculated using a direct quantum tunnelling model by Tsu et al. [112, 113]. The tunnelling probability was calculated according to the Gundlach formula for a trapezoidal potential barrier [114]. Both the incident and transmitted currents were taken into account and Schrödinger's equation was solved in the effective mass approximation [115]. The tunnelling current through the gap was allowed only via a tunnelling process, and homogeneous (reflecting) Neumann boundary conditions were used for the non-contact areas. Dirichlet boundary conditions were used for the tungsten tip and the sample contact. Mid-band gap surface states could be accounted for in this model, but the *in situ* cleaved atomically flat (110) surface of GaAs contains no mid-band gap surface states and they were not included.

WO_3 is a wide band gap semiconductor, and for un-cleaned tips if tunnelling was taking place through the oxide at the tip apex, the WO_3 band structure would convolve with the sample band structure to produce spectra with a much wider apparent band gap. This is the opposite of what we observe experimentally, and later we will show that the tip apex behaves predominantly as a metal.Therefore, it was found that during the initial tip approach the oxide coating is mechanically removed to exposed metal tip apex due to contact with the sample before tunnelling initiates. Direct current annealing at 1714 K is high enough to sublimate the oxide and is low enough to prevent blunting of the tip, but a residual oxide layer remains. In line with this, and our SEM and EDX results discussed in the previous section of this chapter, a model was constructed with a 32 nm diameter tip with a 1 nm WO_3 layer

and after annealing the tip shaft oxide reduced to 0.3 nm, with the tip apex exposed for both. This structure was used for all simulations is shown in Figure 4.8.

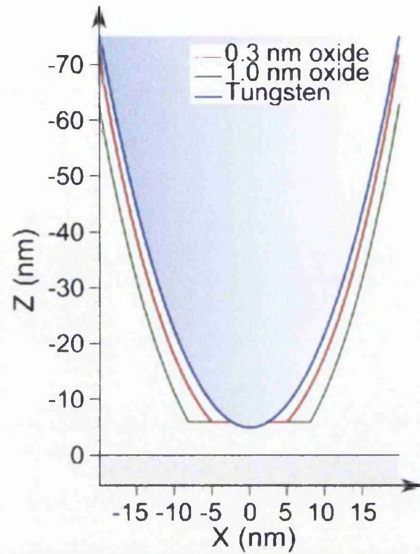

Figure 4.8: Physical model of the tip, with an exposed metal apex and oxide coated shaft (image produced by Olga Kryvchenkova [12]).

4.2.2 Results

For the high doped sample shown in Figure 4.9a, the electron transport in (positive gap voltage) is observed to shift after probe shank oxide removal, where simulations find that the probe field is high enough to induce localised surface depletion creating a probe-induced quantum dot with empty discrete states in the VB above the Fermi level.

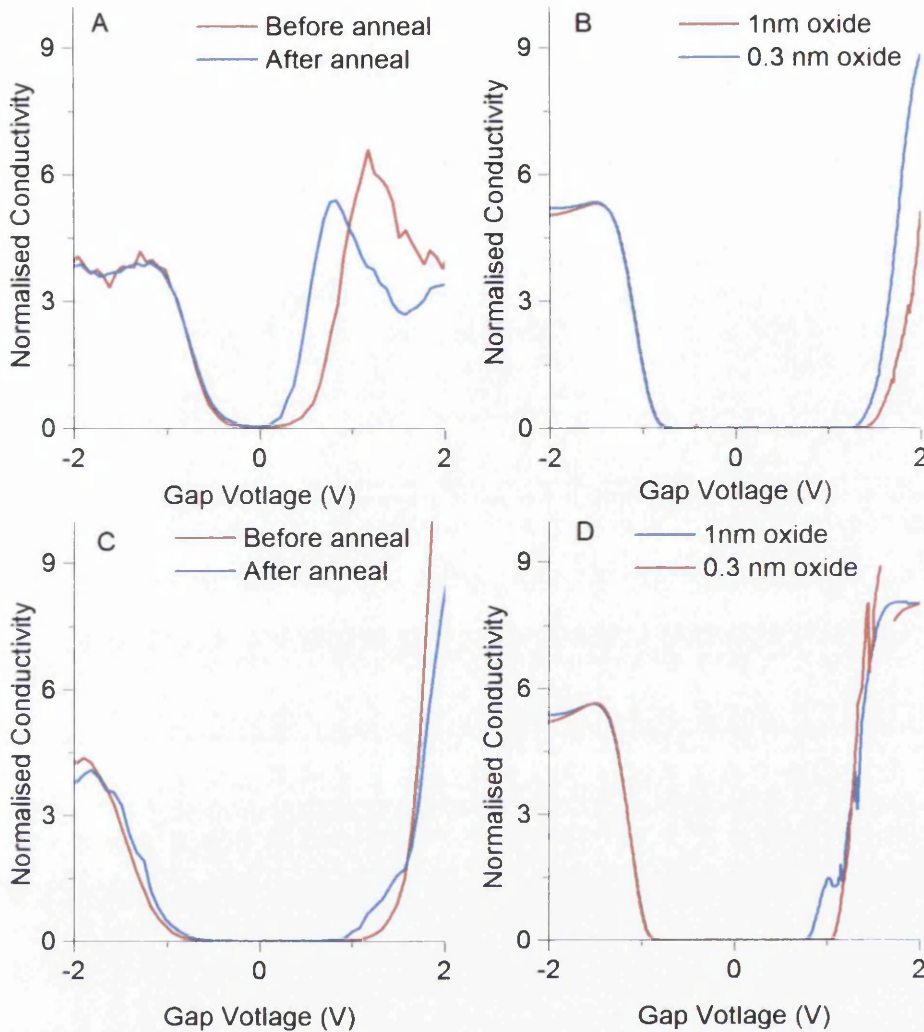

Figure 4.9: Normalised conductivity versus gap voltage (sample bias) with a denominator offset constant c = 0.02 and a rolling average of six for non-contact measurements on highly doped GaAs (a) experimental and (b) simulation and low doped GaAs (c) experimental and (d) simulation. Simulation data courtesy of Olga Kryvchenkova [12]

An example is shown in Figure 4.10, where at +1.8 V for the highly doped sample, localised band bending is larger with the thicker probe oxide before annealing, see Chapter 3 for a description of band bending. This leads to discrete states above the Fermi level, Figure 4.10 b) in the VB which the probe electrons tunnel in to before the voltage is high enough to tunnel in to the CB. Thermal broadening, where the Fermi function is non-abrupt at room temperature, means the additional states are not resolved individually but still add to the overall current.

For low doped GaAs, these long range electrostatic interactions are essentially already so high that there is little difference when the probe oxide is changed. The only exception is a shoulder cantered around 1 V caused by the on-set of the quantum dot, which appears earlier when the probe oxide has not been reduced.

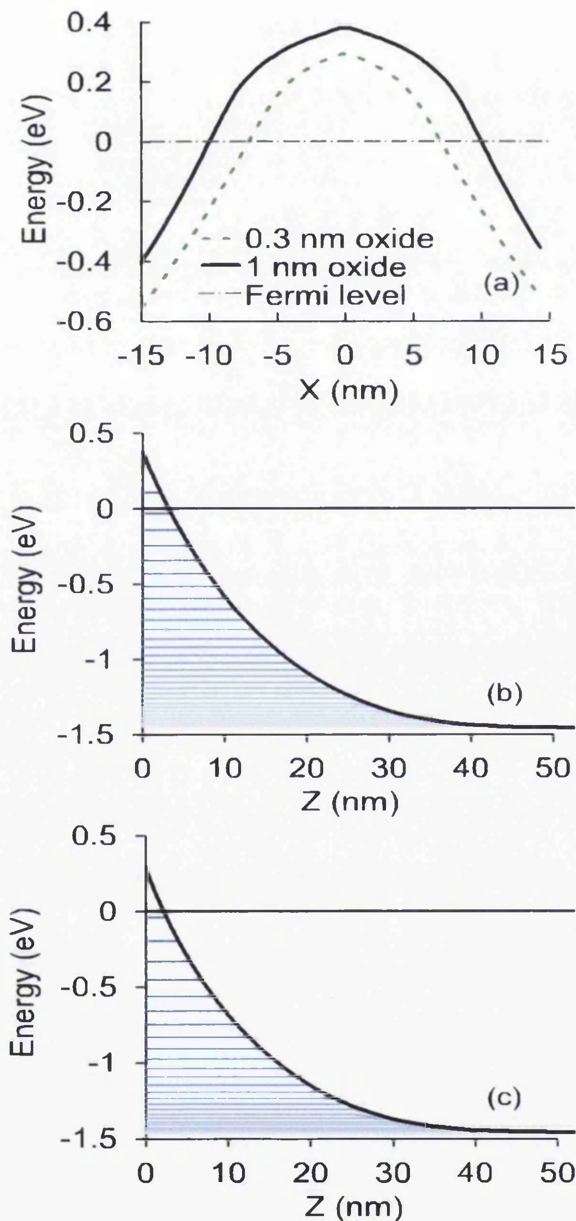

Figure 4.10. For highly doped GaAs at +1.8 V gap voltage, simulations show (a) VB profile under the tip before and after annealing, with the VB profile orthogonal to this in the z-direction directly under the centre of the tip with discrete states (b) before tip annealing and (c) after annealing. Image produced by Olga Kryvchenkova [12].

Both experimental and simulated results show the same effect and any discrepancy arise from the tip shape and oxide profile..

4.3 Effect of Oxide on SPM tip when carrying out I-V

4.3.1 Method

It was seen that probe oxide has an effect on STS therefore is it possible that a similar effect would affect contact measurement such as the two point probe measurement taken on nanowire and nanosheets in Chapter 6. To assess the effects of probe oxide tips, highly doped GaAs samples were prepared in the same way as above. In order to bring the tip into contact with the sample the tip was lowered 0.1nm and the voltage swept between -2 and +2 V until a change was observed in the behaviour of the I-V curve. The equation 3.18 in Chapter 3 shows that the tunnelling will increase exponentially with decreased tip sample separation, therefore it is assumed that when the measurement jumped away from this trend that the tip was in contact. It was found that the tip needed to be approached 0.5nm to be in contact with the sample and a macro was written using the Scarla software so that when a STS point was taken, the tip would approach 0.5 nm, wait, sweep the voltage then retract 0.5 nm and wait to stabilize before continuing the scan. As before 100 spectra points were taken per sample and 2 samples and tips where studied.

For the contact modelling, again carried out by Ogla Kryvchenkova [12], when tip and sample form a Schottky contact the thermionic emission and surface recombination velocities are calculated [116]. The universal Schottky tunnelling model is used to estimate the tunnelling current through the Schottky barrier, where the localised tunnelling rates are calculated close to the metal-semiconductor interface for both electrons and holes [117, 118].

4.3.2 Results

The conductivity both experimentally and in simulation increases after the probe shank oxide is reduced. The simulations and experimental results contain the same features with quantitative agreement. Discrepancies arise from the probe geometry estimated from SEM images and non-uniform oxide formation which was modelled as uniform. Simulations find that the creation of a near-intimate contact between the

probe and sample forms a Schottky contact with a fixed barrier height for both thickness of probe oxide. This is caused by the high concentration of electrons in the metal compared to the semiconductor sample. Therefore, the Fermi level of the metal is pinned fixing the height of the contact barrier. However, the different shank oxide profile before and after cleaning alters the electrostatic interaction with the sample, changing the shape and width of the barrier, giving rise to the altered transport shown. Importantly, the change for electron transport into the sample (positive gap voltage), where the presence of the Schottky contact means tunnelling dominates, is much more pronounced than the change observed for electron transport out of the sample (negative gap voltage), where thermionic emission dominates. This result confirms that the barrier for current into and out of the sample for probes in the four point probe method would be unequally affected by probe shank oxide, and could lead to a violation of the assumptions which make four point probe measurements independent of contact resistance.

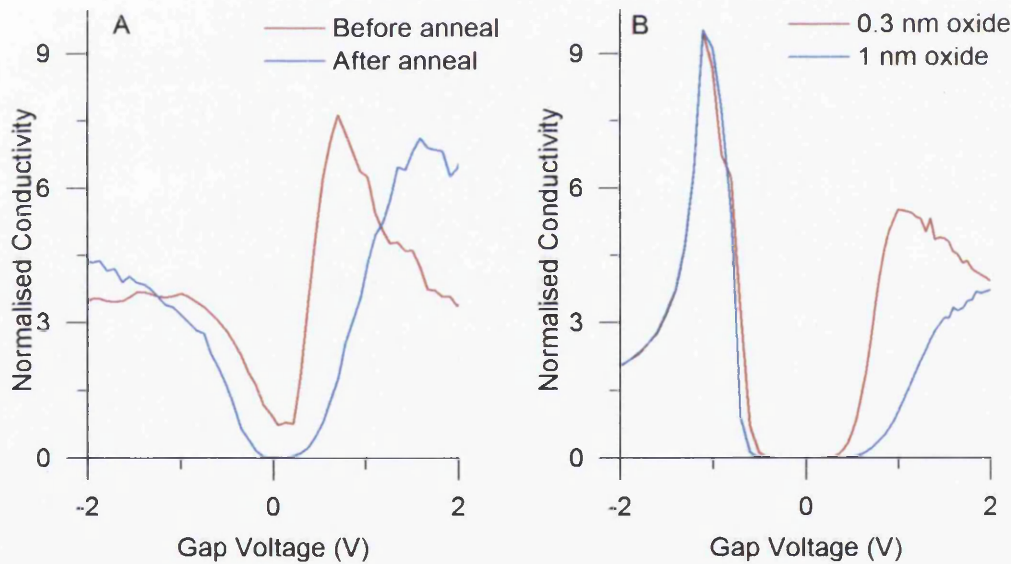

Figure 4.11. Normalized conductivity as a function of applied bias with a denominator offset constant c = 0.02 and a rolling average of six for contact measurements on GaAs A) experimental and B) simulation. Simulation data courtesy of Olga Kryvchenkova [12]

4.3.3 Conclusion

Both experimentally and computationally the effects of probe oxides on non-contact STS and contact I/V when the probe oxide is controllably reduced has been explored. Both the spectroscopic and I/V curves shift when the tip oxide is reduced. When in non-contact regime, the main shifts in the spectra occur when the sample is in depletion, where a tip-induced quantum dot has been created in the sample below the tip. The shape and size of the induced quantum dot is altered by the electrostatic field from the tip, which is governed by the oxide coating. When an oxidised tip is used, the resulting tip induced quantum dot causes empty discrete states above the Fermi level in the VB which results in increased tunnelling. When the oxide coating is reduced, the smaller tip induced quantum dot does not create discrete states above the Fermi level. A similar shift in the spectra observed by Shen et al. and Clemens et al. may be due to a similar effect as that observed here [26, 27]. In their case, the oxide layer deposited on the InGaAs sample reduces the effect of the electric field and reduces the tip induced band bending which causes the CB edge to shift towards the Fermi level.

It was also observed that a different mechanism governs contact measurements. In the non-contact regime, the height of the barrier played a key role in modifying tunnelling behaviour by changing the depth of the tip-induced quantum dot. However, in contact regime, the height of the barrier is pinned and the shape of the barrier instead plays the most important role.

Therefore local probe spectroscopic measurements are highly dependent not only on the shape of the probe, but also on the shape and characteristic of the oxide layer. By modifying the electrostatic field from the probe, the oxide controls the tunnelling regime which causes shifts in spectroscopic measurements in both contact and non-contact measurements and must be included in any description of local probe measurements. In the experiments carried out in Chapter 6, all the tips were annealed at 7.5 A using the recipe found in the first experiment to ensure that tips were reproducibly cleaned so that there were no changes in probe oxide that would affect the STS and 2 point probe measurements on the ZnO nanowires and nanosheets.

Chapter 5: ZnO Nanowire Growth

This chapter reports the results of experiments designed to understand and tailor the growth of ZnO nanowires with the hope to be able to grow suitable nanowires for use in the experiments described in Chapter 6. This chapter consists of four experiments each examining a component of growth: precursor concentration, temperature of growth, time of growth and substrate material. The first two experiments, precursor concentration and temperature of growth, are a continuation of my MSc dissertation in 2011 [119] and the results have been analysed in line with recent literature and published in two conference papers in 2012 [120, 121]. These experiments looked at varying the concentration of zinc nitrate to HMTA by changing the quantity of zinc nitrate and varying the temperature of water baths in which the growth occurs. The third experiment relating to time was presented by myself at the 2012 12th IEEE Conference on Nanotechnology and examines the stages of nanowire synthesis. The final experiment on substrate material is a continuation of work undertaken by Richard Brown at Swansea University during my own research [14]. I have continued the experiments using different metals: chromium, tungsten and titanium. All experiments where characterised with SEM to observe any changes in the morphology of the nanowires. PL was also carried out on the temperature experiment to assess any changes in defects.

5.1 The Effect of Precursor Concentration on ZnO Nanowire Growth

5.1.1 Method

As discussed in Chapter 2 Sugunan et al. suggested that the concentration of HMTA will affect the diameter of the ZnO nanowires synthesised [122]. To assess this a PTFE beaker was filled 500 ml of deionised (DI) water was heated in a Grant 5 Litre water bath to 90 °C. 3.72 g of ≥99.0% zinc nitrate hexahydrate (Sigma Aldrich) and 1.75 g of ≥99.0% HMTA (Sigma Aldrich) was dissolved in 100 ml of DI water and stirred using a magnetic stirrer for 10 minutes. The solution was made up to 500 ml using the pre-heated DI water to create a solution containing 31 mM with a 1:1 ratio

of each precursor and placed back in the water bath. A piece of silicon with a 30 nm seed layer of ZnO was floated seed layer down on the solution and left for 6 hours. The sample was then removed from the solution and rinsed in DI water and allowed to dry in air. This method was repeated varying the amounts of zinc nitrate while keeping the mass the HMTA at 1.75 g so that the molar ratio of the solution varied from 2:1 to 1:2 to create a total of 8 samples.

The seed layer was deposited onto n-type silicon that was cut into 1 cm^{-2} pieces and was cleaned by sonicating in acetone for 10 minutes, agitated with a cotton bud and then sonicated in isopropanol for a further 10 minutes. The silicon was then placed in a Lesker PVD 75 with a ZnO ceramic target and pumped down to 10^{-5} torr. 55 sccm of argon and 5.5 sccm of oxygen were injected into the chamber and 50 W applied to the ZnO target. These settings gave a deposition rate of 0.6 Å/s. The thickness to the deposited layer was monitored using a crystal monitor and the deposition was stopped when the layer was 30 nm thick.

The ZnO nanowires were characterised using a Hitachi 4800 SEM for diameter, length and density. The diameter was measured using a top down view and individual nanowires were measured using the built in SEM tool. Multiple nanowires were measured from different areas of the sample. The density was measured by counting the number of nanowires in pre-defined boxes drawn using the SEM tools. Five areas per sample were measured. To measure the length the samples were snapped then tilted to 30° and measured using the in-built software then divided by *cos 30* to find the true length. Again multiple nanowires were measured from several areas of the sample.

5.1.2 Results

Figure 5.1 shows the images collected for each sample. It shows that ZnO nanowires were successfully synthesised over the 2:1 to 1:2 precursor ratios. The nanowires synthesised had hexagonal structures and appeared to be similar in form to those grown by Vayssieres et al. [56].

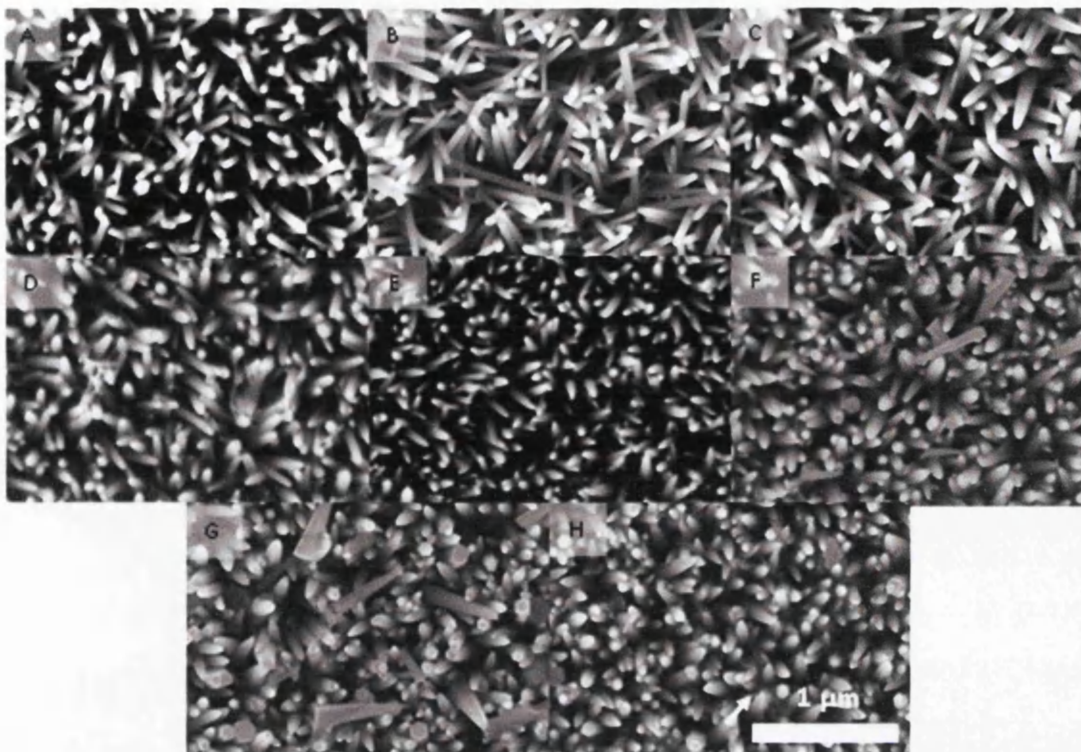

Figure 5.1: SEM images of ZnO nanowires grown aqueously for 6 hours in a 500ml solution containing 1.752g of HMTA and varying amounts of zinc nitrate: A) 1:2, B) 0.57:1, C) 0.8:1, D) 1:1g, E) 1.25:1, F) 1.5:1, G) 1.75:1, H) 2:1, with arrow marking sheets between nanowires [119].

Figure 5.1 shows that using lower concentrations of zinc nitrate relative to HMTA resulted in nanowires that were less tapered than those grown at high zinc nitrate to HMTA ratios. This is caused by an increase ratio of Zn^{2+} to OH^- ions in the solution. The increased Zn^{2+} ions creates a boundary layer adjacent to the Zn terminated face which could increase the dissolution of the nanowire and cause the tapering. This is discussed in full by Sun et al. [58].

Figure 5.1 H shows that at high concentrations of zinc nitrate to HMTA thin sheets, marked with a white arrow, form between the nanowires. The sheets could be formed by nucleation on the sides of the nanowires caused by the excess of Zn^{2+} ions which have encouraged non defined growth on the non-polar facets.

Figure 5.2 below shows a graph of the length and diameter of the nanowires against the ratio of pre-cursors in the growth solution. Measurements were made on the SEM images and each point is an average of at least 20 different nanowires in different area of the samples and the error bars where generated using standard error.

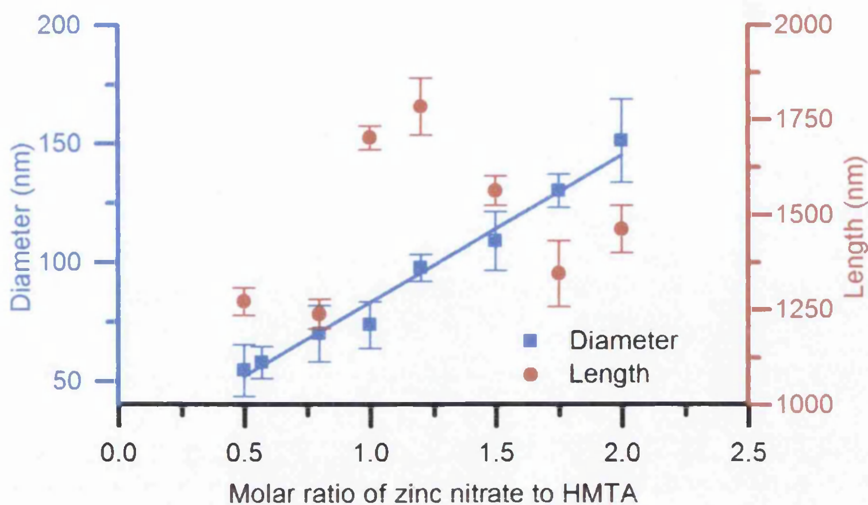

Figure 5.2: Graph of length and diameter of ZnO nanowires against molar ratio of zinc nitrate to HMTA of the growth solution. Error bars show the standard error and a least squared linear fit is applied to the diameter data.

It can be seen in Figure 5.2 that there is no well-defined trend, although there may be a complex trend, between the length of nanowires and the ratio of the pre-cursors in the growth solution. The length of the ZnO nanowires was measured to between 1,240 nm and 1,780 nm across all the samples. The longest nanowires seemed to be produced when the growth solution was around the 1:1 ratio.

The applied least squared linear fit, R^2 (calculated using Pearson's r in Orgin Pro) value 0.980, shows that the diameter increases in a linear fashion with the increase in the molar ratio of zinc nitrate to HMTA. The narrowest nanowires were measured on the sample which was grown in a solution with a concentration ratio for 2:1 in favour of HMTA. The average diameter of this sample was 54 nm. The nanowires grown in the solution with a molar concentration of zinc nitrate twice as high as the molar solution of HMTA had the largest diameter. The average diameter was found to be 151 nm.

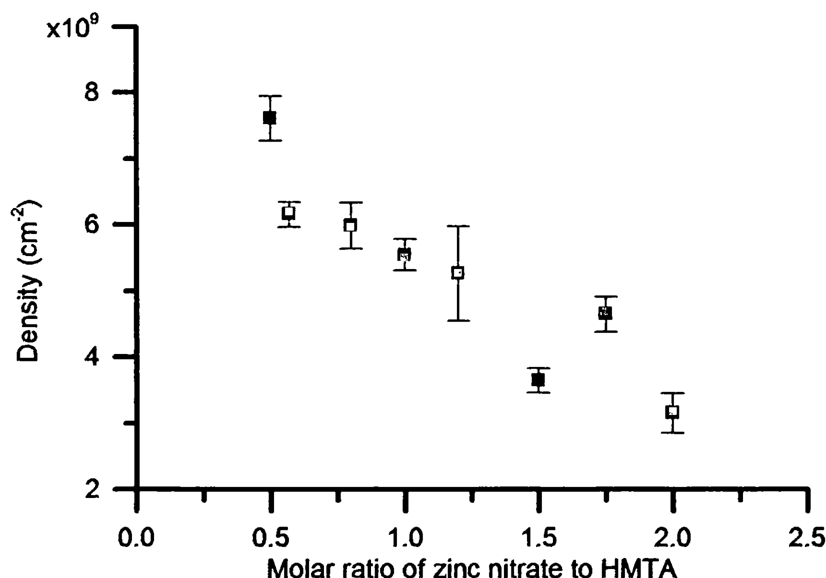

Figure 5.3: Graph of denisty of ZnO nanowires against molar ratio of zinc nitrate to HMTA of the growth solution. Error bars show the standard error.

Figure 5.3 shows the density of ZnO nanowires against the molar ratio of the growth solution. The average density was calculated by counting the number of nanowires in five randomly, selected, separate 1 μm^2 areas across the sample from the SEM images and the error bars were calculated using standard error. The general trend of the graph shows that the average density decreases with increasing concentration of zinc nitrate relative to HMTA. It can be seen that when the molar concentration of zinc nitrate to HMTA was 1:2 the density was 7.62×10^9 nanowires per cm^2 and when the ratio was 2:1 the density was 3.16×10^9 nanowires per cm^2. This change is significant, however, the changes between the others are not, although on average they do show a decreasing trend. The small error bars indicate that nanowire coverage and growth across each sample is consistent.

5.1.3 Conclusion

It has been found that decreasing the molar concentration of HMTA relative to zinc nitrate reduced the diameter of the ZnO nanowires in a linear fashion. This is in agreement with the predictions made by Sugunan et al. [13] although work by McPeck et al. [57] has shown that Sugunan et al.'s mechanism was incorrect by growing ZnO nanowires of varying diameters by varying the concentration of OH^- ions using sources other than HMTA . Using the setup described in the method

section 5.1.1 above it is possible to tailor the diameter of the nanowires synthesised from 54 nm to 151 nm. It was also found that increasing the concentration of zinc nitrate in the growth solution produced nanowires that were tapered. There was also no linear trend between the length of the ZnO nanowires and the molar ratio of the precursors in the growth solution although there could be a more complex relationship. To confirm a more complex trend the experiment should be repeated with a wide range of zinc nitrate to HMTA ratios and smaller changes between each ration. However, longer nanowires were produced when using a 1:1 solution or a solution with slightly higher ratio of zinc nitrate to HMTA. This could suggest that at high concentrations of HMTA, relative to the concentration of zinc nitrate, the rate of reaction is lower producing shorter nanowires. At low concentrations of HMTA, relative to the concentration of zinc nitrate, the growth on the c-plane might be restricted by the increase in the diameter of the nanowires.

5.2 The Effect of Temperature on ZnO Nanowire Growth

5.2.1 Method

To assess the effects of growth temperature ZnO nanowires were synthesised using a method similar to that described in Chapter 5.1.1. For all samples the growth solution contained 1.752 g of HMTA and 2.126 g of zinc nitrate, molar ration 1:0.57, in 500 ml of DI water. This ratio was chosen as it produced non tapered nanowires with most consistent diameter indicate by the error bar in Figure 5.2. The nanowires were grown for 6 hours and each sample was grown in a separate water bath set to different temperatures ranging from 40 °C to 90 °C.

Again the samples were rinsed in DI water and allowed to dry in air. The nanowires were characterised using SEM to measure the diameter and length. Each sample was also characterised using PL to observe the effects of growth temperature on the number of defects present.

5.2.2 Results

Figure 5.4 shows the images collected for each sample. It shows that ZnO nanowires were successfully synthesised at temperatures ranging from 70 °C to 90 °C. The

nanowires found had hexagonal structures and appeared to be similar to those grown in section 5.1 above, however, direct comparison is not possible due to the different growth time.

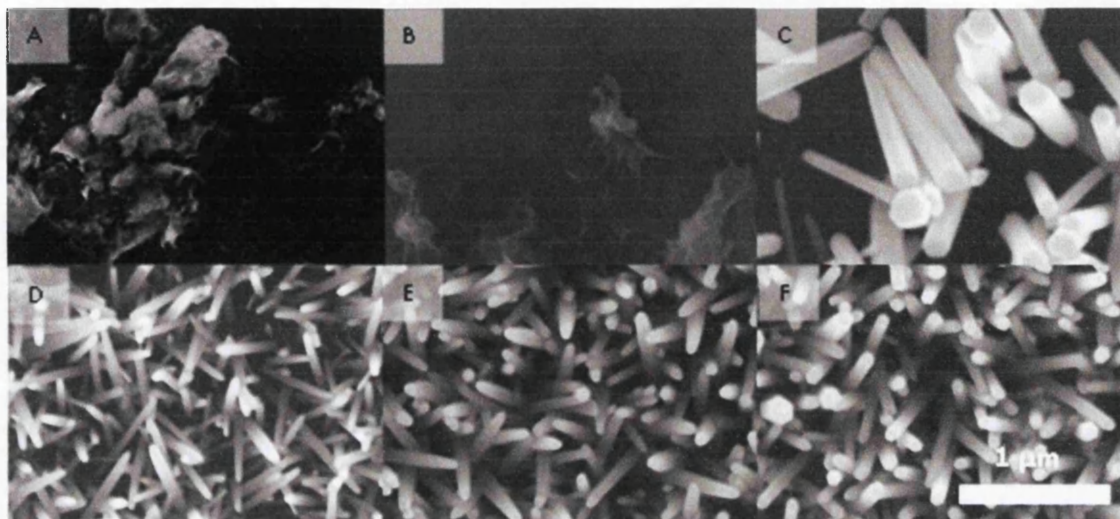

Figure 5.4: SEM images of ZnO nanowires grown aqueously for 7.5 hours in a 500ml solution containing 1.752g of HMTA and 2.126g of zinc nitrate: A) 40 °C, B) 50 °C, C) 60 °C, D) 70 °C, E) 80 °C and F) 90 °C [119].

It can be seen that no ZnO nanowires were synthesised when the growth solution was heated to temperatures lower than 50 °C. It can also be seen that the coverage of nanowires grown at 60 °C was very sparse and the crystals had flat tops. The SEM images show that when the growth temperatures were above 70 °C the nanowires developed a tapered tip and were more dense compared to those grown at a lower temperature.

Figure 5.5 below shows a graph of the length and diameter of the nanowires against the temperature growth solution. Measurements were made on the SEM images and each point is an average of at least 20 different nanowires in different areas of the samples and the error bars were generated using standard error. The trend line was fitted using a linear least squared fit, R^2 (calculated using Pearson's r in Orgin Pro) value 0.979, and extrapolated back.

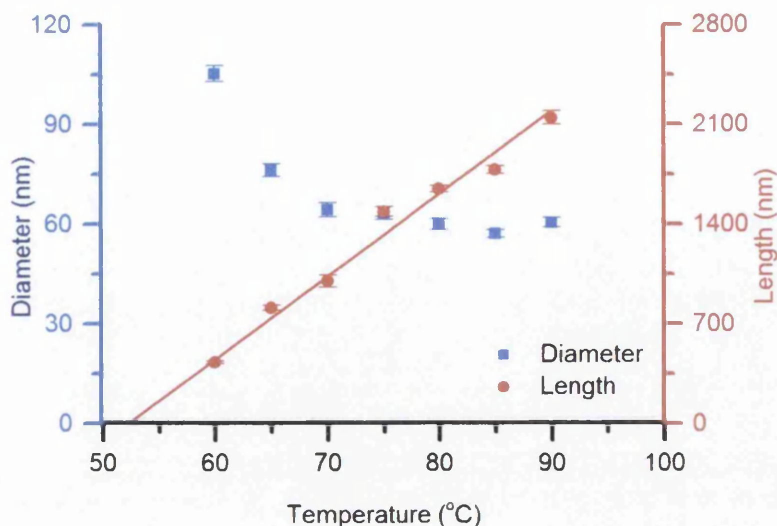

Figure 5.5: Graph of length and diameter of ZnO nanowires against temperature of the growth solution [119]. Error bars show the standard error and a least squared linear fit is applied to the length data.

Figure 5.5 shows that the diameter of the nanowires grown at 60 °C had an average diameter of 105 nm. Increasing the growth temperature reduced the diameter of the nanowires to 76 nm at 65 °C and 64 nm at 70 °C. Increasing the temperature further did not significantly alter the diameter of the crystals. The average diameter of the nanowires grown at temperatures above 70 °C was 61 nm.

The length of the nanowires increased in a linear fashion with growth solution temperature. Extrapolating the graph in Figure 5.5 shows that nanowire growth is only achieved above 51 °C. This agrees with the SEM images in Figure 5.24 and the discussion by Xu et al. [123]. These results and the large diameter of the nanowires grown at 60 °C suggest that this is an effect of the HMTA. HMTA is known to readily hydrolyse in water, therefore the temperature does not affect the production of HCHO and NH_3. The reaction of NH_3 with water to form OH^- is dependant of temperature [57]. This slows the reaction of OH^- with Zn^{2+}. $Zn(OH)_2$ will dehydrate into ZnO in sunlight and since there is no evidence of any growth in Figure 5.4 it can be said that $Zn(OH)_2$ has not formed. Therefore the source of the relationship between temperature and growth rate is the formation of the OH^- ions from the HMTA.

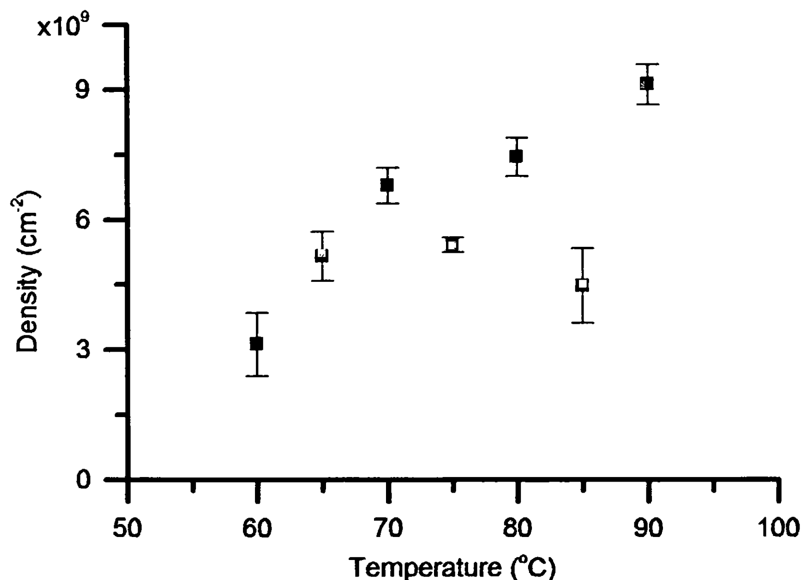

Figure 5.6: Graph of density of ZnO nanowires against temperature of the growth solution. Error bars show the standard error.

Figure 5.6 shows the density of ZnO nanowires against the temperature of the growth solution. The average density was calculated by counting the number of nanowires in five randomly, selected, separate 1 μm^2 areas across the sample from the SEM images and the error bars were calculated using standard error. The general trend of the graph shows that the average density increases with the temperature of the growth solution. The trend could be linear or logarithmic, although the outliers at 75 °C and 85 °C make this difficult to confirm. However, is logarithmic trend it more plausible since density cannot indefinitely increase due to the finite diameter of the nanowires. The outliers could have resulted from seed layer inconsistences due to contamination or uneven deposition. The small error bars indicate that nanowire coverage and growth across each sample is consistent.

PL was also carried out on the nanowire samples. The spectra are shown below in Figure 5.7. Each curve is an average of three separate areas from each sample and normalised to the NBE emission intensity.

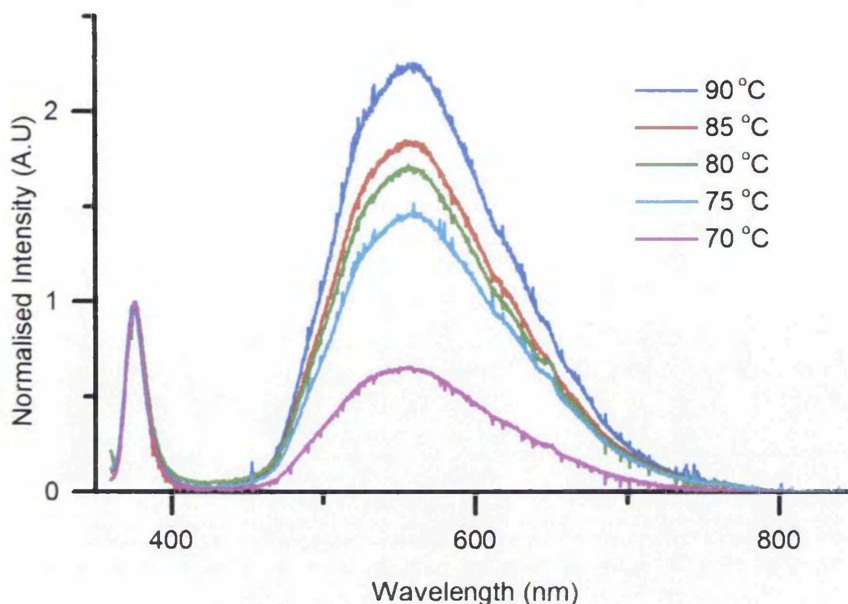

Figure 5.7: PL spectra at room temperature of ZnO nanowires synthesised in growth solutions at different temperatures [119].

Figure 5.7 shows that all samples emitted a NBE at 376 nm which agree with the literature reviewed in Chapter 2. This near band edge equates to an energy of 3.29 eV which is similar to the characteristic band gap of ZnO of 3.3 eV. The PL spectra also shows a broad defect band centred about 557 nm for all samples. It can be seen that the relative intensity of the defect band increases with the temperature of the growth solution. To analyse the defects present FITYK was used to curve fit the defects band and an example of the fit is shown in Figure 5.8.

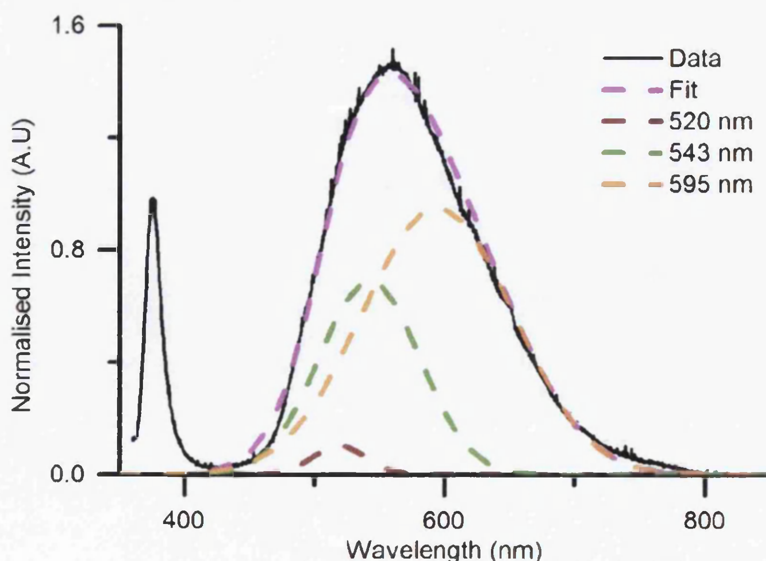

Figure 5.8: Curves fitted PL spectra of ZnO nanowires synthesised at 75 °C.

For each spectra three curves were fitted under the defects band. This is shown in Figure 5.8 where the green line is the obtained data, the red lines are the fitted curve and the yellow line is the overall fit. To obtain the best fit allowed transitions from Table 2.1 where selected and the wavelengths constrained the full width half maxima allow to vary. The peak positions selected were 520 nm, 543 nm and 595 nm. Using Table 2.1 in Chapter 2, these wavelengths are contributed to transitions : from CB to oxygen anti-site, CB to oxygen interstitials with no charge and oxygen vacancies with single or double positive charges to oxygen interstitials respectively. The area under each curve and the total area of the defects band as well the R^2 (calculated using the residual in FITYK) value of the fit are given in Table 5.1.

Table 5.1: Table of curve fitted area for the defect band for each growth tempreature.

	520 nm	543 nm	595 nm	Total	R^2
70°C	3.67	34.91	53.71	92.29	0.997
75 °C	6.39	68.90	130.14	205.43	0.999
80 °C	6.83	90.47	144.44	241.74	0.998
85 °C	9.953	92.55	152.39	254.90	0.998
90 °C	12.31	109.49	187.91	309.71	0.999

It can be seen from Table 5.1 that the main contribution for the defect band is from oxygen vacancies with single or double positive charge. This defect makes up ~60 % for the defects band. It can also be seen that ~36 % of the defects band is attributed to oxygen interstitials with no charge. There is also a small contribution of ~4 % from oxygen atoms occupying zinc sites. To check if the density of defects were affected by the temperature of the growth solution or whether the observed increase in the intensity of the defects band relative to the near band edge is related to the increased surface area due to longer nanowires the curve area was divided by the length. The results are shown in Table 5.2.

Table 5.2: Table of curve fitted area normalised to length for the defect band for each growth temperature.

	520 nm	543 nm	595 nm	Total
70°C	0.004	0.035	0.054	0.09
75 °C	0.004	0.046	0.088	0.14
80 °C	0.004	0.055	0.088	0.14
85 °C	0.006	0.052	0.086	0.14
90 °C	0.006	0.051	0.088	0.14

Table 5.2 reveals that the overall area of the defect band normalised to nanowire length increased when the nanowires were synthesised at 75 °C compared to 70 °C. Growing at higher temperatures did not increase the defect density and therefore the increase in the overall defects observed is caused by the increase in surface area. A similar result would have also been seen if the normalised defect intensity was divided by the density of the nanowires. It was seen that the density also increases in temperature which will also result in an increase in the surface areas of the nanowires.

The area of the curve centred at 520 nm did not increase when the temperature was increased from 70 °C to 75 °C. It can be seen that the increase in overall relative defect density was caused by the oxygen interstitials with no charge and oxygen vacancies with single or double positive charge defects.

5.2.3 Conclusion

It was found, using extrapolation, that ZnO nanowire synthesis did not occur when the growth solution was below 51 °C and that growing below 70 °C produced nanowires that had large diameters and sparsely covered the sample. This is likely to be caused by the slow rate of reaction at lower temperatures between Zn^{2+} and OH^- due to the slow formation of OH^-.

When the growth solution was above 70 °C it was observed that the growth rate increased producing longer nanowires in the same amount of time. It was also observed that the diameter of the nanowires did not change with an increase in temperature above 70 °C.

Analysis of the room temperature PL spectra found that growing at high temperatures increased the intensity of the defects band relative to the near band edge emission. There are three defects that contribute to the defects peak: Oxygen occupying a zinc site (520 nm), oxygen interstitials with no charge (543 nm) and oxygen vacancies with single or double positive charge (595 nm) with the charged oxygen vacancies being the largest component.

It was found that increasing the temperature of the growth solution from 70 °C to 75 °C significantly increased the relative density of the 543 nm and 595 nm defects. However, any further increase in temperature did not increase the defect density and the increase in the defect band was caused by the increased surface area of the nanowires.

5.3 The Effect of Time on ZnO Nanowire Growth

5.3.1 Method

To assess the effects of time on the morphology of synthesised nanowires the growth method preparation was kept the same as that used in Section 5.2 above. Ten 500 ml beakers of growth solution were used containing 2.126 g of zinc nitrate and 1.752 g of HMTA, molar ratio 0.57:1, and heated to 90 °C to maximise growth rate. In each beaker was floated a glass substrate with a 30 nm ZnO seed layer deposited by PVD.

After each 60 mins of growth a sample was removed, rinsed in DI water and allowed to dry in air. The diameter and length were measured using SEM as before. A Fisher Scientific pH probe was calibrated using pH 4 and pH 9 buffer solution and placed in the tenth beaker and the pH of the growth solution was recorded every 5 mins for 540 mins.

5.3.2 Results

Figure 5.9 shows the SEM images collected for each sample. It shows that ZnO nanowires were synthesised after 1 hour of floating on the growth solution although the coverage was very low. After 120 mins of growth the coverage was more

consistent with that seen in Figure 5.1. It can also be seen from Figure 5.9 that after 300 mins of growth the nanowires had large diameters.

Figure 5.9: SEM images of ZnO nanowires grown aqueously in a 500ml solution containing 1.752g of HMTA and 2.126g of zinc nitrate for: A) 60 mins , B) 120 mins , C) 180 mins, D) 240mins, E) 300 mins, F) 360 mins, G) 420 mins and H) 480 mins.

Figure 5.10 shows cross sectional SEM images for each sample and it can be seen that over time the length of the nanowires increase. It can also be seen that the nanowire alignment appears to improve with growth time with the average angle made to the substrate increasing from 42.5 ° for the nanowires synthesised for 60 mins increase to 86 ° for the nanowires synthesised for 480 mins.

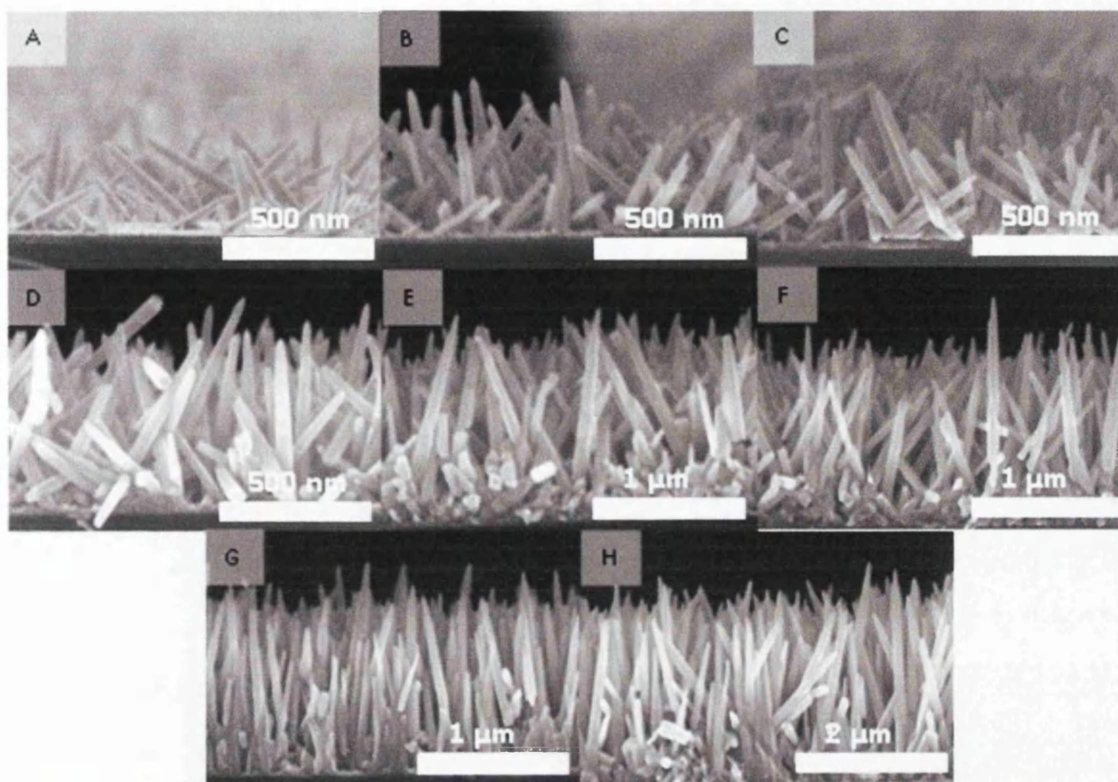

Figure 5.10: Cross sectional SEM images of ZnO nanowires grown aqueously in a 500ml solution containing 1.752g of HMTA and 2.126g of zinc nitrate for: A) 60 mins , B) 120 mins , C) 180 mins, D) 240mins, E) 300 mins, F) 360 mins, G) 420 mins and H) 480 mins.

Figure 5.11 shows a graph of the average length and diameter for the nanowires against time. The average diameter was calculated from the measurement of at least 40 nanowires and the length from at least 15 nanowires and the error bars were calculated using standard error.

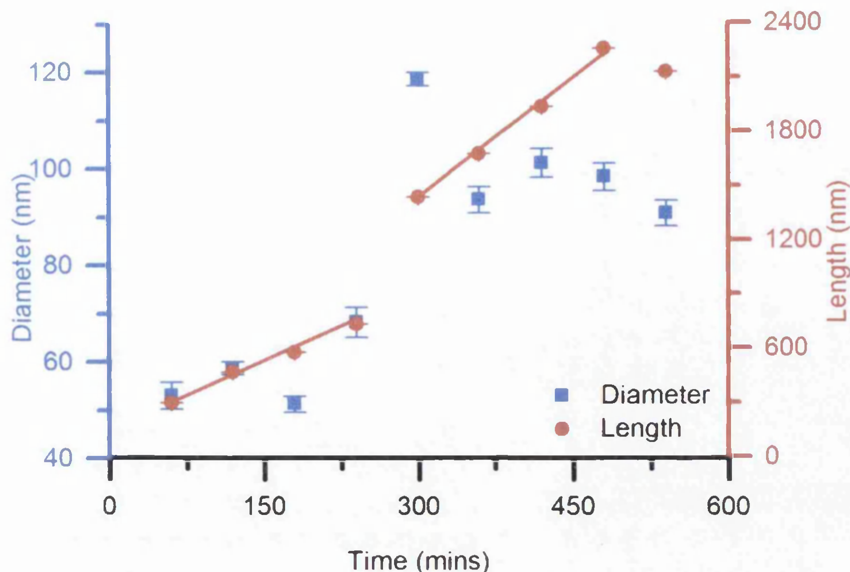

Figure 5.11: Graph of diameter and length of ZnO nanowires against time of the growth. Error bars show the standard error and a least squared linear fits applied to the diameter data.

It can be seen from Figure 5.11 that overall the length of the nanowires increases with growth time. The least squared linear fit, R^2 (calculated using Pearson's r in Orgin Pro) value 0.988, the first 240 mins of growth indicated that length increases in a linear fashion with growth time. The resulting growth rate in the first 240 mins of growth is ~2.5 nm per minute, calculated using the slope of the fit. The nanowires grown for 300 mins were significantly longer than those grown for 4 hours with an average length of 1400 nm compared to 700 nm. The least squared linear fit, R^2 (calculated using Pearson's r in Orgin Pro) value 0.996, shows another linear trend between the length and the time of growth between 300 and 480 mins. This trend shows the rate of growth between these times is greater than between 60 and 240 mins with a rate of ~4.4 nm per minute, calculated using the slope of the fit. After 540 mins there is no increase in the length of the nanowires, the average length was seen to decrease but the decrease is not significant. This is likely to be caused by the solution dropping below the saturation point therefore not allowing further growth.

It can also be seen from Figure 5.11 that the nanowire diameter is dependent on time in the form of a step like function. The average diameter of the nanowires grown for 0-240 mins is ~55 nm. The nanowires grown for 300 mins had a larger average diameter and the nanowires grown from 480-540 mins had an average diameter of

~90 nm. The data point for diameter of the nanowires grown for 300 mins seem to be an anomaly which may have been caused by an error in making the solution such as adding too little HMTA. This experiment was repeated and showed a similar trend in the results with a large increase in growth around the 300 mins mark. However, this experiment was carried out in a different lab resulting in different atmospheric conditions, and this appears to affect the size of the final nanowires. The graph of the repeat experiment is shown below in Figure 5.12.

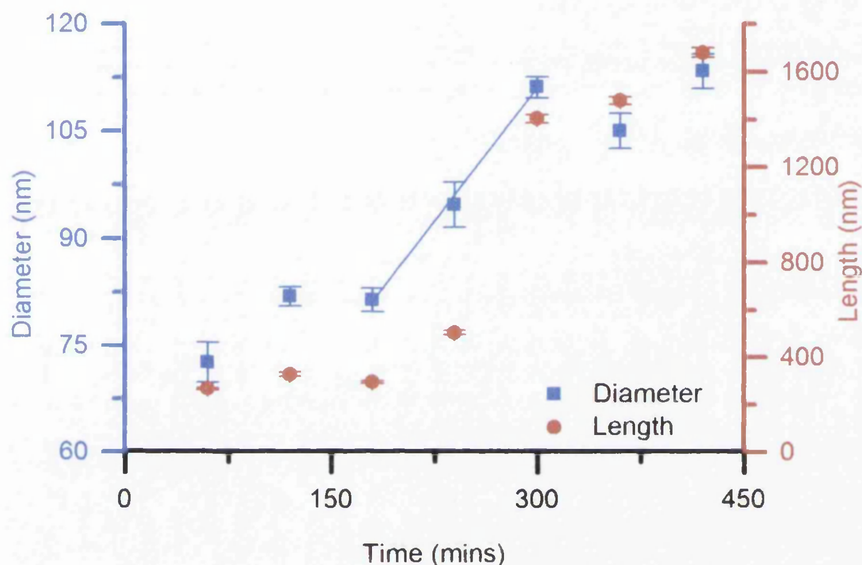

Figure 5.12: Graph of diameter and length of ZnO nanowires against time of the growth for repeat experiment. Error bars show the standard error and a least squared linear fit applied to the length data.

The repeat also shows a jump in the length growth rate at 300 mins. The repeat also shows that during the same period that diameter increase is not jump but the least squared increase fit, R^2 (calculated using Pearson's r in Orgin Pro) value 0.998, suggests that the increase is linear. To try and test for changes in the solution, the pH was measured every 5 minutes over the 540 mins of growth and the result is shown below in Figure 5.13.

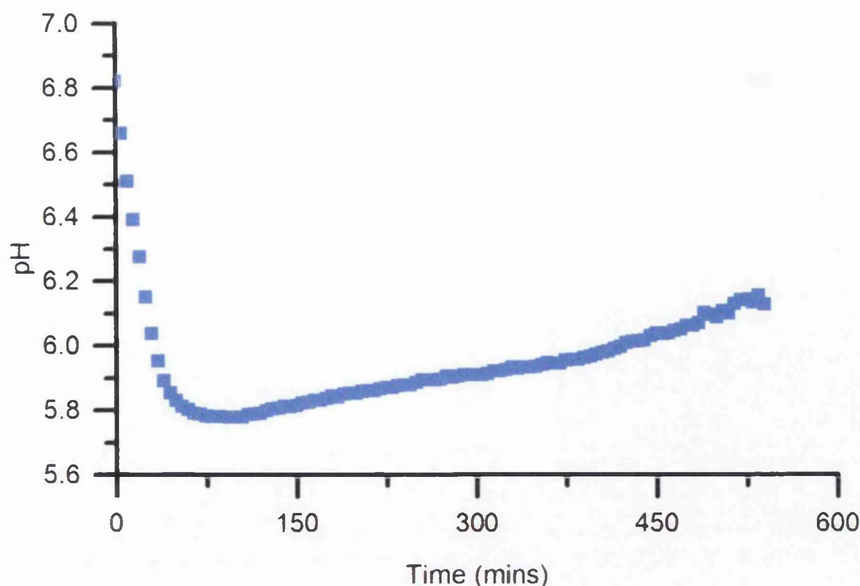

Figure 5.13: Graph of growth solution pH against time of the growth.

Figure 5.13 shows that the initial pH of the solution is 6.8 and over the 60 mins of growth the solution becomes more acidic and the pH decreases to 5.8 due to the precipitation of the zinc ions [58]. The pH then increases to 6.16 over the next 480 mins of growth and the pH starts to oscillate over the last hour of growth. This result is different to that found by Jacob et al. who found the pH was ~10 [39]. However, the result in Figure 5.13 is similar to that found by McPeak et al. who found that the saturation index of ZnO is 5.7 [57]. The pH increases over time as the HTMA decomposes into OH^- ions which causes the solution to tend toward neutral. After 480 mins of growth the pH starts to oscillate suggesting that OH^- production is slowing which results in the slowing of growth. The graph does not suggest any sudden change between 240-300 mins that causes the sudden increase in growth seen in Figure 5.11 and Figure 5.12. This suggests that the sudden increase in growth is not caused by the breakdown of HMTA or zinc nitrate but may be caused by the conversion to ZnO from $Zn(OH)_2$. Initial Zn^{2+} ions combine with OH^- ions to form $Zn(OH)_2$ which can undergo forward reactions to ZnO or a backwards reactions to $Zn2^+$ ions. It is possible that at the 300 mins that these reaction reach an equilibrium or break an equilibrium that results in a the rapid growth. The relatively high pH in the first hour does explain the lack of growth seen in the SEM images in Figure 5.8 as the zinc nitrate has not broken down as also seen by Sun et al. [58].

5.3.3 Conclusion

It has been seen that in general the length of ZnO nanowires increase with time of growth up until 480 mins. After 480 min the solution drops out of saturation due to lack of either Zn^{2+} and OH^- ions and the growth stops in the same manner suggested by Sun et al. [58]. For the first hour of synthesis the growth is slow and sparse due to the relatively high pH. Between 60 and 240 mins of ZnO nanowire synthesis the growth rate is linear. Between 240 and 300 mins the nanowires undergo rapid growth but this could not be explained from the experiments carried out. The growth between 300 and 480 mins is again linear but at a faster rate than the first 240 mins.

It was also seen that the diameter of the ZnO nanowires follows a step like function with time with a linear increase between 180 and 300 mins. As with the nanowire length the diameter undergoes a rapid increase between 240-300 mins. For the first 240 mins the nanowires are narrow, around 55 nm in diameter, and longer growth time results in nanowires around 90 nm in diameter.

5.4 The Effect of Substrate on ZnO Nanowire Growth

5.4.1 Method

To assess the effects of substrate type on ZnO nanowire growth, as seen by Brown et al. [14], an intrinsic silicon wafer was cut into forty 1 cm^2 pieces and cleaned by sonication in acetone and isopropanol. PVD was used to coat: ten pieces with 200 nm of chromium, ten pieces with 200 nm of tungsten and ten pieces with 200 nm of titanium. These metals where chosen as they are often used as contacts and bonding layers in nanowire device fabrication. PVD was then used to deposit a 30 nm ZnO layer on all forty samples and the roughness of the ZnO seed layer was characterised using a JPK AFM.

All samples were grown in 500 ml of solution containing 2.126 of zinc nitrate and 1.752 of HMTA, molar ration0.57:1. Four of each sample were floated in four PTFE beakers containing growth solution heated in a water bath at 90 °C for 9 hrs. One of each sample was floated in a fifth beaker of growth solution and grown at 90 °C for 9 hrs. Four of each sample was also placed in four glass beakers containing 500 ml of

growth solution and heated in a 800 W microwave oven for 30 mins. One of each sample was also placed in a fifth glass beaker and heated in the microwave oven for 30 mins.

All samples were rinsed in DI water, dabbed dry and then allowed to dry fully in air. All the samples were then characterised using SEM to measure diameter, density and length.

5.4.2 Results

As above the nanowires synthesised were characterised using SEM to measure the diameter, density and length for all samples. The bar graph of average diameter against substrate for all four growth situations is shown below in Figure 5.14 and the error bars are generated standard error.

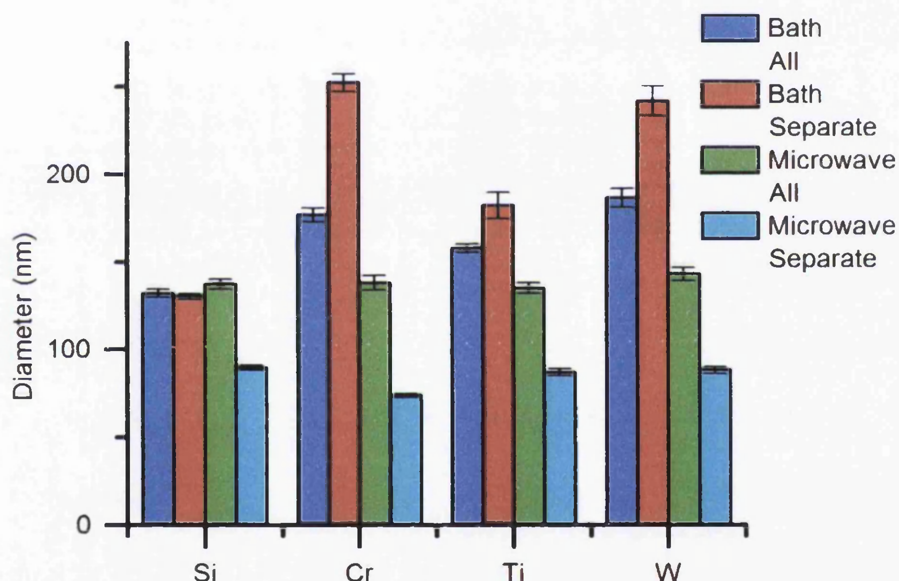

Figure 5.14: Graph of diameter against PVD substrate material. Error bars show the standard error.

It can be seen from Figure 5.14 that in general the ZnO nanowires synthesised in the microwave oven had small diameters compared with the nanowires grown in a common beaker which produced the narrowest nanowires. In contrast the nanowires produced in the water bath in beakers containing one type of substrate, in general, had the largest average diameter compared the samples grown in a common beaker,

this agrees with Brown et al. [14]. This suggests that at least one of the metal layers used has reacted with the solution resulting in a lower growth rate.

From the graph it can be seen that the substrate does not significantly affect the diameter of the nanowires when they were grown in a common beaker in the microwave. While of the Cr sample differed significantly when grown separately When grown in a common beaker the average diameter was ~138 nm for all substrate types. When the nanowires were grown in separate beakers they had diameters of ~86 nm for the Si, Ti and W while the nanowires grown on Cr had a diameter of ~74 nm.

The diameter of the nanowires synthesised in the water bath were dependent on the substrate material. It can be seen that the nanowires grown on ZnO seed layers on silicon had the smallest diameter, ~ 131 nm for both separated and all in one samples. Growth on a layer of Ti under the seed layer produced larger diameter nanowires than the Si samples both on the grown separately and common beaker samples, 182 nm and 158 nm respectively. The samples with a W and Cr metal layer had the largest diameters and did not differ significantly from each other shown by the error bars over lapping. The Cr sample had the largest average diameters 252 nm when grown separately and 177 nm when grown in the same beaker as the other samples. The density of the nanowire coverage was also measured and the results shown in Figure 5.15.

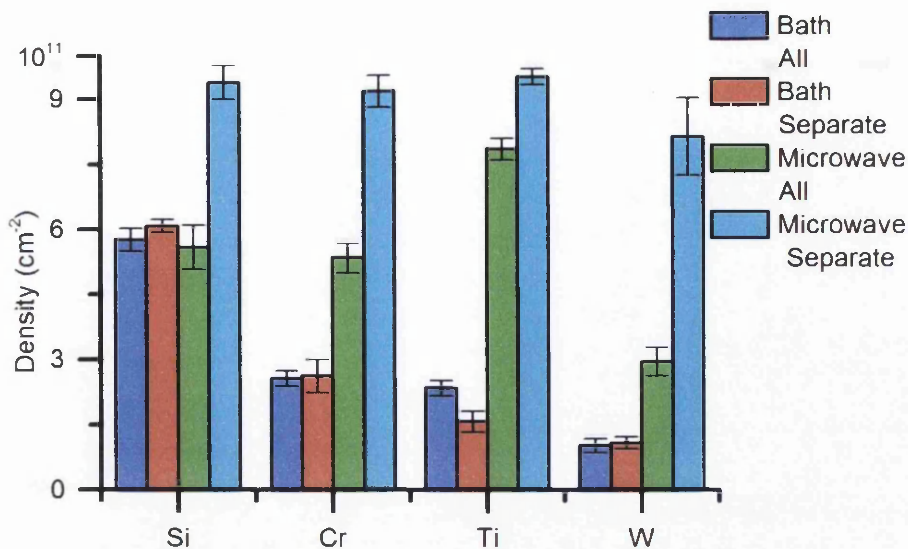

Figure 5.15: Graph of density against PVD substrate material. Error bars show the standard error.

Figure 5.15 shows that in general the density of the microwave synthesised nanowires was higher than those grown in the bath and the samples grown separately in the microwave had denser coverage than those grown in a common beaker. This was expected due to the smaller diameter of the microwave nanowires allowing more space for the nanowires to grow. The density of the nanowires grown separately in the microwave does not in general change with substrate material with the nanowires grown on Si, Cr and Ti having a diameter of ~9.3×10^{11} NW/cm^2 and the nanowires grown on W having a diameter of ~8.1×10^{11} NW/cm^2. For the samples grown in the same beaker in the microwave the sample with the Ti layer had the largest density while the sample with a tungsten layer had the lowest density. The samples without a metal layer and with the Cr layer did not have significantly differing densities with the standard error bars overlapping.

For the bath grown nanowires, the density in general does not significantly depend on whether the samples were grown in the common beaker or separately. It also does not appear that the density of bath grown nanowires is related to diameter. Figure 5.16 shows density of the nanowires against the diameter for the bath grown nanowires and shows there is no correlation between the two.

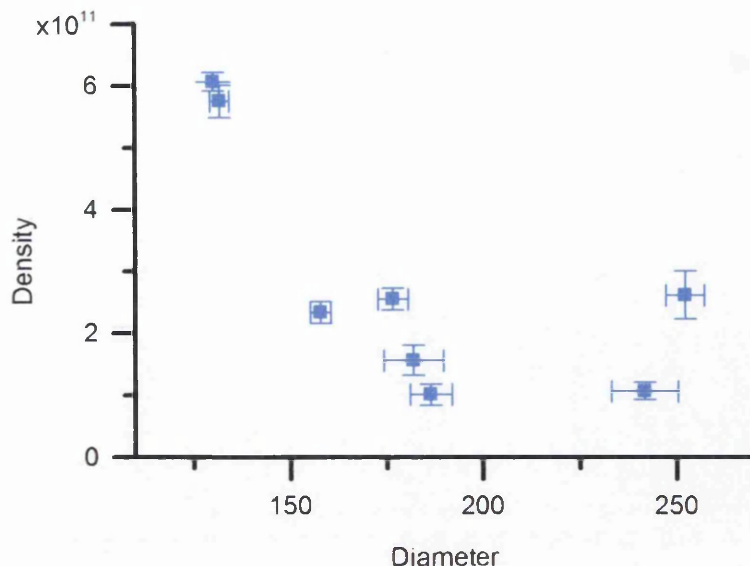

Figure 5.15: Graph of density against diamter of nanowire. Error bars show the standard error

The sample without a metal seed layer had the largest density, the Cr and Ti samples had roughly the same densities and the samples with the W layer had the least density.

The length of the nanowires was also measured using the SEM images. The results are shown the graph in Figure 5.17 below and the error bars are again generated using standard error.

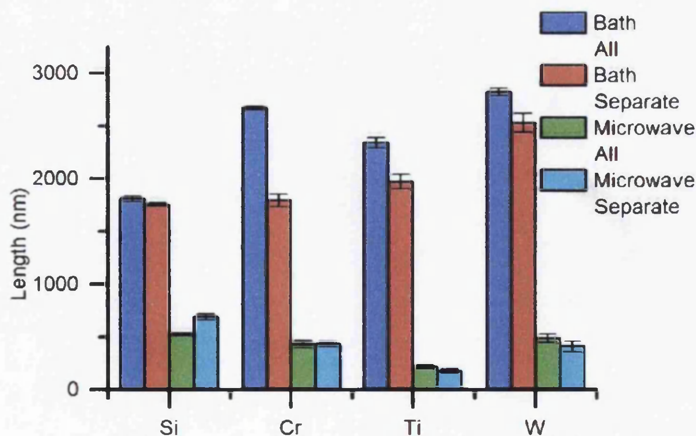

Figure 5.17: Graph of length against PVD substrate material. Error bars show the standard error.

Figure 5.17 shows that nanowires synthesised in the microwave were shorter than those grown in the water bath. In general there was little difference between the lengths of the nanowires grown in the microwave when the samples were separated or mixed in the beaker of growth solution. The samples with a Ti layer under the ZnO seed layer produced the shortest nanowires with an average length ~200 nm. The average lengths of the nanowires grown on the CR and W samples were ~410 nm while the plain silicon were 520 nm for those grown with the other samples and 689 nm for those grown separately.

For the samples grown in the water bath the nanowires grown in separate baths were shorter than those grown in a common beaker. This is opposite to the findings of Brown et al., however, they state that the nickel layer they used might inhibit the growth rate of all the samples in the common beaker [14]. Nickle was not used as this experiment was looking at nanowires grown substrates at are commonly used for fabricating nanowires array devices. The nanowires grown on Si were the shortest with average lengths of 1.80 μm and 1.75 μm. The nanowires grown on W layers were the longest with average lengths of 2.82 μm and 2.52 μm. When grown with all types of substrate the nanowires grown on Ti had an average length of 2.33 μm and the nanowires grown on the sample Cr had an average length of 2.67 μm. When grown in separate baths the nanowires grown on Ti had an average length of 1.97 μm and the nanowires grown on the sample Cr had an average length of 1.79 μm.

To understand the difference that causes the different growth caused by the metal layer on the substrate, AFM was used to measure the average roughness on the ZnO seed layers. The results are shown below in Figure 5.18. The error bars were generated using standard deviation.

SWANSEA UNIVERSITY LIBRARY

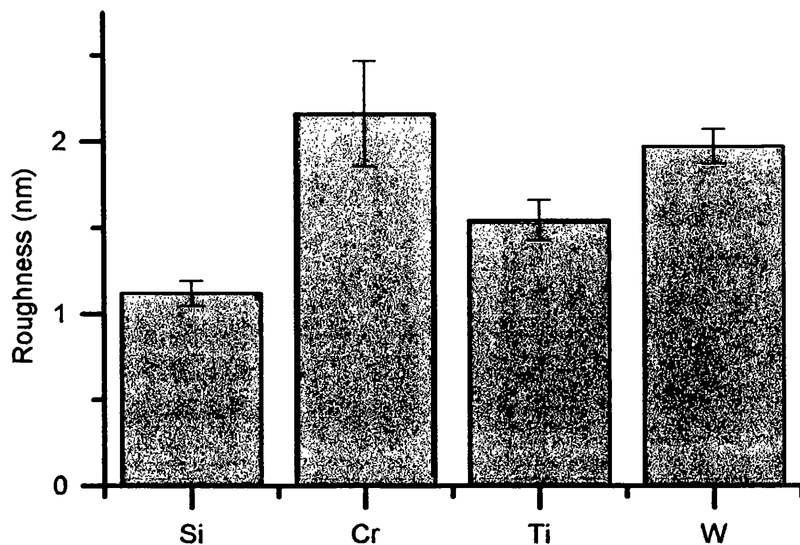

Figure 5.18: Average roughness against substrate material. Error bars show the standard error.

Figure 5.18 shows that the ZnO seed layer on Si was the least rough while Cr was the roughest. However, there is no statistical significance between the Cr and W samples. Therefore there is correlation between the diameter of the nanowire and the roughness of the seed layer shown in Figure 5.18. The least square dl linear fit, R^2 value for the samples grown in a common beaker is 0.891 and R^2 value for the samples grown in separate beakers is 0.996, indicated that the relationship is linear. From the graph sample grown in a common beaker have a lower average diameter than those grown in separate beakers with the slope increasing from 48.4 to 119.6.

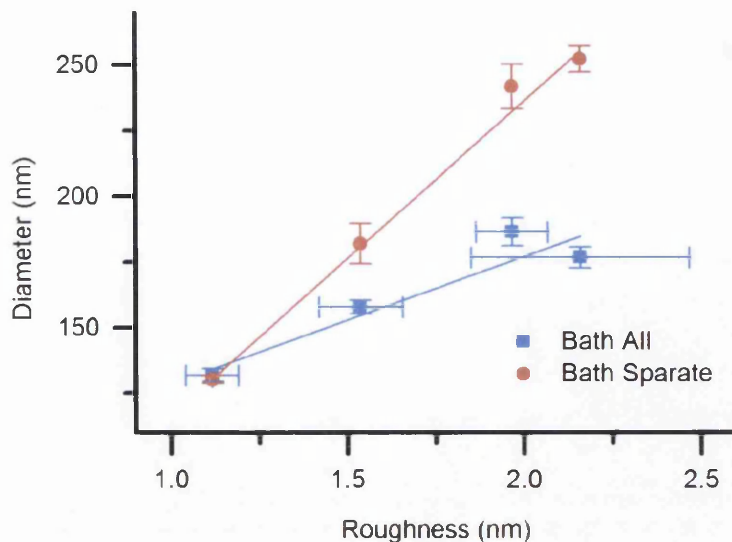

Figure 5.18: Graph of diameter of nanowire against roughness of seed layer for the bath grown samples. Error bars show the standard error and least square linear fits applied to both sets of data.

The roughest seed layer causes growth of the widest nanowires. There is also a correlation between the length of the nanowires grown in a common beaker and the roughness, shown in Figure 5.19. The least squared linear fit, R^2 (calculated using Pearson's r in Orgin Pro) value 0.867 shows that the relationship between roughness and length in linear.

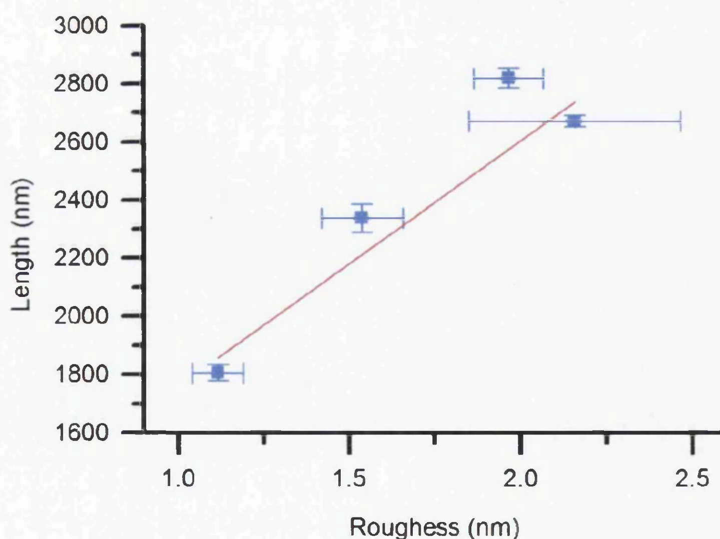

Figure 5.19: Graph of length of nanowire in the bath common beaker against roughness of seed layer for the bath grown samples. Error bars show the standard error and a least square linear fit applied.

This disagrees with Brown et al. who found the opposite, they did find that a ZnO seed layer on bare silicon was the least rough [14]. Brown et al. did find that grain size also affected the morphology of the nanowires. They did state that small grain size caused longer wider nanowires. The grain size was not measured here since AFM sizing was considered un-reliable and SEM was unable to obtain high enough resolution on intrinsic silicon. However, it is reasonable to assume that rougher seed layers had small grain sizes as observe by Tarat et al on their nanosheets [87]. therefore the result could be in agreement with Brown et al [14].

The small grain size causes increased solubility according to the Ostwald-Freundlich equation 5.1:

$$c(r) = c_0 e^{\frac{y\Omega}{rkT}} \qquad (5.1)$$

where $c(r)$ is the solubility, c_0 the bulk solubility, r is the crystal size, y is the surface free energy, Ω the molecular volume, k the Boltzmann constant and T the absolute temperature. From equation 5.1 is can be seen that smaller grain size results in great solubility causing the small grains to dissolve more readily and therefore deposits larger particles giving rise to longer and wider nanowires. It is also possible that the increase in length and diameter of the nanowires grown on the rougher seed layers is caused by the higher surface area and therefore giving higher initial growth rate.

Another possibility for the different morphology of ZnO nanowires when grown on different substrate could be a chemical reaction between the metal and the ZnO seed layer. This has not been investigate in this thesis, however, Kim et al, [124] noted that Ti reacts with ZnO to form TiO by drawing oxygen from the ZnO lattice. This chemical reaction could affect the surface chemistry of the seed layer resulting in the observed changes in growth. Experiments have been carried out by Evans [125] characterised a 20 nm layer of ZnO deposited on Ti with PL but found no change in the spectra when compared to ZnO deposited on Si. This suggests that the reaction between the ZnO and Ti does not extend up through the 20 nm of the seed layer and therefore does not affect the surface chemistry.

There seems to be no trends among the microwave samples. It is possible that the microwaves cause changes in the metal layers that affect growth, however, no tests have been undertaken to show this.

5.4.3 Conclusion

It has been seen that microwave synthesis for ZnO nanowires produces shorter nanowires usually with small diameters than bath synthesised nanowires. However, the density of nanowires is higher than bath grown nanowires.

It has also been seen that depositing a metal layer before the ZnO seed layer results in a change in morphology of the ZnO nanowires when grown in a water bath; there is little change when grown in a microwave. It appears that the metal layer causes the seed layer to change in roughness depending on the metal. It was found that Cr and W caused the roughest ZnO seed layer which resulted in the longest and widest nanowires. Brown et al. suggests that the increased surface area causes a faster initial growth rate caused by small grain sizes which reduced the solubility resulting in a faster growth rate [14].

Chapter 6: Characterisation of ZnO nanostructures

This chapter reports on a series of experiments that relate to the cleaning of ZnO with the aim of achieving local transport measurements. This chapter also reports on an experiment in which ZnO nanosheets were annealed in vacuum and characterised after each treatment using SEM, PL, AES and 2 point probe which has been published in Nanoscale Research Letters [126].

The chapter first describes an attempt to clean ZnO single crystal using the recipe that was published by Dulub et al [15] and descripbed in Chapter 2. The result was characterised using LEED. The chapter then reports on two experiments that examine the effects of the cleaning treatment: argon bombardment; which has been published in Nanotechnology [127], and vacuum annealing. These experiments also give insight into the defects present in aqueous synthesised ZnO nanowires and where in the structure they are situated. These two experiments also provide a way to control the defects present so that they can be altered to suit devices.

Using the results for the annealing and argon bombardment treatment the recipe for cleaning the single crystal was changed and this chapter reports on the attempt to obtain atomic resolution on single crystal ZnO using it. The recipe was then applied to ZnO nanowires and STM was carried out.

6.1 Argon Bombardment and Heating Single Crystal ZnO

6.1.1 Method

Single crystal ZnO was purchased from PiKem Ltd with orientation $(10\bar{1}0)$ and cut to 10 mm by 3 mm and polished on one side. The crystal appeared green when visually inspected.

The single crystal was placed on an Omicron two tiered sample plate and loaded into an Omicron VT STM/AFM. The sample was moved into the preparation chamber containing a PSP ISIS3000 argon gun and LEED stage. A LEED diffraction pattern was taken then cleaned using argon bombardment and heating following the recipe used by Dulub et al. [15]. The single crystal was cleaned using cycles of argon bombardment of 1 keV for 15 minutes, then heated to 900 °C using the stage heater. The heating curve used for the heating was taken from the Omicron manual and showed that 60 W of power is needed for the stage to reach 900 °C. After each cleaning cycle the LEED pattern was captured.

6.1.2 Results

Figure 6.1, below, shows images of the LEED pattern taken after argon bombardment of 1 keV. The images were taken using a Canon D55 digital camera under a blackout curtain with a 2 second delay to ensure it was stable with a low ISO and 4 s exposure.

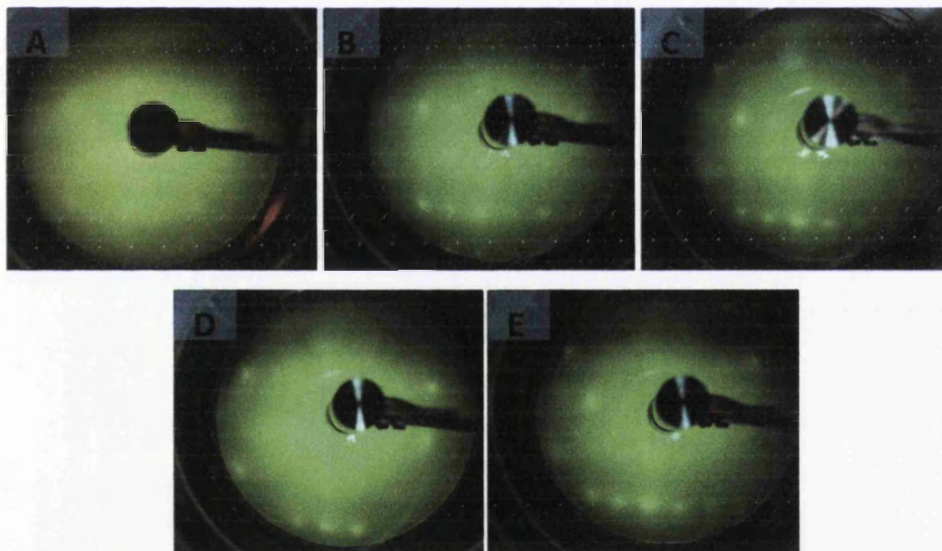

Figure 6.1: LEED of single crystal ZnO ($10\bar{1}0$) taken at 151.1 eV A) before treatment, B) after 1 cycle of 1 keV Ar bombardment for 15 mins and 1 hour of heating at 900 °C, C) after 2 cycles of 1 keV Ar bombardment for 15 mins and 1 hour of heating at 900 °C, D) after 3 cycles of 1 keV Ar bombardment for 15 mins and 1 hour of heating at 900 °C and E) after 4 cycles of 1 keV Ar bombardment for 15 mins and 1 hour of heating at 900 °C.

Figure 6.1 shows that before treatment no LEED pattern was obtained suggesting that the surface of the single crystal ZnO was not well ordered. After one cycle of argon bombardment and heating a 2x1 LEED pattern was observed. However, the

pattern is not clear showing 7 out of the expect 20 spots across the left half of the hemisphere compared to the LEED partner in Figure 6.19c where the cleaning recipe has been optimised which shows 18 out of 20 spots across the left half of the hemisphere. After two cycles of treatment, the LEED pattern is clearer, showing 10 out of 20 spots, than that obtained after one cycle. Figure 6.1 shows that further cycles of argon bombardment and heating do not improve the obtained LEED pattern.

6.1.3 Conclusion

It has been seen that following Dulub et al.'s [15] recipe did not produce a clear LEED pattern with only 7 out of 20 dots seen. There are two possible causes for this. This first is the argon bombardment power is too high which would result in too much damage to the single crystal or too low so that the crystal does not clean. The second is that temperature is either too high to too low. It also need to be considered that nanostructures require different cleaning conditions to single crystal. To understand the effects of the argon bombardment and heat the follow two experiments have been carried out. The first examines the effects of argon bombardment on nanowires and the second examines the effects of heating. The results are then used to modify the cleaning recipe.

6.2 The Effects of Argon Bombardment on ZnO Nanowires

6.2.1 Method

To assess the damage of the Ar bombardment, nanowires were mechanically transferred onto two Si/SiO_2 wafers (referred to as Sample 1 and Sample 2) using a method used by Lord et al. [3] where the Si/SiO_2 wafers were rubbed across the top of the as grown nanowire array. Sample 1 was scanned using SEM and PL then subjected to increasing doses of argon bombardment using sample current as a measure. The powers used were 0.3 keV, 0.5 keV, 1.0 keV, 1.5 keV and 2.0 keV which equated to a sample current of 2 μA, 12 μA, 19 μA, 23 μA and 26 μA. After each treatment the Sample 1 was scanned using SEM and PL again.

2 point probe I-V measurements using an Omicron LT Nanoprobe were taken on the Sample 2. The sample was placed on an Omicron directed current heating plate designed for the Nanoprobe. The sample was then subjected to the same argon treatment as Sample 1 using the sample current as a measure of dose. After each treatment I-V measurements were taken.

The tips were direct current annealed to remove tip oxide as described in Chapter 3 [108] and approached onto the nanowire using a method put forward by Smith et al. [128], to ensure minimal compressive strain at the point of contact providing intrinsic characterisation. An SEM image of the tips in contact with the nanowire is shown in Figure 6.2 below.

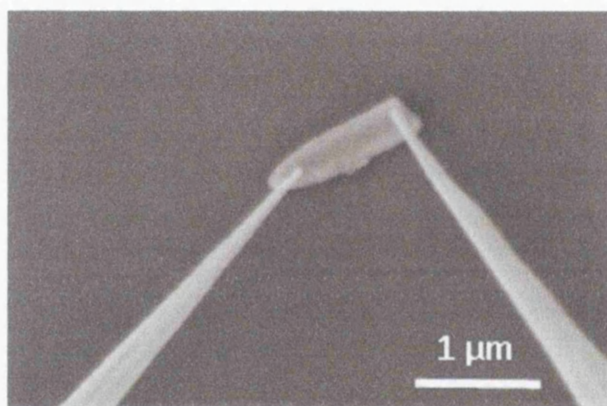

Figure 6.2: SEM image of two tungsten probes approached onto a ZnO nanowire for 2 point probe measurements.

For the PL, three spectra were taken from different areas of Sample 1 and averaged after each treatment. For the I-V measurement four randomly selected nanowires were measured after each treatment. For each nanowire the tips were approached manually until contact was seen to be made.

The nanowires used were grown on a substrate made from a 25 x 25 mm glass microscope cover slip on which a 30 nm ZnO seed layer had been deposited using PVD. The nanowires were synthesised for 9 hours using a water bath heated to 90 °C using a solution of 500 ml of DI water, 2.126 g of zinc nitrate and 1.752 g of HMTA. These conditions were used since the experiments in Chapter 5 found that they produced long nanowires of around 2.5 μm with a diameter greater than that of the tungsten probe with minimal tapering with high density.

6.2.2 Results

Two point probe on the nanowires before argon bombardment revealed that the average resistance per unit length over probe separation at 1 V was $2.6 \times 10^{13}\ \Omega m^{-1}$ and at -1 V was $2.0 \times 10^{13}\ \Omega m^{-1}$. This is shown in Figure 6.3. The error bars were calculated using standard deviation and reveal that before argon treatment the normalised resistance has a large spread. This indicates that the contact between the probes and the nanowires is inconsistent.

After argon bombardment of 2μA for 15 minutes the normalised resistance decreases to $2.7 \times 10^{10}\ \Omega m^{-1}$ at both 1 V and -1 V. It can also be seen that the standard deviation has also decreased. This shows that the argon bombardment has removed surface contamination from the nanowires and allowed for better and more consistent contacts to be made with the probe tips. Further argon bombardment with higher sample current increases the average normalised.

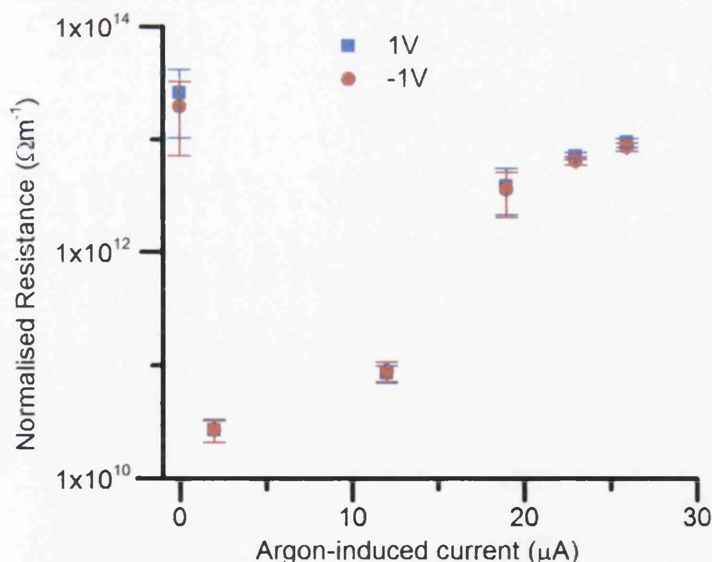

Figure 6.3: Graph of normalised resistance against the sample current from argon bombardment. Error bars generated using standard deviation.

The averaged I-V sweeps normalised to probe separation are presented in Figure 6.4. Analysis of the I-V sweeps after each argon treatment showed that initially the

contact behaviour was ohmic and became more ohmic after 2 μA of treatment. Further argon bombardment caused the I-V curve to become Schottky in behaviour.

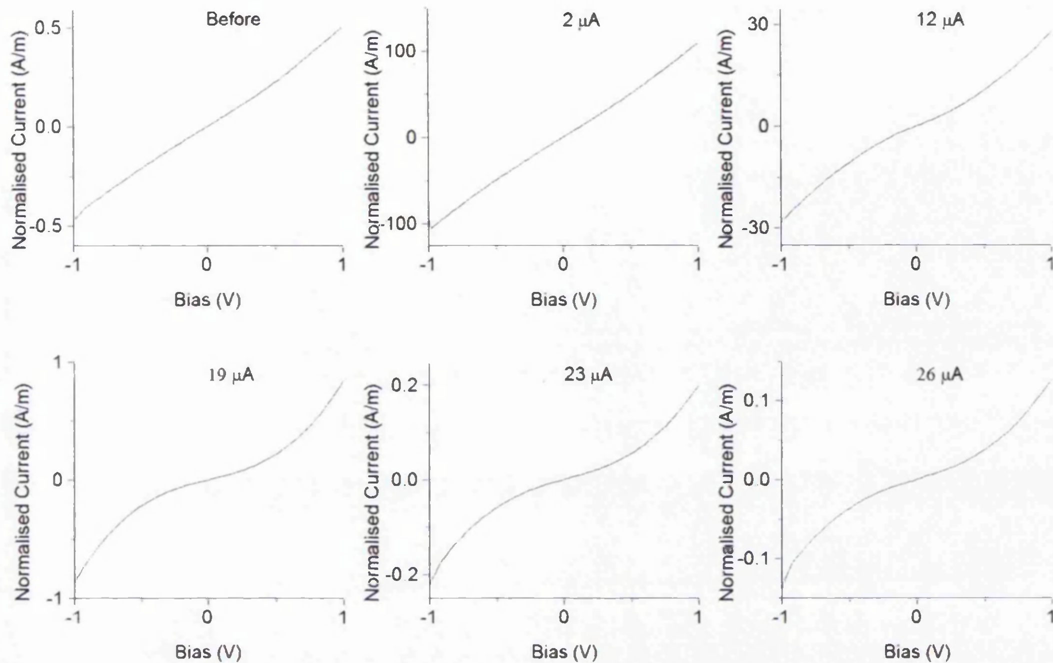

Figure 6.4: I-V sweep normalised to probe separation against bias for each argon treatment.

To characterise this, a linear fit was applied to the average I-V curves and the R^2 (calculated using Pearson's r in Orgin Pro) value from these fits plotted against argon current to measurement the deviation from Ohmic. The R^2 against argon-induced current is shown in Figure 6.5.

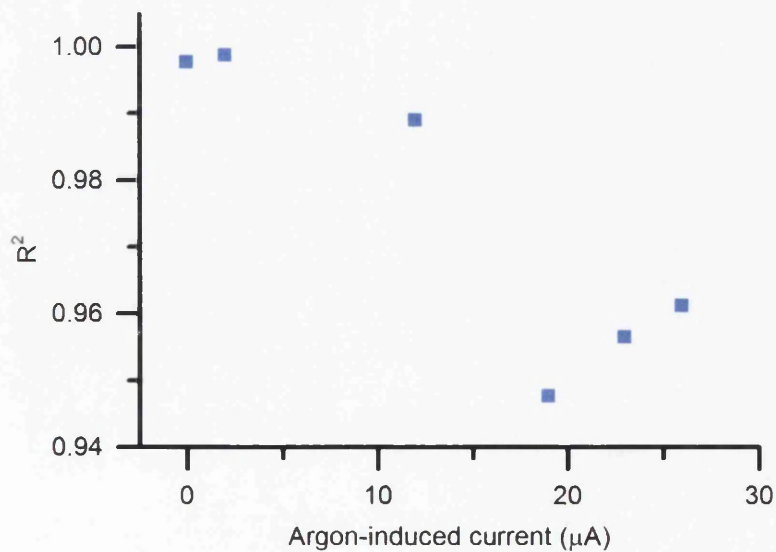

Figure 6.5: Graph R square value of linear fit against the sample current from argon bombardment.

PL revealed that the near band edge was centred at 376 nm and a defects band peak centred at 595 nm neither of which changed after argon bombardment, as seen in Figure 6.6. Argon bombardment using a sample current 2 μA for 15 mins did not significantly change the normalised intensity of the defects band. This supports the argument that low dosed argon treatment cleans the surface resulting in better contact between the nanowire and the probes rather than being a lattice effect. Further argon bombardment with an increased dose resulted in a decrease in the intensity of the defects band relative to the near band edge. This has been plotted in the inset Figure 6.6 as green triangles and shows that the decrease is linear, R^2 (calculated using Pearson's r in Orgin Pro) value 0.987.

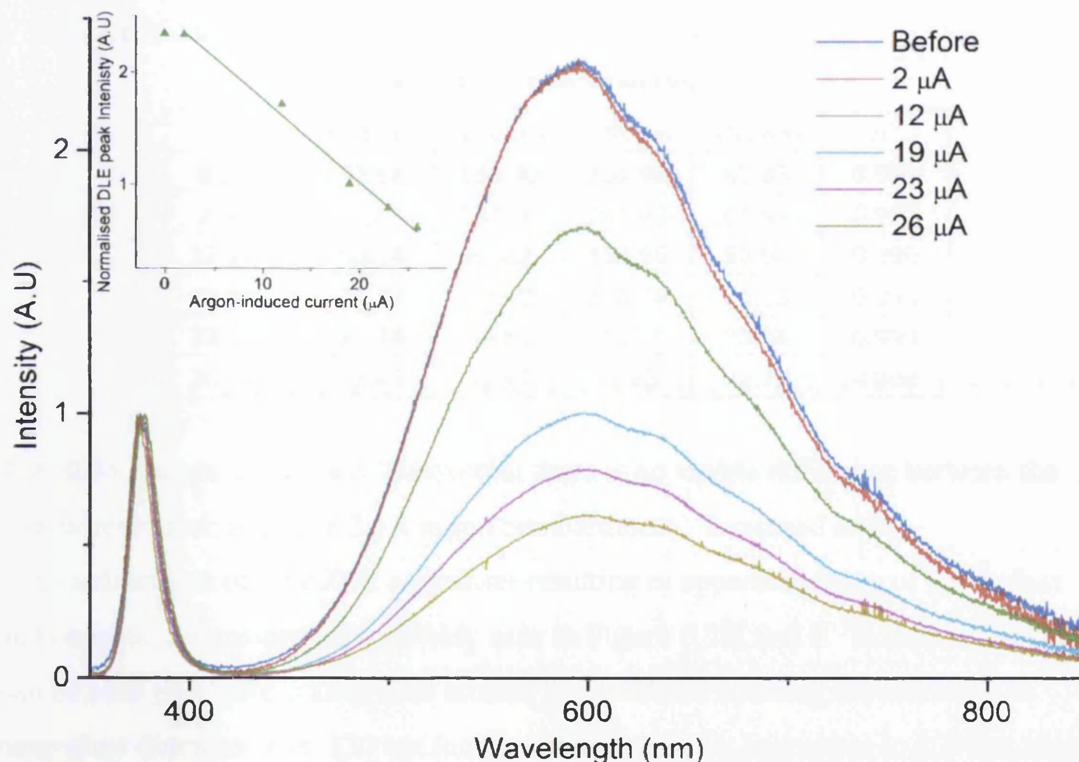

Figure 6.6: PL spectra for ZnO nanowires with different doses of argon bombardment. Inset: DLE peak intensity normalised to NBE peak against the sample current from argon bombardment. Linear fit least squared fit applied to DLE peak intensity normalised to NBE peak data.

Curve fitting under the DLE peak shown in Figure 6.6 showed that there are 5 components centred at 543 nm, 595 nm, 640nm, and 765 nm. These defects are attributed to transitions from: CB to oxygen interstitials with no charge, oxygen vacancy with a positive charge to oxygen interstitials, oxygen vacancy with a positive charge to oxygen vacancy with a no charge and oxygen vacancy with a no charge to VB and are detailed in Chapter 2 [1, 65, 66, 71, 129].

Table 6.1 presents the area of each component under the DLE peak and the R^2 (calculated using residual in FITYK) value for each fit. Analysis revealed that components related the oxygen vacancies with a positive charge are the main contributors to the DLE peak. All components were observed to decrease with argon bombardment, however, the oxygen vacancy with a positive charge, 595 nm, were found to decrease the most.

Table 6.1: Table of curve fitted area and R^2 values of the fits for the defect band before and after argon bombardment.

	543 nm	595 nm	638 nm	765 nm	R^2
0 μA	62.68	134.40	201.93	61.83	0.999
2 μA	62.68	134.40	201.93	61.83	0.999
12 μA	50.84	84.02	153.96	50.94	0.999
19 μA	27.33	42.09	100.74	34.18	0.999
23 μA	21.24	34.82	78.17	26.58	0.999
26 μA	18.43	32.92	66.65	22.75	0.998

The SEM images in Figure 6.7 show that there is no visible difference between the nanowires before and after 2 μA argon bombardment. Increased argon bombardment etched the ZnO nanowires resulting in apparent pitting of the surface and reduced dimensions most notably seen in Figure 6.7 E and F. In these images it can be seen that there is an outline around the nanowire showing the reduction in nanowires diameter from 330 nm for the before treatment nanowires to 270 nm after argon bombardment at 26 μA.

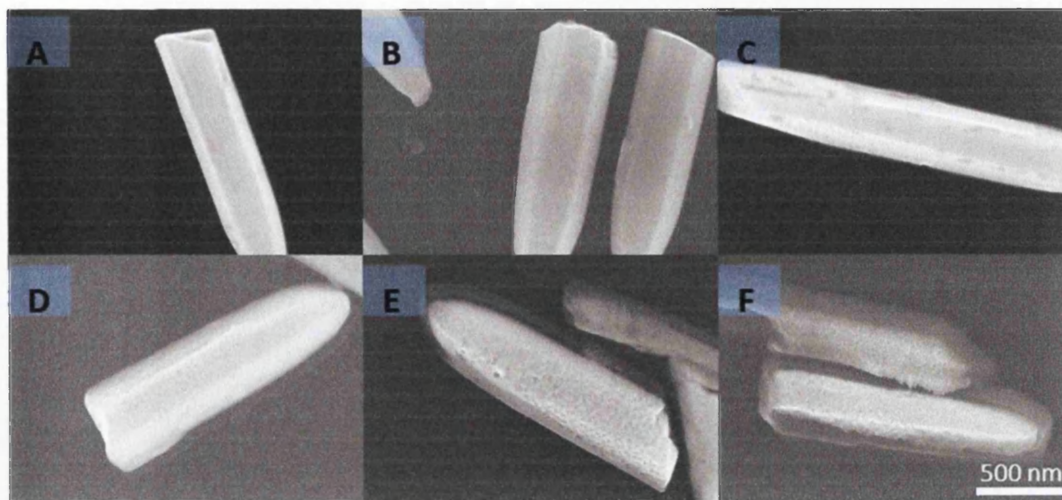

Figure 6.7: SEM images of ZnO nanowires magnified 60.0k after 15 mins of argon bombardment at A) before, B) 2μA, C) 12 μA, D) 19 μA, E) 23 μA, F) 26 μA.

The SEM was also used to carry out EDX and showed that there was 0.04 % argon present in the ZnO nanowires after argon bombardment, which is within the normal background.

Simulations of the observed data were also carried out by Olga Kryvchenkova use the model described here [110, 130-132]. A model for two cases was established, firstly for 'cleaned' nanowires, equivalent to the experimental data following the 2 μA argon dose, and secondly for 'etched' nanowires equivalent to the 26 μA treatment. The cleaned nanowires are modelled as a 330 nm diameter wire, with a doping concentration of 10^{18} cm^{-3}, and a surface charge of 5×10^{13} cm^{-2} to simulate the surface oxygen vacancies identified earlier with PL. For the etched nanorods the diameter is reduced to 270 nm as observed with SEM, the surface charge is removed and the doping concentration is reduced to 10^{16} cm^{-3} in line with the direction of PL change. For both cases a barrier height of φB=0.27 eV was used at the metal-nanowire interface. Figure 6.8 presents typical experimental and simulated I-V curves for the cleaned and etched nanowires.

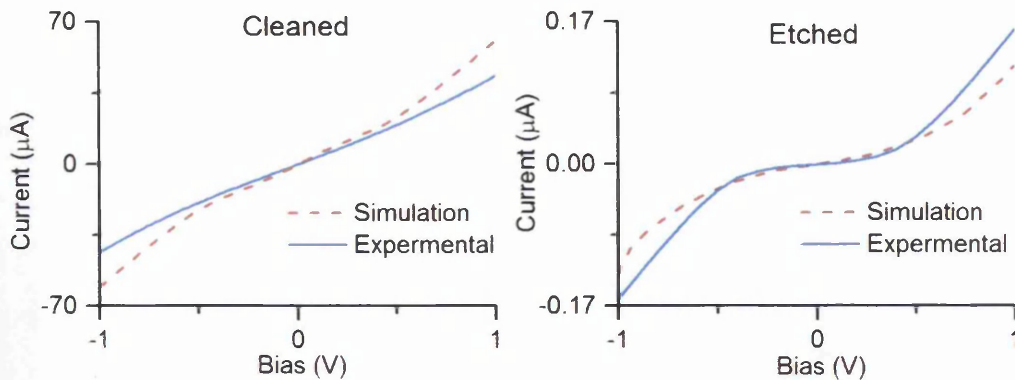

Figure 6.8: I-V characteristics generated using experimental and simulated data for the cleaned and etched nanowires. Simulation data courtesy of Olga Kryvchenkova [12].

The simulation shows that reducing the negative charge on the surface of nanowires causes the current to reduce for a set voltage meaning that the resistance is increasing. The simulation also shows a change from Ohmic to Schottky behaviour as the negative surface charge is reduced, this is in agreement with the experimental results in Figure 6.3 and 6.4.

The results show that a light argon bombardment at 2 μA cleans the surface of the ZnO nanowires as the normalised resistance decreases due to removal of surface contaminants. Further argon bombardment causes the resistance to increase and the intensity of the defects band to decrease. Analysis of the PL spectra shows oxygen vacancy with a positive charge defect decreased the most. Removing this defect causes a reduction in the negative charge and therefore reduces the carrier concentration. This could explain the observed increase in normalised resistance. The reduction in charge carriers also causes the contact type to change from ohmic to Schottky. The removal of negative charge effectively makes the nanowire less n-type and therefore less doped. This causes upwards band bending at the contact resulting in an increased barrier to transport and this is shown below in Figure 6.9. A description of band bending is described in Chapter 3.

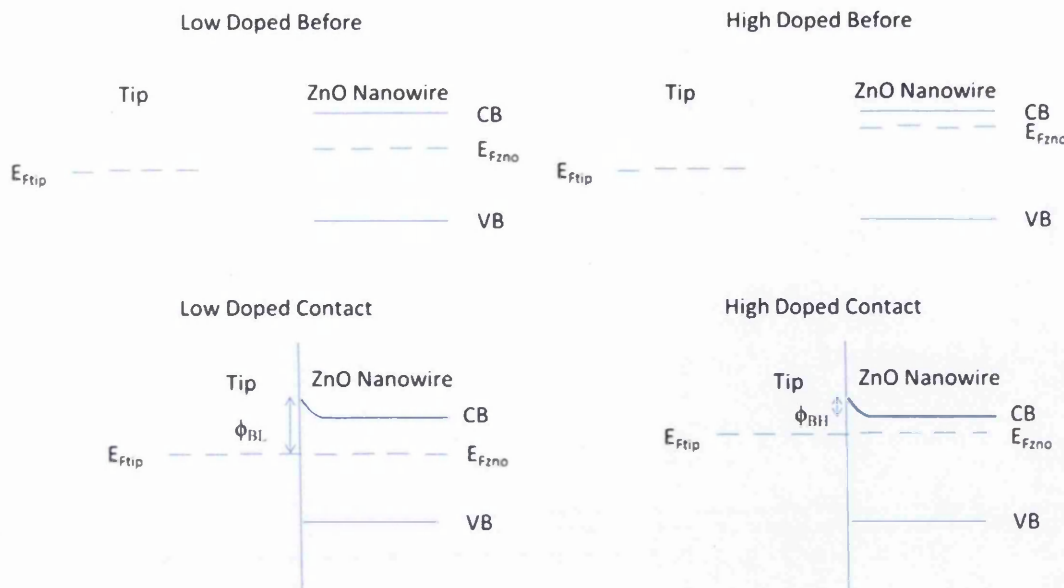

Figure 6.9: Band diagrams of metal tip in contact with high and low doped ZnO.

It can be seen from Figure 6.9 that the barrier from transport from the tip into a low doped nanowire, ϕ_{BL}, is much larger than the barrier for high doped ZnO, ϕ_{BH}. This causes the increased resistance measured and the increase Schottky behaviour when the V_O^+ defects was removed with argon bombardment.

The SEM images show that the neutral $(10\bar{1}0)$ surface of ZnO nanowires were damaged by the argon bombardment and that the size was reduced. This suggests that the oxygen vacancy with a positive charge defects are predominantly in the surface of as-grown nanowires and that the argon bombardment removes the surface resulting in the removal of this defect. EDX was carried out and showed that no argon had been incorporated into the nanowire structure, therefore the reduction in surface charge is not caused by the argon ion chemically interacting with the surface.

An alternative possibility is that the nanowire acts a coaxial cable, which is referenced by Lord et al. [3]. They found that the surface of their CVD synthesised nanowires was in depletion. It is possible that the nanowires are in depletion close to the surface and then in accumulation just inside, with the wire moving towards intrinsic towards the core due the wide nanowires grown, for thin CVD nanowires the core may not go to intrinsic and therefore follows the accepted n-type model. This would cause upwards band bending in the nanowires towards the core and

result in Schottky behaviour observed when the surface layers are removed. This work is still under investigation.

6.2.3 Conclusion

It has been found that a light argon bombardment at 2 μA (0.3 keV) removes surface contaminants from the ZnO nanowires which improves the reproducibility of the contact and reduces the resistance by three orders of magnitude. This is in agreement with Ra et al. who observed a reduction in the nanowires' resistance when subjected to argon plasma [78]. However, they do not attribute the change to cleaning the nanowires but to a decrease number of trapping states on the surface. Further argon bombardment at increased dose causes the resistance to increase and the contact to change from ohmic to Schottky. This is caused by the removal of the surface of the nanowires where it appears the V_O^+ defects are present. Removal of this defect reduces the negative surface charge which results in a larger barrier for electron transport from the tungsten probe. It therefore appears that the V_O^+ defects are responsible for the n-type nature of ZnO nanowires. This agrees with the work carried out by Ha et al., Ra et al. and Law et al. who all found that removing this defect reduces the carrier concentration and therefore increases the resistance [80-82]. They used oxygen and hydrogen plasma treatment of nanowires which would increase the number of oxygen vacancies, however; there is no literature that states that these defects are only present on the surface of the nanowires although it is known that oxygen vacancies migrate to the surface of bulk crystals to stabilise the lattice.

It has also been seen from the results that following Dulub et al.'s recipe [15] will cause too much damage to the ZnO nanowires to obtain atomic resolution using STM. Therefore in the attempt to obtain atomic resolution on single crystal ZnO described in Section 6.4, the argon bombardment power will be reduced to 0.3 keV as it will clean the surface with altering the defect chemistry.

6.3 The Effects of Heating ZnO Nanowires

6.3.1 Method

The LEED experiment carried out in Chapter 6.1 showed that the surface did not sufficiently clean to obtain a clear LEED pattern, this may have been caused by the sample not reaching the 900 °C using the stage heater. It was discussed in Chapter 2 that annealing can affect the properties of the nanostructures. Therefore an experiment has been designed to understand the effects of annealing ZnO nanowires and create heating method where the temperature of the sample is known,

A sample was made in the same way as in Chapter 6.2 using a piece of silicon that had been calibrated for direct current heating using an optical pyrometer. The calibration curve of temperature against current is shown in Figure 6.10 below and has been fitted to a black body approximation.

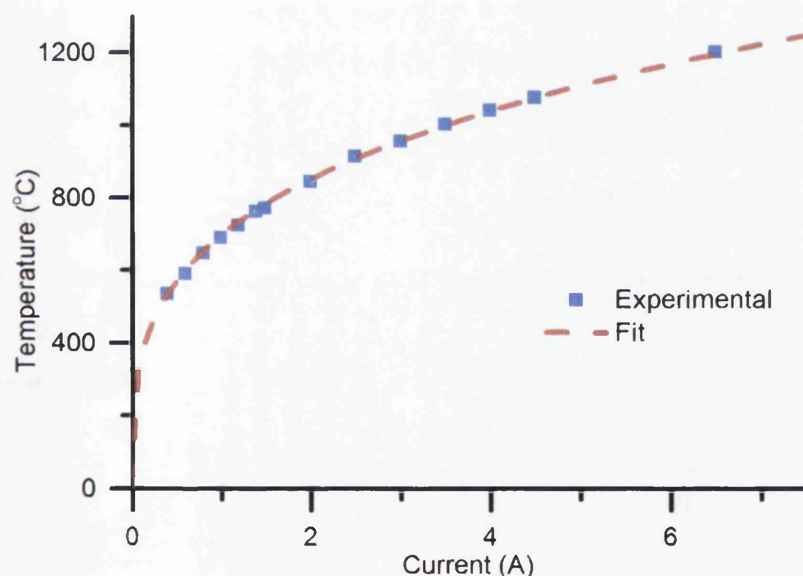

Figure 6.10: Calibration curve for the direct current heating of silicon.

Fitting the curve in Figure 6.10 showed the relationship between the temperature in Celsius of the silicon (T) and the current (I) follows equation 6.1 with an R^2 (calculated using Pearson's r in Orgin Pro) value of 0.998.

$$T = 695.3\ I^{0.29} \qquad (6.1)$$

Using equation 6.1 the silicon with the nanowires was heated from 600 °C to 925 °C for 30 minutes in 25 °C increments. After each annealing the sample was removed from the UHV system and scanned using the SEM.

A second sample was prepared in the same way as the first. It was scanned using SEM and PL then loaded into the Omicron STM. The sample was scanned using the STM until a nanowire was found. STS was then carried out on the nanowire, >60 STS spectra were collected. The sample was then annealed using direct annealing to temperatures 500 °C to 800 °C in 100 °C increments for 1 hour. After each annealing the sample was removed from vacuum and scanned using PL and XPS then replaced in the UHV system and STS carried out. To ensure that changes seen in the oxygen peak were not caused by chemical changes in the native oxide on the silicon substrate, XPS was carried out on pure silicon and again after it was then heated 500 °C, 600 °C, 700 °C and 800 °C.

6.3.2 Results

Figure 6.11 below shows the SEM images of ZnO nanowires heated using the calibrated silicon substrate from 600 °C to 925 °C. It can be seen in Image A that there appears to be small pits with average diameter 12 nm in the surface of the nanowire. These pits increase in diameter as the annealing temperature is increased with the average pit diameter increasing to 31 nm at 700 °C. These pits are coursed by sublimation of oxygen from the ZnO lattice.

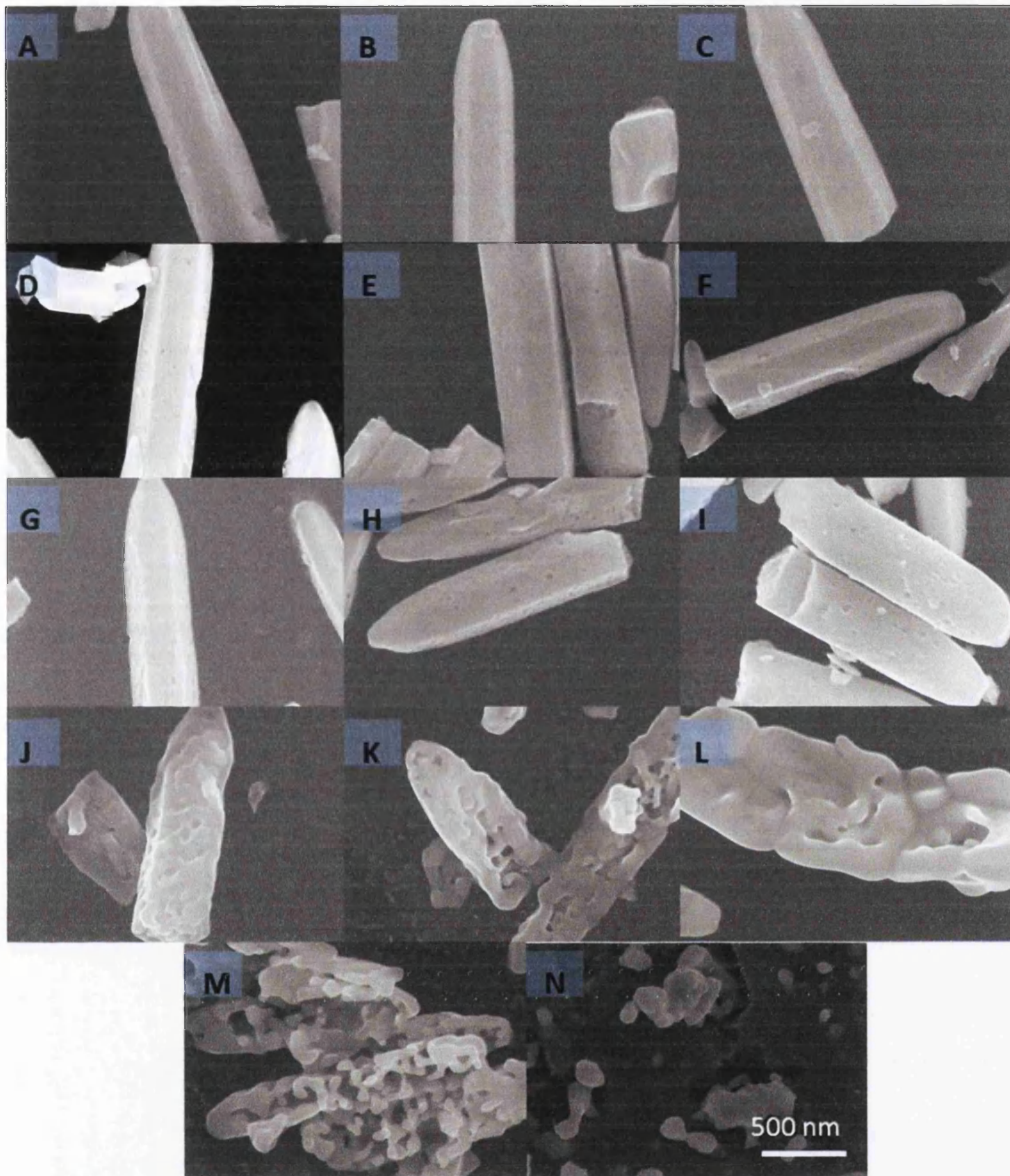

Figure 6.11: SEM images of ZnO nanowires magnified 60.0k after 30 mins heating by direct heating Si substrate A) 600 °C, B) 625 °C, C) 650 °C, D) 675 °C, E) 700 °C, F) 725 °C, G) 750 °C, H) 775 °C, I) 800 °C, J) 825 °C, K) 850 °C, L) 875 °C, M) 900 °C and N) 925 °C.

It can be seen from Figure 6.11 that annealing above 750 °C causes the nanowire to change the hexagonal form of the nanowires. It can be seen from the SEM images increasing annealing temperature to 800 °C results in a nanowire without a clear, well defined hexagonal structure. It appears that annealing to temperatures above 825 °C causes the ZnO nanostructure to sublimate resulting in a globular structure.

To observe the effects of annealing on the defects of the ZnO nanowires PL was carried out on a sample heated to 500 °C, 600 °C, 700 °C and 800 °C. The results are shown below in Figure 6.12.

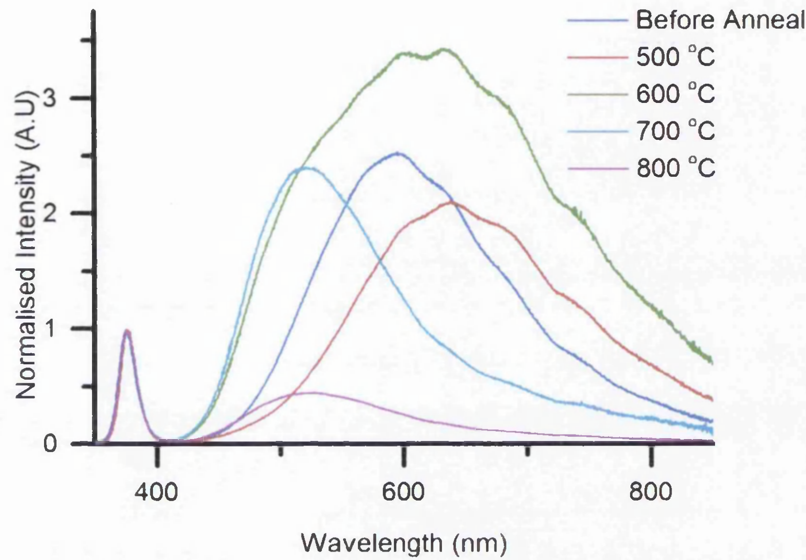

Figure 6.12: PL of ZnO before and after heating.

Figure 6.12 shows that before annealing the PL spectra is of the same form as that displayed in Figure 6.6 with a NBE centred at 376 nm and a defects band with the major component at 595 nm. Table 6.2 below displays the area under each of the fitted curves as well has the R^2 (calculated using residual in FITYK) value of the overall fit of the DLE peak.

Table 6.2: Table of curve fitted area for the defect band for each annealing tempreature.

	520 nm	543 nm	595 nm	638 nm	679 nm	765 nm	R^2
Before anneal	-	34.15	258.44	133.82	-	66.66	0.998
500 °C	-	48.39	17.54	243.15	25.01	126.08	0.994
600 °C	137.02	118.81	78.68	144.85	237.65	381.69	0.996
700 °C	125.74	132.78	28.16	38.76	52.69	59.48	0.995
800 °C	54.17	5.67	15.51	21.96	-	-	0.974

Annealing to 500 °C caused a change in the DLE peak. The major component has changed to a peak centred at 640 nm, which is also due to oxygen vacancies with a positive charge, while the component centred at 595 nm has reduced [1, 69, 71, 73,

74]. The components centred at 679 nm and 765 nm have also increased which are both attributed to oxygen vacancies [66, 68, 133]. It can be seen that increasing the annealing temperature to 600 °C results in a very large defects band as all components increase; also a component centred at 520 nm, which is caused by oxygen occupying a zinc site, appears. Further annealing to 700 °C causes the overall defects band area to decrease as the components centred at 540 nm, 595 nm, 679 nm and 765 nm reduce. However, the peak centred at 520 nm, which has become the major contribution to the defects peak, and 640 nm has increased. Annealing to 800 °C causes all the components to reduce further with the 540 nm, 640 nm, 679 nm and 765 nm components becoming zero. Annealing does not change the position of the NBE peak which always remains centred at 376 nm. This is in agreement with Tarat et al. [87] who also observed no shift when annealing ZnO nanostructures. This suggests that the Pl setup's resolution is too low to measure the shift the NBE emssion caused by the induced lattice strain due to annealing. An experiment carried out by Babikier et al. [134] shows that lattice strain due to annealing shifted the NBE peak by 14 meV. This shift is on the limit of the resolution of the spectrometer used for this thesis. The resolution of the spectrometer used is 0.1 nm that equated to a band gap shift of ~10 meV.

XPS was also carried out after each anneal to characterise whether the composition of the ZnO nanowires were changing. To assess if any change seen was caused by changes in the native oxide of the silicon substrate, plain silicon was also scanned after annealing. Figure 6.13 below shows the narrow scans of the O 1s peaks before and after the silicon was heated at 500 °C, 600 °C, 700 °C and 800 °C. The peak positions were adjusted for charging using the carbon peak using the CasaXPS software.

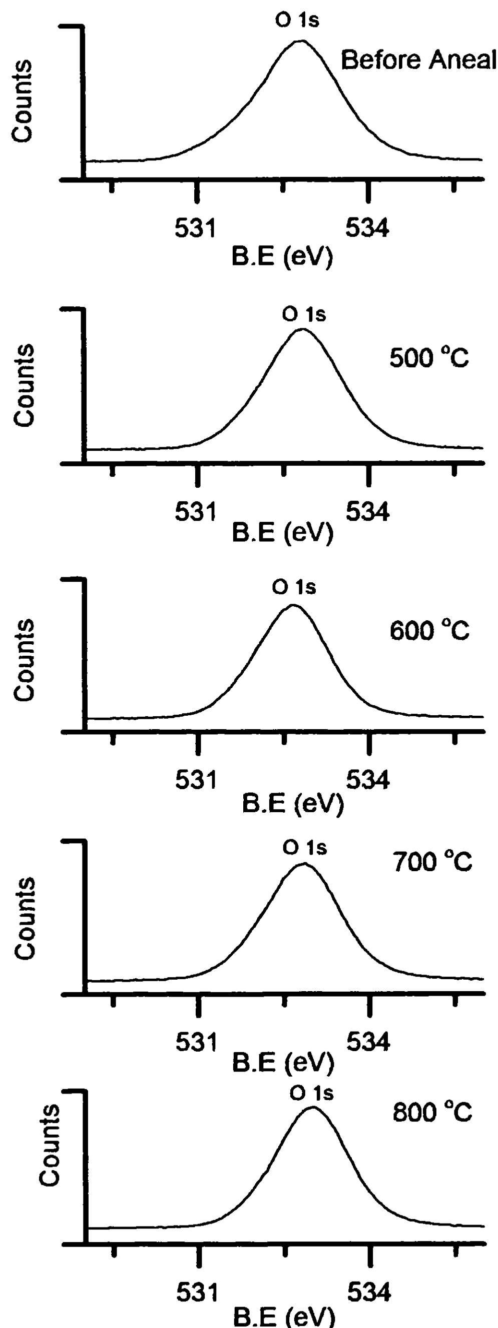

Figure 6.13: XPS scan O 1s peak from Si wafer before and after vacuum annealing at 500 °C, 600 °C, 700 °C and 800 °C.

It can be seen from Figure 6.13 that the O 1s peak appears narrower after annealing at 500 °C and the peak does not does not appear to change shape after annealing at higher temperatures. Curve fitting was carried out using CasaXPS. Three curve where fitted to the O1s peaks centred at 531.04 eV, 532.13 eV and 532.81 eV and the areas and residual STD (calculated in CASAXPS) are present in Table 6.3 below.

These peaks are attributed to SiO bonding, SiO_2 bonding and surface hydroxyls or water. It can be seen that annealing removes the surface hydroxyls or water.

Table 6.3: Table of curve fitted area for the O 1s peak and fits for each annealing tempreature for a Si wafer.

	531.04 eV	532.13 eV	532.81 eV	Residual STD
Before Anneal	14598	58896	25816	3.33
500 °C	5946	118372	-	3.13
600 °C	10082	98936	-	3.12
700 °C	7098	111650	-	3.17
800 °C	3415	95732	-	3.11

XPS were carried out ZnO nanowire sample and the O 1s scans are shown in Figure 6.14 below. It can be seen that for the before anneal, 500 °C and 600 °C spectra contains another peak when compared to the Si sample spectra displaying in Figure 6.13 above. It can also be seen that after annealing at 700 °C and 800 °C that this peak is no longer present and the O 1s peak observed in Figure 6.14 appears broader.

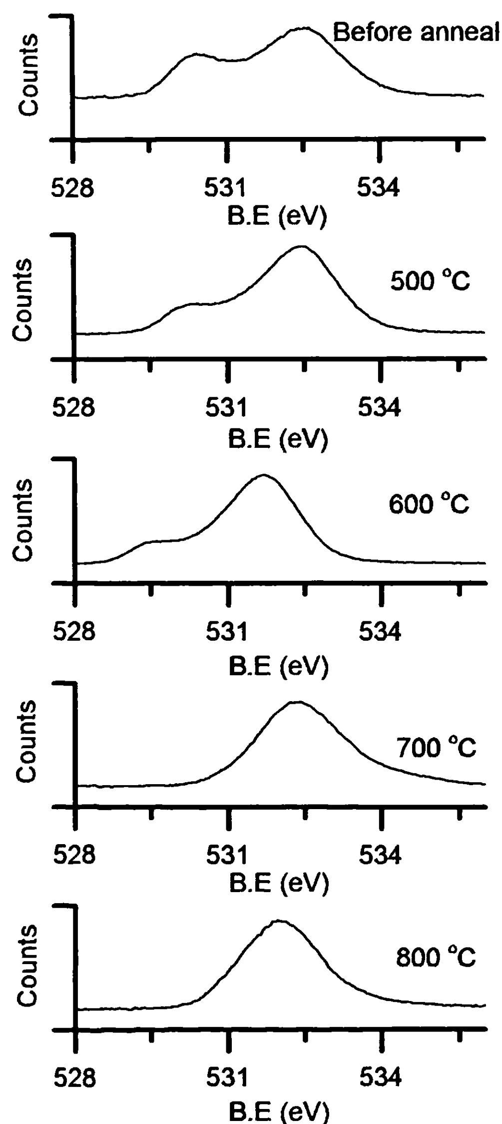

Figure 6.14: XPS scan O 1s peak from ZnO nanowires on a Si wafer before and after vacuum annealing at 500 °C, 600 °C, 700 °C and 800 °C.

Again curve fitting was carried out using CasaXPS. Five curves were fitted: using the three components found from the Si sample and were constrained to have the same relative areas and full width half maximums, a component constrained to have a centre less than 532 eV for the additional peak observed in Figure 6.14 and a component constrained to have a centre greater than 532 eV to account for the peak broadening. It was found that the additional components were centred at 530.12 eV which is attributed to Zn-O bonding and 533.7 eV which is attribute to C-O bonding. The areas of each curve normalised to the SiO_2 O1s component centred at 532.13 eV and the Residual STD (calculated in CASAXPS) are presented in Table 6.4 below.

Table 6.4: Table of curve fitted area for the O 1s peak and fits for each annealing tempreature for a ZnO nanowires on a Si wafer.

	530.12 eV	531.04 eV	532.13 eV	532.81 eV	533.40 eV	Residual STD
Before Anneal	0.52	0.25	1.00	0.40	-	1.34
500 °C	0.20	0.05	1.00	-	-	2.49
600 °C	0.19	0.10	1.00	-	-	4.57
700 °C	-	0.06	1.00	-	0.43	1.13
800 °C	-	0.04	1.00	-	0.29	2.83

It can be seen from Table 6.4 that vacuum annealing the ZnO nanowires at 500 °C and 600 °C results in a drop in the quantity of oxygen bonding to Zn. Annealing at above 700 °C resulted in no measured surface O bonding to Zn. However, the table does show the presence of C-O bonding. This suggests that at 700 °C oxygen is leaving the ZnO lattice and reacting with C contamination on the surface of the nanowires. The XPS results also revealed that the quantity of Zn $2p_{3/2}$ normalised to Si $2p_{3/2}$ measured also varied with annealing temperature and is presented in Table 6.5 below. This indicates that the Zn is sublimating.

Table 6.5: Table of area of Zn 2p3/2 peak normalised to area Si 2p3/2 peak.

	Zn 2p3/2: Si 2p3/2
Before Anneal	10.54
500 °C	4.36
600 °C	3.74
700 °C	3.05
800 °C	0.22

To understand the effects of annealing on electron transport through the ZnO nanowires, STS was carried out. The results are shown in the stacked log plot below in Figure 6.15. To obtain the stacking an offset of two orders of magnitude has been used. Each curve has been generated using an average of least 60 STS spectra and a rolling average of 6 has been applied. The band gap noise has been removed by introducing a noise level removal of 6 pA.

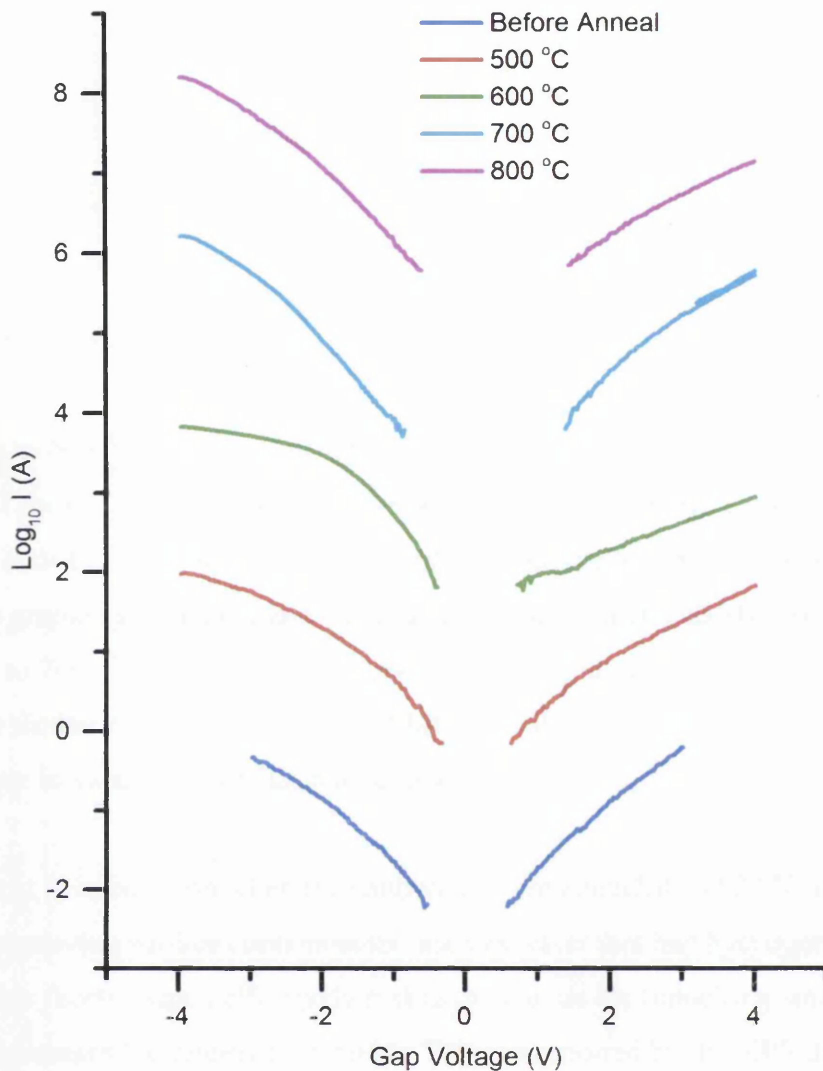

Figure 6.15: STS plots of $\log_{10}$ I against V stacked with increasing annealing temperature.

Figure 6.15 shows that after annealing at 500 °C the apparent band gap has reduced from 1.11 V to 0.75 V and both the CB and VB edges of the log plot have become steeper compared to the before spectra. Table 6.6 presents the apparent band gap and the initial slopes for the CB and VB. The slope was calculated by fitting a straight line to the first 10 data points of the CB and VB edges.

Table 6.6: Table of apparent band gap, VB slope and CB slope before and aftger vacuum annealing.

	Band Gap (V)	VB Slope	CB Slope
Before Anneal	1.11	-1.44	0.92
500 °C	0.75	-1.64	0.99
600 °C	1.10	-1.98	1.15
700 °C	2.23	-0.99	1.10
800 °C	2.28	-0.93	0.67

Annealing to 600 °C causes a widening of the apparent band gap to 1.10 V and the gradient of the CB and VB edges to increase compared to the curve taken after annealing at 500 °C. It can be seen that further annealing to 700 °C and 800 °C causes the gradients of the CB and VB edges to reduce. It can also be seen that annealing to 700 °C and 800 °C caused the apparent band gap to increase. These results are similar to those published by Maffeis et al. [5] who annealed ZnO nanoribbons in vacuum to similar temperatures.

The increase in conduction when the nanowires were annealed to 500 °C is likely to be due to removing surface contaminants, such as water that had hydrogen bonded onto the side facets, which effectively makes the barrier for tunnelling smaller and therefore increases the tunnelling current. This is supported by the XPS data. This is a similar result to that observed in Chapter 6.2 where the argon bombardment removed the surface contaminants and the two point probe measured showed a drop in resistance.

Annealing to 600 °C causes several measurable changes to the nanowires. The STS results show that the apparent band gap has increase to 1.10 V and the gradients of the VB and CB have increase. The PL results show that there is a large increase in the number of oxygen vacancies without charge, peaks centre at 679 nm and 765 nm, compared to annealing at 500 °C. There is also an increase in the peak centred at 595 nm suggesting that the number of donnor dopants have increased. This would result in the steeper VB and CB edges. The PL also shows that the number of oxygen anti-sites have increased [65-67] .This defect is ab acceptor and therefore subtracts

from the effects of the increase in donors [76]. This explains the widening in the apparent band gap.

The increase in oxygen anti-sites zinc site also explains the small pits seen in the SEM images when the ZnO nanowires were annealed at 600 °C. The zinc sublimating from the lattice producing the pits as the zinc leaves the nanostructures. It was seen that annealing at 500 °C caused oxygen atoms to leave the lattice and change from interstitial to vacancies. It can be seen from the PL results that the number of interstitials has increased since the peak at 595 nm has also increased. The oxygen interstitials have moved from lattice sites and therefore it is possible that lattice site oxygen has also moved into the vacated zinc sites.

The STS results showed annealing to 700 °C caused the conduction of the ZnO nanowires to decrease and the apparent band gap to increase. This could be caused by the increase in the acceptor defects centred at 520 nm and the decrease in the donor defects centred at 595 nm. Although the defect centred at 640 nm has increased slightly, this is likely to be caused by interstitial oxygen moving out of the lattice to leave only oxygen vacancies. It has been seen from the PL results that the overall number of oxygen vacancies with no charge has decreased. It was also seen from SEM images that the surface of the nanowires had started to melt. It appears that melting the surface sublimated the zinc and therefore there can be no oxygen vacancies remaining in the surface and the results from the argon bombardment showed that these defects are only present in the surface. The PL results show that oxygen occupying a zinc site defect is the main component of the defects band after the ZnO nanowires were heated to 700 °C. The reason for this is the same as that described above when the nanowire was heated to 600 °C, the zinc sublimates and oxygen atoms move to occupy the free sites.

Annealing to 800 °C caused a further reduction conductance. This is caused by further removal of the surface and V_O^+ defects due to the melting of the nanostructure. The PL results also show that the oxygen occupying a zinc site defect has also reduced since the ZnO nanowire has melted and the crystal structure has been damaged.

6.3.3 Conclusion

It was found that ZnO nanowires sublimated at temperatures 825 °C which is lower than the temperature used by Dulub et al. and therefore their recipe cannot be used to clean ZnO nanowires. It was also seen that damage started to occur at 600 °C and annealing to 500 °C caused changes to defects and conductance of the nanowires.

Annealing at 500 °C caused the conductance to increase as the surfaces of the nanowires were cleaned of surface contaminants and a possible increase in the number oxygen vacancies with a positive charge. It was also seen that oxygen interstitials reduced as the oxygen atom left the lattice and left behind non-charged vacancies. Annealing to 600 °C caused the defects band to increase in area as oxygen lattice site atoms move to interstitial positions and interstitial oxygen moved to vacancies. This should have increased the conductance further, however, curve fitting the PL data revealed that the oxygen anti-sites defect had also increased from zero. This defect is an acceptor and therefore effectively reduces the conductance of the n-type ZnO. Further annealing to 700 °C and 800 °C caused the conductance to decrease as the oxygen anti-sites defect becomes the dominant observed defect. This was due to the removal of the surface through sublimation of the surface zinc which therefore removed the oxygen vacancies and oxygen moving from the lattice into the free zinc sites.

6.4 STM of Single Crystal ZnO

6.4.1 Method

Using the information gathered from the experiments carried out in 6.2 and 6.3, the experiment in 6.1 was repeated using a lower dose of argon bombardment and heating to 600 °C. A piece of single crystal ZnO was cut to 5 x 2 nm using a diamond scribe so that it was smaller than the window in the Omicron sample plate. The single crystal ZnO was stuck onto a piece of silicon that had been calibrated for

direct current heating. ESL 5545 platinum conductive composite paste was applied to the silicon to secure the ZnO. To set the paste the sample was annealed in a tube furnace for 20 minutes at 400 °C which was significantly lower than the manufacture's recommended curing temperature. This was done to ensure that electrical resistance did not change from 10 MΩ when measured using a MegaOhm.

The sample was loaded into the preparation chamber of the Omicron VT AFM/STM and LEED was carried out. The sample was then treated with cycles of 15 minutes of argon bombardment using 0.3 keV (sample current of 2 μA) and annealing at 600 °C for one hour. After each cycle the sample was allowed to cool for 30 minutes then LEED was carried out. When a clear 2 x 1 LEED pattern was obtained the sample was moved through to the STM/AFM chamber and STM was carried out.

To ensure the STM had the highest chance of obtaining atomic resolution two tips were cleaned using the current annealing technique described in Chapter 4. The tips were then checked by obtaining atomic resolution on 7 x 7 silicon. The silicon was prepared by direct current annealing silicon at 7.8 A (1200 °C) for 8 seconds then slowly turning down the current to 0 A. The STM images of silicon from two tips are shown in Figure 6.18. It can be seen that the images are similar to those obtained by Naffer et al. in Figure 2.1 [17] and the Si atoms are clearly seen in both forward bias and reverse bias.

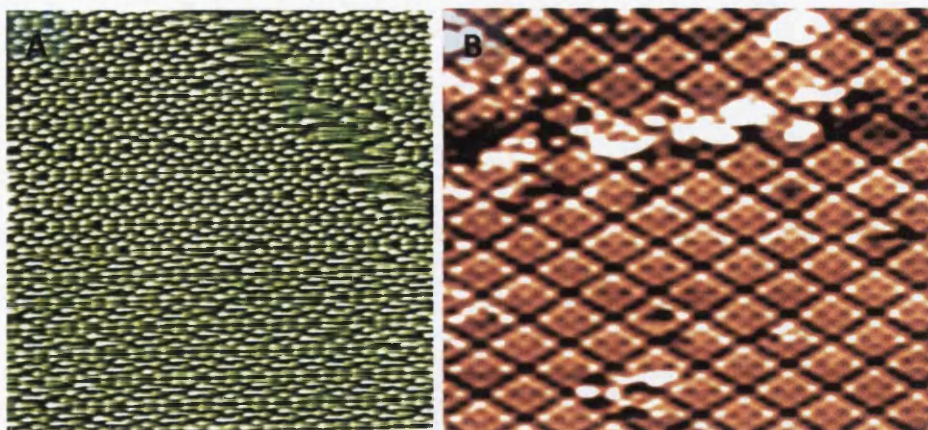

Figure 6.18: STM images of 7x7 silicon. A) Negative voltage applied to tip 1, B) positive voltage applied to tip 2.

6.4.2 Results

Figure 6.16 below, shows a series of pictures of the LEED patterns taken before and after each cycle of argon bombardment and heating. It can be seen that before treatment that no LEED pattern was obtained since the single crystal ZnO has no long range order. This is the same result as shown above in Figure 6.1 A. Figure 6.16 shows that after one cycle of treatment a LEED pattern can be obtained. The pattern obtained is of the expected 2 x 1 form for ZnO. However, it can be seen from the image below that some of the points are not present and therefore the long range order is interrupted so that atomic resolution would be unlikely using STM.

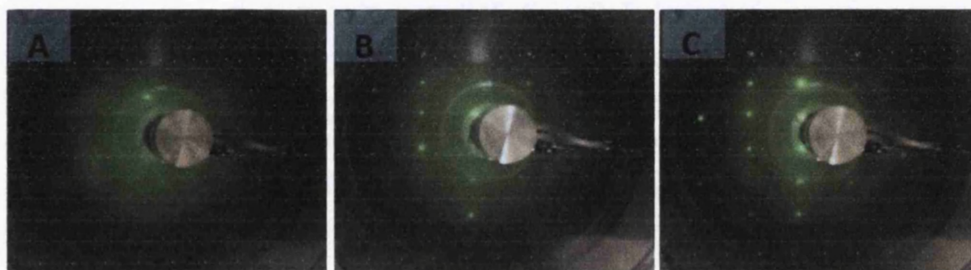

Figure 6.16: LEED of single crystal ZnO ($10\bar{1}0$) taken at 151.1 eV A) before treatment, B) after 1 cycle of 0.3 keV Ar bombardment for 15 mins and 1 hour of heating at 600 °C, C) after 2 cycles of 0.3 keV Ar bombardment for 15 mins and 1 hour of heating at 600 °C.

Figure 6.16C shows that after two cycles of argon bombardment at 0.3 keV for 15 mins and annealing using a silicon substrate at 600 °C for an hour causes a clear surface to be reconstructed. The pattern is also clear across the whole hemisphere of the LEED detector, which did not occur after one cycle of treatment. The pattern obtained is very similar in quality to that obtained by Dulub et al. which is shown in Chapter 2 in Figure 2.3 [15]. STM was then carried out. The STM images are shown below in Figure 6.17. The scan set used were: Setpoint 0.5 nA, gap voltage -3V and scan speed 33 nm/s.

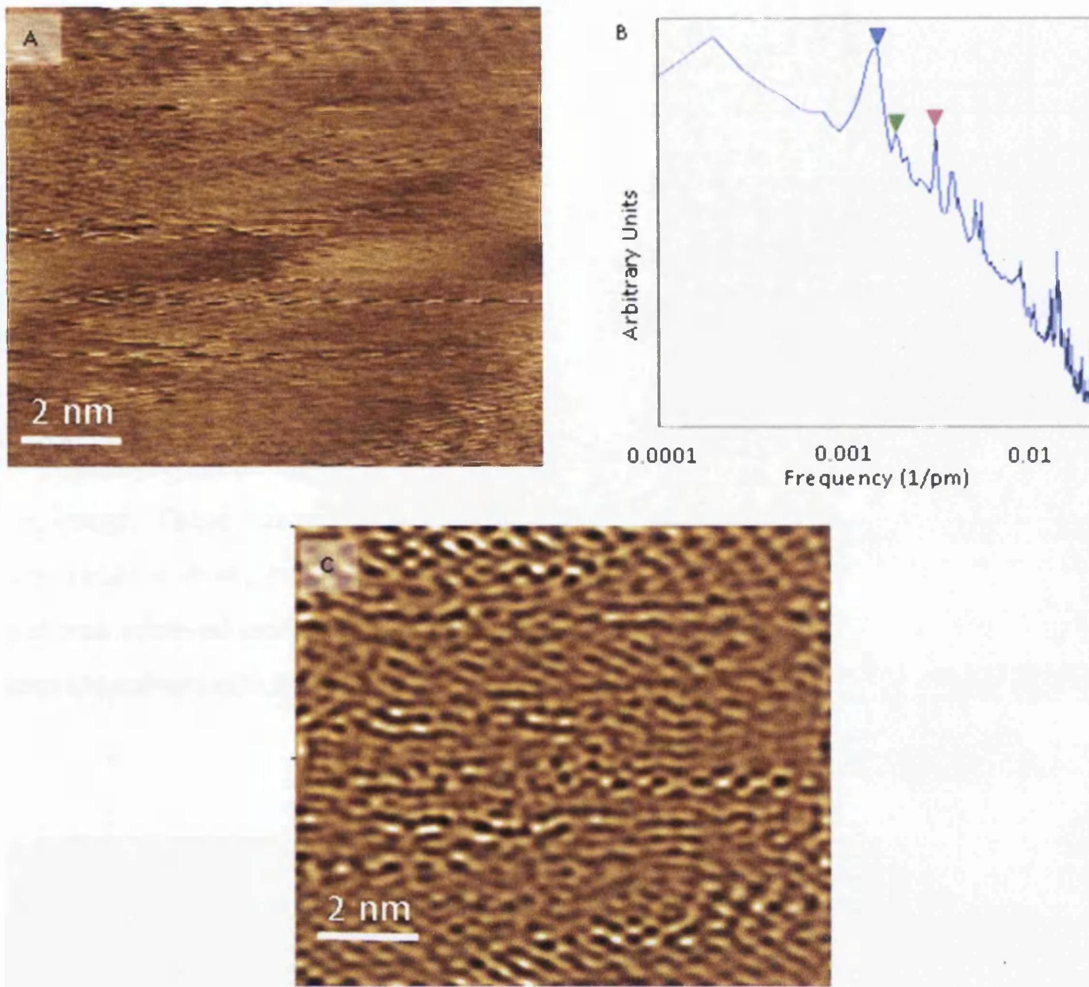

Figure 6.17: A) STM images of the (10$\bar{1}$0) surface of ZnO single crystal, B) Fourier transform plot of raw data and C) STM images of the (10$\bar{1}$0) surface of ZnO single crystal process using SPIP to filter out high frequency noise.

Figure 6.17 A shows the initial STM scan which was 10 nm by 10 nm. The image has been plane corrected using global level and linewise bow removal. Global levelling is a 1 st order plane correction that removes small surface corrugations. Linewise bow removal removes the bow from the Z-axis caused by the sweep of the probe. It can be seen that at the top and bottom right corner of the image there is a periodic feature. A 2D Fourier analysis of image A is shown in image B; it can be seen that there are several peaks. The peak marked with the pink arrow has a frequency value of 0.0030 pm^{-1} which equates to a wavelength of 0.33 nm which is the *a* lattice parameter. There is also a harmonic of this frequency indicated by the blue arrow with a value of 0.0015 pm^{-1} which equates at a wavelength of 0.65 nm which is the 2*a* lattice parameter.

The Fourier transform plot also shows a peak centre at 0.0018 pm^{-1}, indicated by the green arrow. This peak equates to 0.52 nm which is the *c* lattice parameter. The plot also shows several peaks of higher frequency such as the peak indicated by the turquoise arrow. These peaks are caused by high frequency noise. The peak centre at 0.007 pm^{-1} is caused by electrical noise at 50 Hz. Therefore the original STM data was filtered using a band pass to only include wavelengths between 0.31 nm and 0.84 nm. The result is shown in image C above.

It can be seen from Figure 6.17 C that there is a feature at the top and bottom right of the image. These features may be the atoms in the crystal. An image with a reduced scan range is shown below in Figure 6.18. The scan range for this image is 2 nm and was achieved using a scan speed of 3 nm/s with a gap voltage of -3 V and a setpoint current of 0.5 nA.

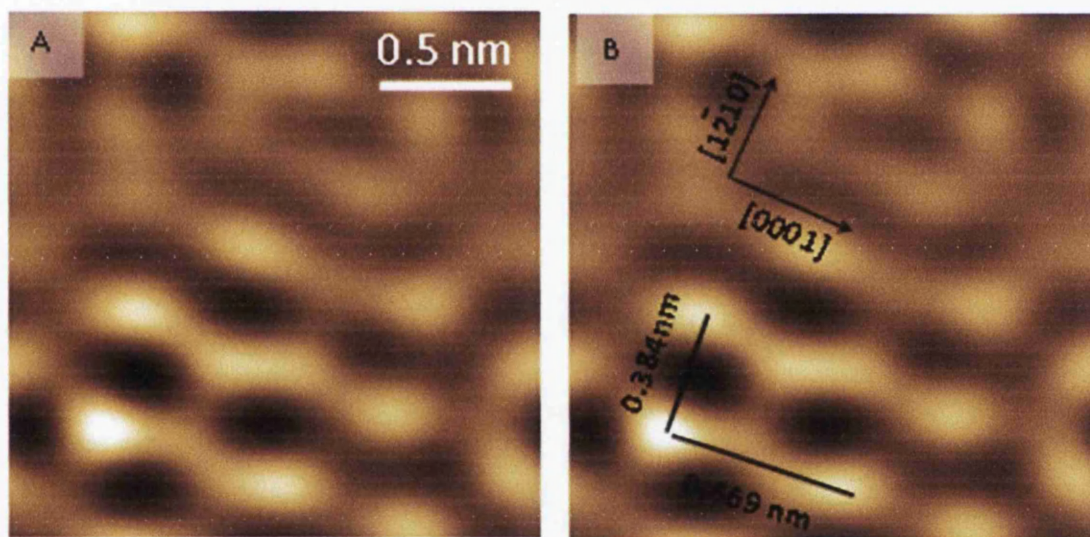

Figure 6.18: A) STM images of surface of ZnO single crystal process using SPIP to filter out high frequency noise and B) STM images of surface of ZnO single crystal process using SPIP to filter out high frequency noise with measurement of the unit cell.

Figure 6.18A shows that although the STM scan is not stable over the whole range of 2nm, there are small regions where atomic resolution has been achieved and the unit cell is marked in Figure 6.18B which matched the expected lattice parameters. The measurements for both the 2 *a* and *c* parameter are larger than those stated in

Chapter 2 at 0.65 nm and 0.5 nm, however. These values are larger than the expected lattice parameters and is caused by surface atoms undergo relaxation [135]. The images have been levelled as before and filtered.

6.4.3 Conclusion

It has been seen that single crystal ZnO can be cleaned using 0.3 keV of argon bombardment and heating to 600 °C. It was seen from the LEED images that 2 cycles of treatment caused a 2 x 1 surface reconstruction similar to that seen in the literature. However, STM found that large areas of the sample were not of atomic order and it was therefore not possible to achieve full atomic resolution. Analysis and processing of a 10 x 10 nm scan showed that there were row like features in parts of the scan which were similar to those seen by others in Chapter 2. A reduced scan range of 2 nm along with image processing using SPIP was used to show short range near atomic resolution of a unit cell. Therefore this cleaning recipe was used on ZnO nanowires.

6.5 STM of ZnO Nanowires

6.5.1 Method

Again ZnO nanowires were rubbed onto a piece of calibrated silicon for direct current annealing and placed onto an Omicron direct heating plate for the LT Nanoprobe. The Nanoprobe was used for this experiment since it has an SEM which allowed quick position of the STM tip on a nanowire. The sample was treated with two cycles of Ar bombardment for 15 minutes and heated to 600 °C for 1 hour using direct current heating of the silicon. The Ar bombardment dose was kept the same as that used in Chapter 6.4 by measuring the sample current, for this the sample current used was 2 μA.

Once the sample had cooled it was placed onto the scanning stage. A tungsten probe, that had been cleaned using direct current annealing, was lowered towards a nanowire and positioned over a suitable facet. When the tip was close to the sample it was auto approached using a set point of 0.1 nA, 10 % gain and a gap voltage of 2.5 V.

Once the tip was in tunnelling contact with the nanowire the tip was withdrawn 20 course steps and the SEM turned off and the stage floated on the Eddy current dampening system. The tip was then auto approached again and allowed to scan. The gain was adjusted to minimise the noise. The set point was also increased to 1 nA and the gap voltage reduced to 2 V to increase the signal to noise.

6.5.2 Results

Figure 6.19 below shows the initial STM scan of a ZnO nanowire which has been levelled using SPIP's plane correction functions global levelling and linewise bow removal. There are no discernible features on the image which suggest that there is no contamination or terraces. Roughness analysis using SPIP showed that the average surface rough was 0.045 nm which is very low.

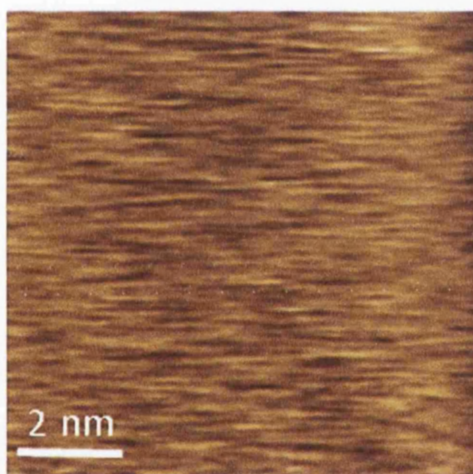

Figure 6.19: STM images of surface of a ZnO nanowire.

Figure 6.20 below shows the STM images shown in Figure 6.19 which has been filtered using an ideal band pass filter. The settings used were the same as that used in Chapter 6.4 above to remove the low and high frequency noise. Figure 6.20 also shows a 3D plot.

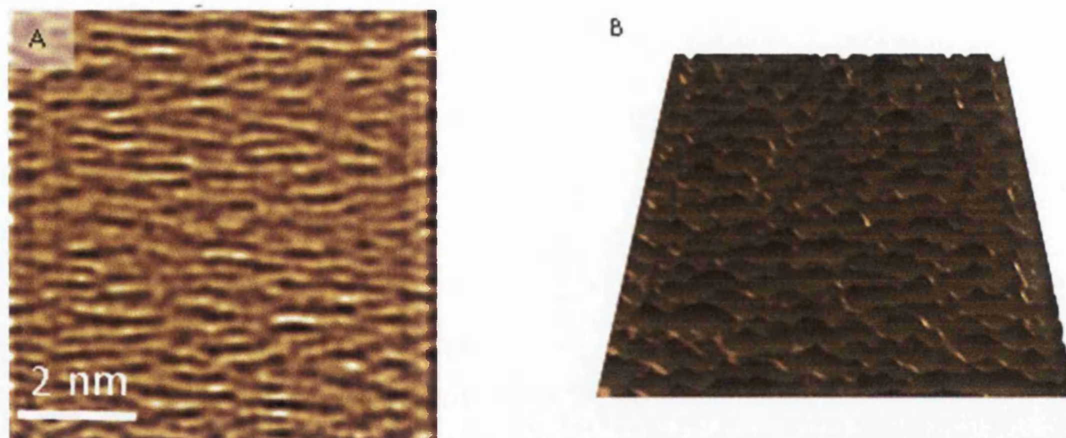

Figure 6.20: A) STM images of the (10$\bar{1}$0) surface of a ZnO single nanowire processed using SPIP to filter out high frequency noise and B) 3D STM images of surface of a ZnO single nanowire processed using SPIP to filter out high frequency noise.

It can be seen from Figure 6.20 that there appears to be trenches running across the sample. The average distance between the trenches was calculated to 0.361 ± 0.021 nm. These trenches are separated by the *a* lattice parameter and is comparable with the spacing of 0.38 nm between the atoms found in Figure 6.18. Again the lattice parameter is greater than that quoted in the literature for the bulk but this is caused by surface atom relaxation.

6.5.3 Conclusion

STM has been attempted on ZnO nanowires after cleaning using argon bombardment and vacuum annealing. Processing the image revealed a series of trenches that are separated by the *a* lattice parameter. Atomic resolution was not achieved.

6.6 The Effects of Heating ZnO Nanosheets

6.6.1 Method

ZnO nanosheets were synthesised in an 800 W microwave using a 500 ml solution containing 0.1M of zinc acetate and 0.04 M of HMTA. The solution was heated in a glass beaker for 6min at full power. 10ml of the solution was then poured into a 15 ml centrifuge tube and centrifuged 5 times at 4000rpm for 5 mins. After each centrifuge the supernatant was removed and the solution made back up to 10 ml by adding DI water. The concentrated nanosheets were then diluted by adding 6 ml of

DI to 2 ml for the concentrate. 10 μL was then deposited onto silicon with 100 nm of thermal oxide (referred to as Sample 1) and two pieces of n-type (100) silicon and all three samples were initially annealed in air at 400 °C to thermally decompose the LBZA to ZnO.

The Sample 1 was placed onto a single tiered Omicron Nanoprobe sample plate and loaded into the Omicron LT Nanoprobe. Two tungsten probes were approached onto nanosheets using the method described in Section 6.2.1 above. Five I-V curves were taken, the first using a range of -1 V to 1 V, the second using a range of -2 V to 2 V, the third using a range of -3 V to 3 V, the forth using a range of -4 V to 4 V, and the fifth using a range of -5 V to 5 V. One of the tips was then moved to a new position on the nanosheet and the five I-V sweeps repeated. This was then repeated for three move positions on the nanosheets. The five tip positions are shown below in Figure 6.21 (A-E). The sample was then heated to 300 °C using the Nanoprobe's preparation chamber stage heater for 1 hour. The sample temperature was measured using an in-built thermal couple. After annealing the sample was allowed to cool and the 2 point probe measurements repeated. The same nanosheets were used and the tips were placed in the same positions on the nanosheets, shown in Figure 6.21. (F-J). This was repeated for annealing to 500 °C and 800 °C.

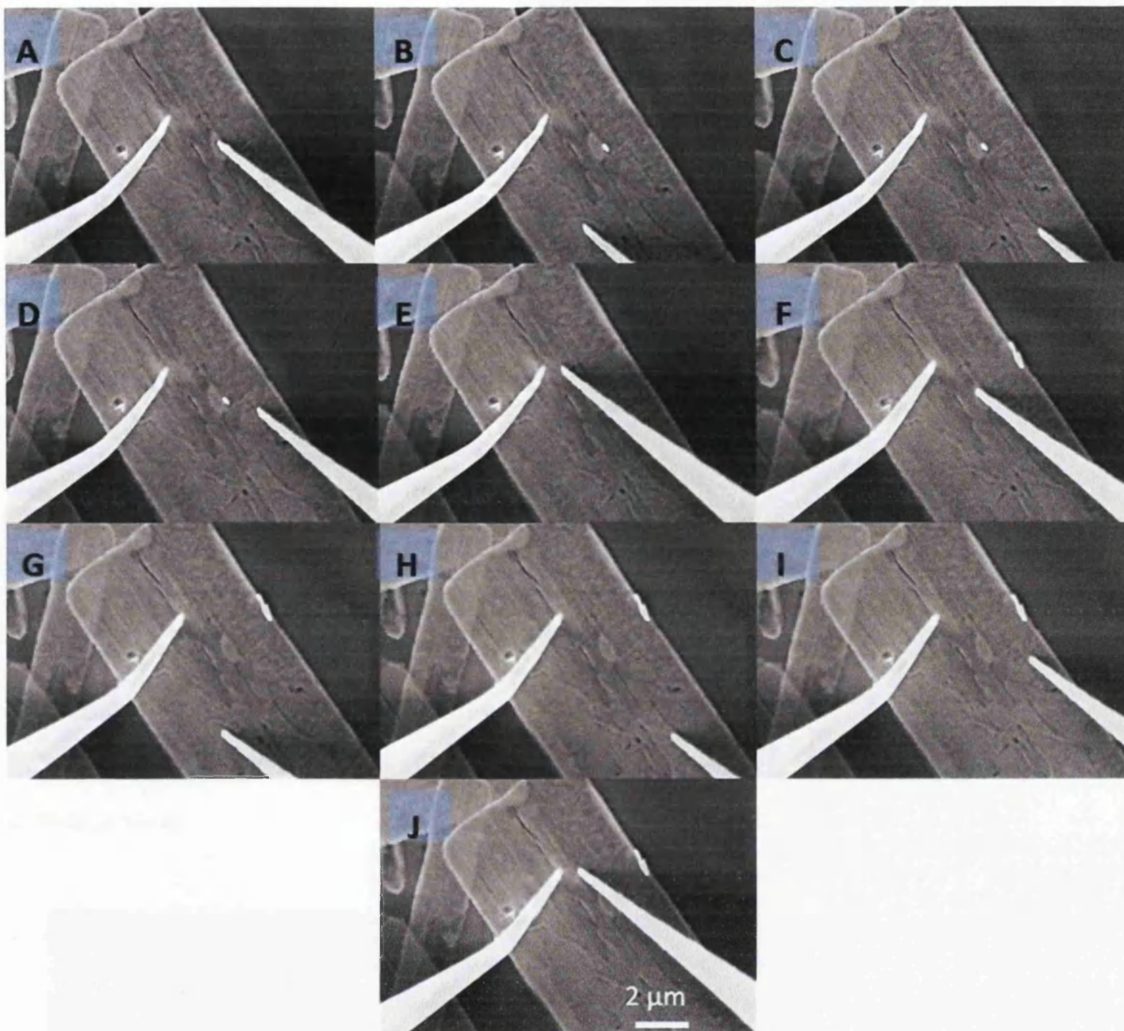

Figure 6.21: SEM images of tip position A) position one before annealing, B) position two before annealing, C) position three before annealing, D) position four before annealing, E) position five before annealing, F) position one after annealing to 300 °C, G) position two after annealing to 300 °C, H) position three after annealing to 300 °C, I) position four after annealing to 300 °C and J) position five after annealing to 300 °C

Sample 2 was characterised before vacuum annealing and after vacuum annealing at 300 °C, 500 °C and 700 °C for 1 hour with AES. As before the annealing was carried out using Nanoprobe's preparation chamber stage heater. The AES was performed at 20 k magnification using a beam acceleration voltage of 5 kV and 1 nA beam current through a 90 µm beam aperture.

Sample 3 was characterised before vacuum annealing and after vacuum annealing at 300 °C, 500 °C and 700 °C for 1 hour with high resolution SEM and PL at room temperature. Again the vacuum annealing was carried out use the Nanoprobe's

preparation chamber stage heater. This meant that this sample had to be removed from UHV for characterisation.

6.6.2 Results

Figure 6.22 shows SEM images of the grain structure before and after vacuum annealing. Before vacuum annealing the average grain size was 5 ± 1.3 nm, as measured from one representative high resolution SEM frame. After annealing to 300 °C, the grains sintered to form clusters of around 50-100 nm. The sintered grain size was much larger than that measured by Tarat et al. [87] following similar annealing in air and is more comparable to annealing at 800 °C in air. This is likely due to the effect of the melting point dependence on pressure, which is well-documented [136, 137]. At 500 °C the grains sintered further, whilst at 700 °C the nanosheets appear much darker, as shown by the SEM image in Figure 6.22d indicating lower conductivity, and show signs of fracturing and partial disintegration.

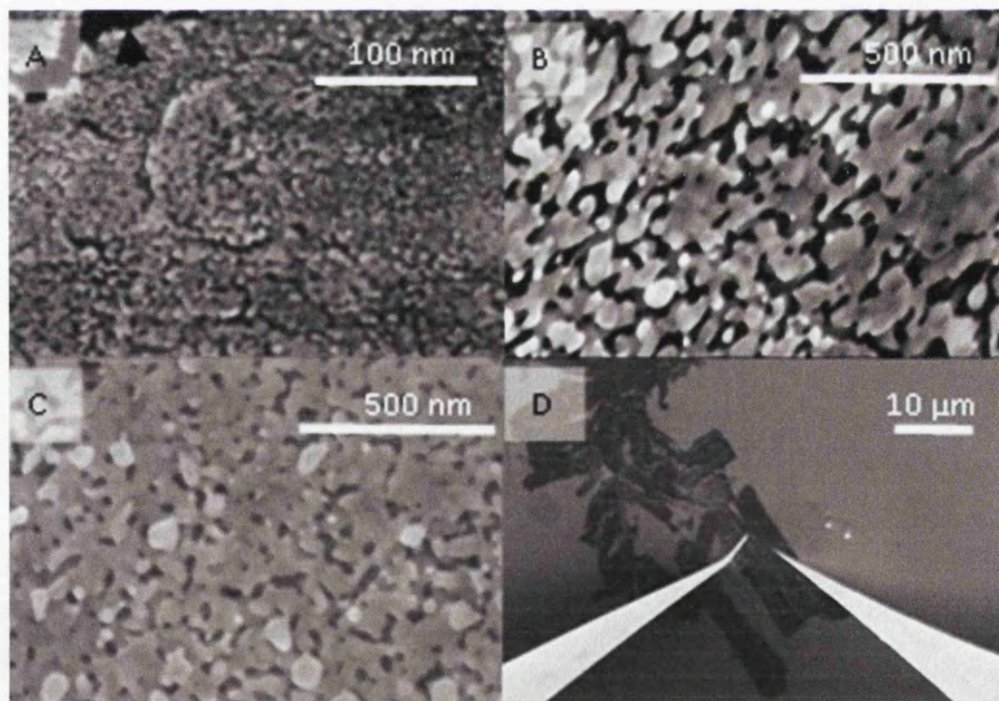

Figure 6.22: SEM images of ZnO nanosheets a) before vacuum annealing with an arrow marking a void and after vacuum annealing at b) 300 °C, c) 500 °C and d) 700 °C.

In Figure 6.23 the mean nanosheet resistance at +1 V measured using two point probe is shown against probe separation. One outlier with a standard deviation more than twelve times the average was removed. For homogenous materials a standard resistivity model would give a linear increase with probe separation. For polycrystalline materials the resistance primarily increases in a step-like fashion across the grain boundaries [138]. However, since the grain size here is much smaller than the length scale shown, the trend should still be linear. Therefore perturbations away from linearity in the data in Figure 6.23 are not caused by the polycrystalline nature of the nanosheets. Instead these are likely caused by dislocations and voids in the nanosheet, some examples of which are indicated by the arrow Figure 6.22a. The same discontinuities are present in the 300 °C and 500 °C data but are reduced in magnitude as the total resistance reduces. The 300 °C and 500 °C data is shown magnified in the inset in Figure 6.23.

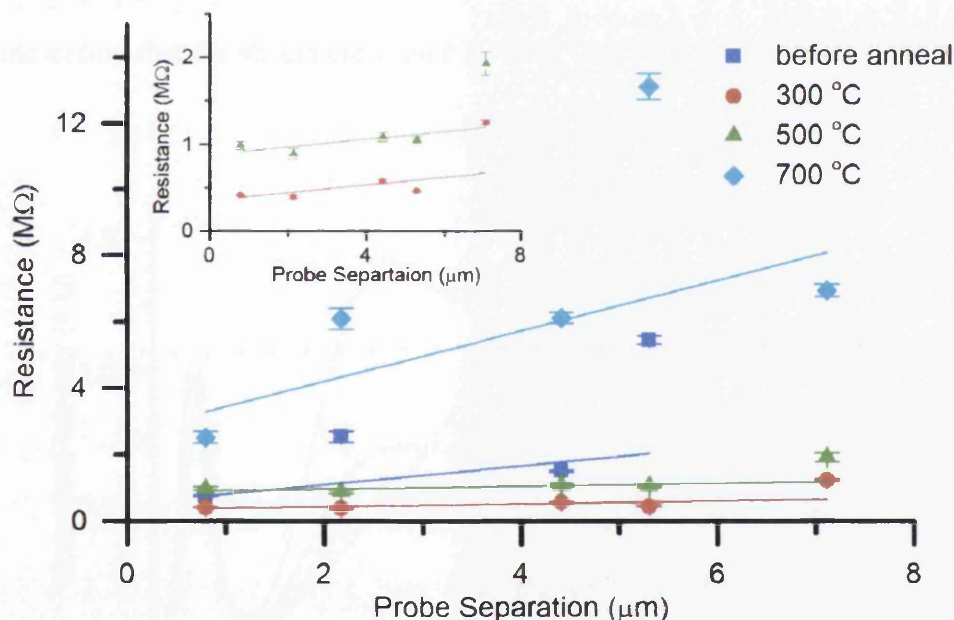

Figure 6.23: Mean two point probe resistance measurements at +1 V with standard deviation, against probe separation for ZnO nanosheets before and after vacuum annealing at 300 °C, 500 °C and 700 °C, with inset showing 300 °C and 500 °C. A least squares linear fit is overlaid for all.

The regression coefficients are improved after annealing at 300 °C and 500 °C to 0.771, The poorer fit of the prior non-annealed case, regression coefficient 0.469, is

attributed to inconsistent probe-nanosheet contacts due to surface contaminants which are removed during annealing [139]. The regression coefficient at 700 °C decreased to 0.324 due to the partial disintegration of the nanosheet structure as discussed earlier.

PL spectra shown in Figure 6.24 are normalised to the near band edge (NBE) peak which remained centred at 378 nm for all annealing stages. Before annealing, the DLE peak maximum is at 640 nm with peak fitting indicating constituent components centred at 543 nm, 595 nm, 635 nm, 690 nm and 765 nm. These components correspond to transitions from: the CB to an oxygen interstitial with no charge [66, 71, 72, 133] an oxygen vacancy with a single positive charge to an oxygen interstitial with no charge [69, 71, 73], an oxygen vacancy with a single positive charge to an oxygen vacancy with no charge [74], an oxygen vacancy with no charge to the valance band [67], the CB to an oxygen vacancy with no charge [66-68], respectively. These DLE transitions are caused by electron donor defect states indicating that the sheets are n-type [1].

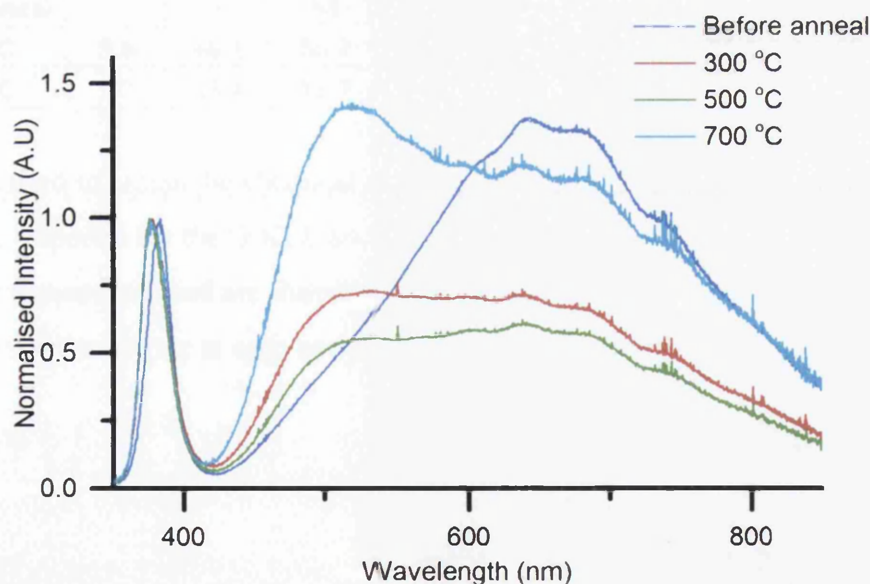

Figure 6.24: PL spectra of ZnO nanosheets before and after vacuum annealing at 300 °C, 500 °C and 700 °C.

After annealing to 300 °C, the intensity of the DLE peak to decrease relative to the NBE with the components remaining centred at the same positions. However, annealing caused components centred at 470 nm and 520 nm to increase which are

attributed to the acceptor defect transitions: an interstitial oxygen ion with a single negative charge [65] and an oxygen anti-site [65-67]. The component centred at 543 nm also increases. Table 6.7 presents the data from the curve fitting and show the areas of the components and the R^2 (calculated using residual in FITYK) values for each fit. Further annealing to 500 °C caused the intensity of the DLE peak to decrease relative to the NBE with all components reducing. This is the same effect as seen in by Tarat et al. [87] when they annealed ZnO nanosheets in air at 1000 °C, although annealing in UHV causes the effect to occur at a much lower temperature. Annealing to 700 °C caused all components of the DLE peak to increase relative to the NBE peak. However, the SEM images show that there is significant damage to the ZnO nanosheets, therefore the PL spectrum for the nanosheets annealed to 700 °C is not reliable. Also the one of the three PL spectra taken from the sample after annealing at 700 °C did not display an NBE peak.

Table 6.7: Table of curve fitted area normalised NBE for the DLE peak before and after vacuum annealing at 300 °C and 500 °C.

	470 nm	520 nm	543 nm	595 nm	638 nm	679 nm	765 nm	R^2
Before aneal	-	-	58	5.7	53.9	124.2	129.5	0.978
300 °C	8.6	46.2	66.7	3.9	27	78.7	58	0.998
500 °C	5.3	23.4	11.7	2.4	19.6	33.7	36.1	0.995

AES was used to assess the chemical composition of the ZnO nanosheets with annealing. Spectra for the O KLL and Zn LMM transitions were collected from two points on a nanosheet and are shown in Figure 6.25. Two silicon spectra were also taken from the substrate at each annealing stage.

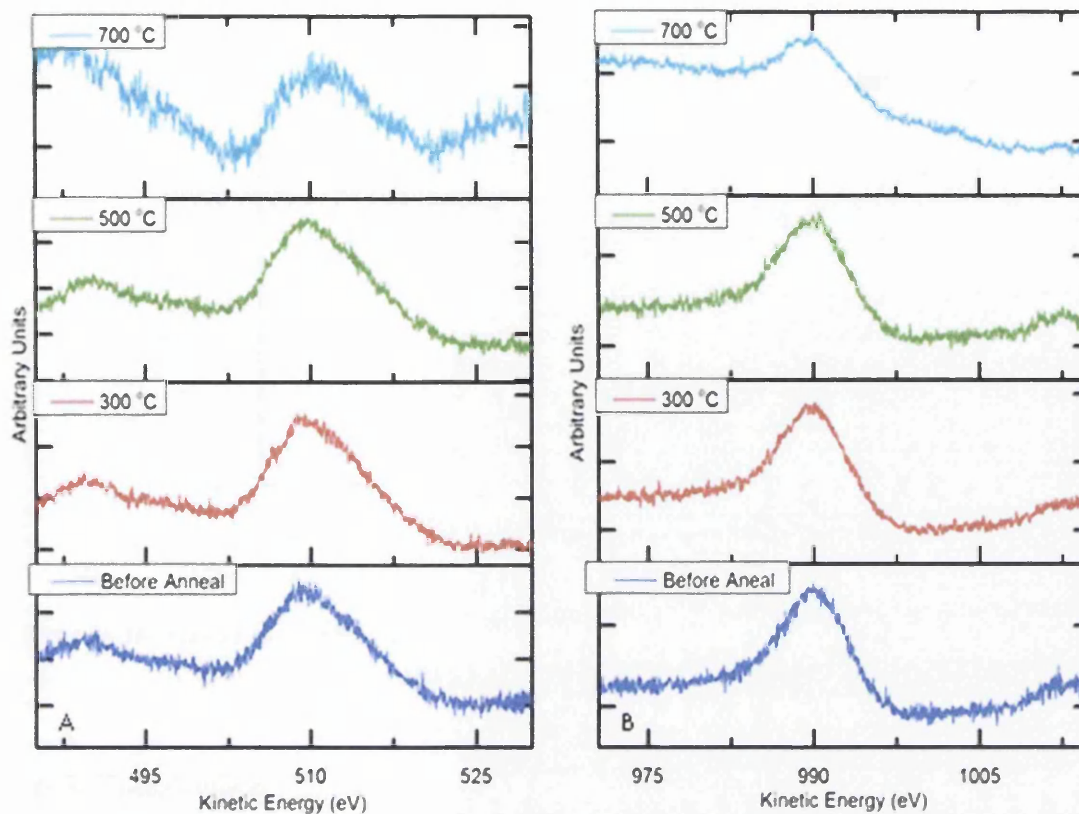

Figure 6.25: AES A) O LMM and B) Zn LMM spectra of ZnO nanosheets before and after vacuum annealing at 300 °C, 500 °C and 700 °C .

The average ratio of oxygen and zinc normalised to the average silicon peak intensity is plotted in Figure 6.26. This result shows the stoichiometry is retained when annealing up to 500 °C in vacuum with the Zn:O ratio bein ~3.2. However, annealing at 700 °C caused loss of stoichiometry with the Zn:O ratio increasing to 4.5. This supports the SEM image in Figure 6.22d that shows the partial disintegrated ZnO nanosheets at the same temperature.

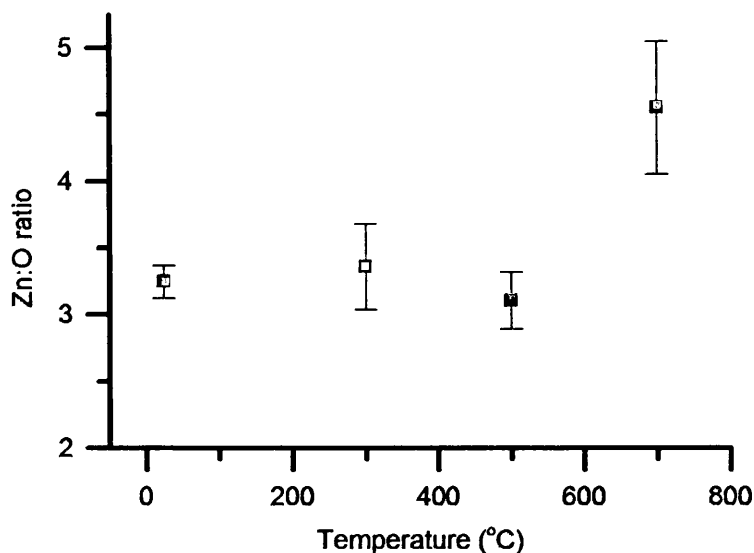

Figure 6.26: Zn:O ratio against annealing temperature. Error bars calculated using standard deviation.

6.6.3 Conclusion

ZnO nanosheets have been synthesised using a solution of zinc nitrate, HMTA and zinc acetate in a microwave. The nanosheets were then deposited on SiO. The nanosheets were annealed to 300 °C, 500 °C and 700 °C in vacuum and characterised before and after annealing using SEM, PL, AES and 2 point probe. It was found that annealing to 300 °C reduced the resistance which was caused by cleaning of surface contaminants and sintering of the grains which reduced the number of grain boundaries. However, it was also seen that there was a decrease in the donor defects and increase in the acceptor defects. Annealing to 500 °C caused further sintering of the grains but the resistance of the ZnO nanosheets increased. This was caused by a reduction in both the donor and acceptor defects. Annealing to 700 °C caused the nanosheets to partially disintegrate and appear black under SEM. AES revealed that stoichiometry between the zinc and oxygen was not conserved. It was also found that the resistance had increased. These results are similar to those found when annealing ZnO nanowires. The differences are mainly due the polycrystalline structure of the nanosheets which have a lower melting point. The nanosheets results do, however, support the conclusion from the nanowire experiment that annealing removed the zinc from the surface at high temperatures and changed the oxygen quantity at lower temperatures.

Chapter 7: Conclusions and Further Work

7.1 Conclusions

The overall aim of this dissertation was to obtain atomic resolution using STM and take local transport measurements on a ZnO nanowire. Short range atomic resolution was achieved on single crystal ZnO and near atomic resolution on a ZnO nanowire, also local transport measurements have led to some useful and interesting discoveries. The underlying method that has been followed was to clean ZnO nanowires using cycles of argon bombardment and annealing in a way similar to that used by Dulub et al. to obtain near atomic resolution on singe crystal ZnO using STM [15], local atomic resolution was also achieved on single crystal ZnO in this thesis. To achieve the final goal three main areas have been investigated, each of which has its own experimental chapter. The three areas included: improving the quality and reproducibility of STM by studying the effects of probe oxide; tailoring ZnO nanowires synthesis to grow suitable structures for STM; and modifying the recipe put forward by Dulub et al. to clean the nanowires and understand the effects of the treatment.

Chapter 4 reports on the experiments that were carried out involving direct current annealing of the STM tip to remove the native oxide. It was found that the native oxide can be reduced by direct current annealing. However, to remove all the oxide requires a temperature greater than 1714 K which causes the tip to blunt. It was therefore concluded that the best compromise was to anneal the tip to 1714 K or 7.5 A since annealing at 8 A or 2051 K did not significantly increase the tungsten to oxygen ratio but the radius of the tip increased from 32 nm to 40 nm.

The effects of reducing the native oxide on the STM probe on STS was also investigated by collecting STS spectra using a tip before cleaning on cleaved GaAs and after annealing to 1714 K. It was found that when a non-annealed STM tip is approached onto the sample the oxide at the apex of the tip is mechanically removed since the size of the oxide is too large to allow tunnelling. It was also found that oxide coating modifies the electric field at the end of the tip which changes the

induced quantum dot in the sample. When a large oxide sheath is present the induced quantum dot is larger and discrete energy levels in the VB exist above the Fermi level when the bias is high enough. This facilitates increased tunnelling currents for a given voltage compared to that measured when using a tip which has been annealed and the oxide coating reduced.

The STS experiment was repeated to investigate the effects of tip oxide on contact measurements. It was seen that a different mechanism occurs to that found when the tip was not in contact. In the contact case the Schottky barrier height becomes fixed, however, the shape of the barrier is affected by the probe oxide. Reducing the probe oxide results in less tip induced band bending which reduces the size of the depletion region and therefore reduces tunnelling current.

Chapter 5 covers experiments that investigate the effects of the growth parameters on ZnO nanowire synthesis. It was found that using heated water baths produces much longer nanowires than microwave growth. It was also found that increasing the ratio of zinc nitrate to HMTA produced nanowires which had larger diameters that were more tapered. It was also seen that the length of the nanowires was not affected by changes to the precursor ratio. The reason for the change in the diameter and taper is likely to be caused by increased concentration in Zn^{2+} which creates a bi layer at the top of the nanowires which causes an increase in growth in the diameter.

It was also found that growing for longer time periods results in nanowires that are longer. However, it was seen that there was no increase in length after 9 hours of synthesis. These two results were expected as the solution drops below saturation which will cause the growth to stop. This experiment also revealed that the growth seems to undergo a number of stages. For the first 4 hours the growth rate is linear and there is little change in the diameter of the nanowires. The nanowires then undergo a "growth spurt" during the 4-5 hour stage of growth when the length doubles and the diameter increases. After this stage the increase in length becomes linear again before trailing off while the diameter does not change significantly.

Chapter 5 also reported on an experiment in which a layer of metal was deposited before the seed layer. It was seen that the metal layer caused the ZnO seed layer to change in roughness. This resulted in a change in the morphology of the nanowires growth such that the nanowires grown on a rougher seed layer were longer and wider. This was in agreement with the findings of Brown et al. [14].

As expected, it was found that increasing the temperature of the growth solution increased the growth rate of the nanowires. It was also found that increasing the growth temperature from 70 °C to 75 °C increased the number of defects in the nanowires when measured with PL. Increasing the temperature further increases the size of the observed defect peak, however, this increase is caused by the increased size of the nanowires.

The final sets of experiments were based on modifying Dulub et al.'s recipe for cleaning ZnO single crystal. It was first found that using Dulub et al.'s recipe of cycles of 1.5 eV of argon bombardment and annealing at 900 °C did not cause the single crystal to reconstruct to produce a clear LEED pattern. Further experiments using a sample on nanowires rubbed onto a piece of silicon found that the temperature did not reach 600 °C. This experiment also showed that ZnO nanowires started to melt at 600 °C. Therefore Dulub et al.'s recipe was modified to using 600 °C instead of 900 °C.

A similar experiment was used to adjust the power of the argon bombardment. It was seen that using 1.5 eV caused a large amount of damage to the nanowires and that 0.5 eV also caused visible damage when viewed with SEM. However, using 0.3 eV did not damage the nanowires, therefore Dulub et al.'s recipe was modified again to use this value. Using this new recipe allowed a clear 2x1 LEED pattern to be seen. STM revealed that there was some order across the surface and it was possible to resolve features that matched the lattice parameter of ZnO when allowing for surface relaxation. As previously stated, repeating the recipe on ZnO nanowires did not result in atomic resolution when scanned with STM.

The argon bombardment and annealing experiments also provide some useful results relating to the electrical properties and understanding the defects. It was found that a light argon bombardment cleaned the surface of the nanowire and allowed a better contact which was seen to be three orders of magnitude lower. This light cleaning also decreased the standard deviation which suggests that the contact is more consistent. This is useful if the nanowires were to be included in a device. It was also seen that increased argon bombardment power removed the surface of the nanowires which increased the resistance. It is therefore concluded that the n-type defects that provide the charge carriers are mainly present in the surface of the nanowires. The annealing of the nanowires caused shifts in the defects present. Annealing caused interstitials to move to vacancies when annealing up to 600 °C. Annealing above 600 °C causes the surface of the nanowires to sublimate zinc which also removes the vacancies and increases the number of oxygen occupying a zinc site defects. This also suggests that the n-type defects are present only in the surface. This reduces the conductivity since the n-type defects are reduced and p-type defects are increased. Therefore it is possible to control the conductivity via controlling the defects with argon bombardment and heating.

The final experiment reported involved the annealing of a relatively new form of ZnO nanosheets. It was found using 2 point probe that annealing to 300 °C caused the resistance to drop in a similar manner to that seen with the nanowires. This is likely to be caused by a better contact due to cleaning the surface and removing contaminants. It was also seen that nanosheets melt at a lower temperature compared to nanowires due to the polycrystalline structure. It was also seen that annealing caused an increase in the p-type defects, again similar to that seen when annealing nanowires. Due to the melting and changing of the grain size it is difficult to conclude the exact reasons for the measured increase in resistance as the temperature of annealing increased.

7.2 Further Work

There are a number of experiments that should be carried out relating to the work presented in this dissertation. Work should be undertaken to improve the recipe to

achieve a better STM scan of ZnO nanowires and obtain a result similar to that of the single crystal STM scan. It is possible that the annealing was carried out at the wrong temperature. The only feasible way to assess this is to carry out a trial and error approach to modify the recipe. It is also worth considering trying the cleaning recipe on ZnO nanowires synthesised using other growth methods such as CVD or electro chemical.

It would also be interesting to use CVD grown nanowires in the argon bombardment and annealing experiment. The defect chemistry of CVD grown ZnO nanowires is different from that of aqueously grown ZnO nanowires [140]. CVD grown nanowires have a defect band in which the main peaks are much lower in wavelength than aqueously grown nanowires. This suggests that they are more p-type in nature. However, it is not known whether these defects are situated on the surface as was seen with the aqueously grown nanowires. Argon bombardment and removing the surface will assess the location of the defect within the structure of the nanowire.

A further area of research that will become more prominent over the coming years will be the study of ZnO nanosheets. An annealing experiment has been carried out as part of this dissertation. However, a study should be carried out using argon bombardment. If it follows a similar trend to the nanowires then a light argon bombardment may improve contacts to the nanosheets. This will help nanosheets to be incorporated into devices such as gas sensors without issues surrounding contact to the interdigitated substrate. Work should also be carried out to further the work undertaken on annealing ZnO nanosheets. Gas sensors rely on heating the sensing material to temperatures of up to 400 °C. It was seen that annealing causing changes to the polycrystalline structure. Therefore studies should be expanded to understand the effects of annealing at this temperature both in vacuum and in an air environment. This may allow tailoring of the ZnO nanosheets' electric properties to better suit the device that they are being used in.

There are many experiments involving the growth of ZnO nanowires that can be carried out. This dissertation has explored some of the variables involved in growing ZnO nanowires, however, there are more that can be investigated such as seed layer

thickness and material. This work already exists in the literature in some form or another. Work to further the time experiment could give further insight and provide useful results. It was seen that little growth occurs over the first hour of synthesis. The experiment should be repeated with a sample removed every 10 minutes for the first 2 hours. This is to provide more detail about the nucleation stage of growth and when it occurs. This should also be repeated over the 4-5 hour period to investigate the growth spurt that was observed.

One of the issues involving aqueous growth is that the nanowires are relatively short compared to those synthesised using CVD. Using the results from the time experiment results, it may be possible to grow longer nanowires by refreshing the solution. An experiment should be carried out where nanowires are synthesised for 4 hours then placed into another solution that has been used for growth for 1 hour. This should cause the nanowires to grow longer without the transition junction in nanowires that was seen when just using a new solution as the diameters should be matched.

References

1. Schmidt-Mende, L. and J.L. MacManus-Driscoll, *ZnO - nanostructures, defects, and devices.* Materials Today, 2007. **10**(5): p. 40-48.
2. Cheng, H., et al., *Large-scale fabrication of ZnO micro-and nano-structures by microwave thermal evaporation deposition.* Journal of Crystal Growth, 2007. **299**(1): p. 34-40.
3. Lord, A.M., et al., *Factors that determine and limit the resistivity of high-quality individual ZnO nanowires.* Nanotechnology, 2013. **24**(43): p. 435706.
4. Herrera-Zaldıvar, M., J. Valenzuela-Benavides, and U. Pal, *STM and STS characterization of ZnO nanorods.* Optical Materials, 2008. **27**: p. 1276-1280.
5. Maffeis, T.G.G., et al., *STM–STS investigation of vacuum annealed ZnO nanoribbons.* physica status solidi (a), 2010. **207**(2): p. 282-285.
6. Cricenti, A., et al., *PREPARATION AND CHARACTERIZATION OF TUNGSTEN TIPS FOR SCANNING-TUNNELING-MICROSCOPY.* Review of Scientific Instruments, 1994. **65**(5): p. 1558-1560.
7. Albrektsen, O., et al., *RELIABLE TIP PREPARATION FOR HIGH-RESOLUTION SCANNING-TUNNELING-MICROSCOPY.* Journal of Vacuum Science & Technology B, 1994. **12**(6): p. 3187-3190.
8. Lucier, A.S., et al., *Determination of the atomic structure of scanning probe microscopy tungsten tips by field ion microscopy.* Physical Review B, 2005. **72**(23).
9. Staufer, U., et al., *INVESTIGATION OF EMITTER TIPS FOR SCANNING TUNNELING MICROSCOPE-BASED MICROPROBE SYSTEMS.* Journal of Vacuum Science & Technology B, 1991. **9**(6): p. 2962-2966.
10. Ding, H.F., et al., *Electron-beam tip/sample heating device for a scanning tunneling microscopy.* Review of Scientific Instruments, 2005. **76**(12).
11. Yu, Z.Q., et al., *Reproducible tip fabrication and cleaning for UHVSTM.* Ultramicroscopy, 2008. **108**(9): p. 873-877.
12. Kryvchenkova, O., *Transport simulations of ZnO nanowires and semiconductor devices in*

the presence of scanning probes, in *College of Engineering*. 2015, Swansea University: Swansea.

13. Sugunan, A., et al., *Zinc oxide nanowires in chemical bath on seeded substrates: Role of hexamine.* J Sol-Gel Sci Techn, 2006. **39**: p. 49-56.
14. Brown, R., et al., *The effect of metal layers on the morphology and optical properties of hydrothermally grown zinc oxide nanowires.* Journal of Materials Science, 2013. **48**(14): p. 4908-4913.
15. Dulub, O., L.A. Boatner, and U. Diebold, *STM study of the geometric and electronic structure of ZnO(0001)-Zn, (000-1)-O, (10-10), and (11-20) surfaces.* Surface Science, 2002. **519**: p. 201-217.
16. Binnig, G. and H. Rohrer, *Scanning tunneling microscopy (Reprinted from IBM Journal of Research and development, vol 30, 1986).* Ibm Journal of Research and Development, 2000. **44**(1-2): p. 279-293.
17. Nuffer, R., H.J. Mussig, and J. Dabrowski, *Cross-sectional STM/STS - a useful tool for identification of dopants in silicon.* Solid-State Electronics, 2000. **44**(5): p. 875-880.
18. Baski, A.A., S.C. Erwin, and L.J. Whitman, *The structure of silicon surfaces from (001) to (111).* Surface Science, 1997. **392**(1-3): p. 69-85.
19. Depuydt, A., et al., *Scanning tunneling microscopy and spectroscopy at low temperatures of the (110) surface of Te-doped GaAs single crystals.* Physical Review B, 1999. **60**(4): p. 2619-2626.
20. Feenstra, R.M., et al., *Low-temperature scanning tunneling spectroscopy of n-type GaAs(110) surfaces.* Physical Review B, 2002. **66**(16).

21. Tiwari, S. and S.L. Wright, *MATERIAL PROPERTIES OF P-TYPE GAAS AT LARGE DOPINGS.* Applied Physics Letters, 1990. **56**(6): p. 563-565.
22. Gaan, S., et al., *Structure and electronic spectroscopy of steps on GaAs(110) surfaces.* Surface Science, 2012. **606**(1-2): p. 28-33.
23. Ibe, J.P., et al., *ON THE ELECTROCHEMICAL ETCHING OF TIPS FOR SCANNING TUNNELING MICROSCOPY.* Journal of Vacuum Science & Technology a-Vacuum Surfaces and Films, 1990. **8**(4): p. 3570-3575.
24. Gimzewski, J.K. and R. Möller, *Transition from the tunneling regime to point contact studied using scanning tunneling microscopy.* Physical Review B, 1987. **36**(2): p. 1284-1287.
25. Bartels, L., G. Meyer, and K.H. Rieder, *High-resolution spectroscopy of weakly chemisorbed species using a low-temperature scanning tunneling microscope (STM): CO/Cu(III).* Chemical Physics Letters, 1998. **297**(3-4): p. 287-292.
26. Shen, J., et al., *Scanning tunneling microscopy/spectroscopy study of atomic and electronic structures of In2O on InAs and In0.53Ga0.47As(001)-(4X2) surfaces.* Journal of Chemical Physics, 2010. **133**(16).
27. Clemens, J.B., et al., *Atomic imaging of the monolayer nucleation and unpinning of a compound semiconductor surface during atomic layer deposition.* Journal of Chemical Physics, 2010. **133**(15).
28. Bode, M., *Spin-polarized scanning tunnelling microscopy.* Reports on Progress in Physics, 2003. **66**(4): p. 523-582.
29. Kim, H.S., et al., *OXYGEN PROCESSED FIELD-EMISSION TIPS FOR MICROCOLUMN APPLICATIONS.* Journal of Vacuum Science & Technology B, 1993. **11**(6): p. 2327-2331.
30. Ishida, N., et al., *Holders for in situ treatments of scanning tunneling microscopy tips.* Review of Scientific Instruments, 2009. **80**(9).
31. Ciraci, S., A. Baratoff, and I.P. Batra, *TIP-SAMPLE INTERACTION EFFECTS IN SCANNING-TUNNELING AND ATOMIC-FORCE MICROSCOPY.* Physical Review B, 1990. **41**(5): p. 2763-2775.
32. Dombrowski, R., et al., *Tip-induced band bending by scanning tunneling spectroscopy of the states of the tip-induced quantum dot on InAs(110).* Physical Review B, 1999. **59**(12): p. 8043-8048.
33. Ke, S.H., T. Uda, and K. Terakura, *First-principles studies of tip-sample interaction and STM-AFM image formation on TiO2(110)-1x1 and TiO2(110)-1x2 surfaces.* Physical Review B, 2002. **65**(12).
34. Ke, S.H., et al., *First-principles investigation of tip-surface interaction on a GaAs(110) surface: Implications for atomic force and scanning tunneling microscopies.* Physical Review B, 1999. **60**(16): p. 11631-11638.
35. Wright, C.A. and S.D. Solares, *Computational study of tip apex symmetry characterization in high-resolution atomic force microscopy.* Journal of Physics D-Applied Physics, 2013. **46**(15).
36. Mashoff, T., et al., *Bistability and Oscillatory Motion of Natural Nanomembranes Appearing within Monolayer Graphene on Silicon Dioxide.* Nano Letters, 2010. **10**(2): p. 461-465.
37. Petersen, C.L., et al., *Scanning microscopic four-point conductivity probes.* Sensors and Actuators a-Physical, 2002. **96**(1): p. 53-58.
38. Li, P.-J., et al., *Electrical and Photoresponse Properties of an Intramolecular p-n Homojunction in Single Phosphorus-Doped ZnO Nanowires.* Nano Letters, 2009. **9**(7): p. 2513-2518.
39. Jacobs, K., et al., *Low-temperature chemical bath deposition of crystalline ZnO.* Solid State Sciences, 2010. **12**(3): p. 333-338.

40. Valtiner, M., S. Borodin, and G. Grundmeier, *Preparation and characterisation of hydroxide stabilised ZnO(0001)-Zn-OH surfaces.* Physical Chemistry Chemical Physics, 2007. **9**(19): p. 2406-2412.
41. Zwicker, G. and K. Jacobi, *SITE-SPECIFIC INTERACTION OF H2O WITH ZNO SINGLE-CRYSTAL SURFACES STUDIED BY THERMAL-DESORPTION AND UV PHOTOELECTRON-SPECTROSCOPY.* Surface Science, 1983. **131**(1): p. 179-194.
42. Parker, T.M., et al., *Imaging the polar (000-1) and non-polar (10-10) surfaces of ZnO with STM.* Surface Science Letters, 1998. **415**: p. 563-569.
43. Ericsson, L.K.E. and K.O. Magnusson, *ZnO nanocrystals on SiO2 /Si surfaces thermally cleaned in ultrahigh vacuum and characterized using spectroscopic photoemission and low energy electron microscopy.* J. Vac. Sci. Technol. A, 2010. **28**(3): p. 438-442.
44. Maffeïs, T.G.G., et al., *Atomic force microscopy and scanning tunneling microscopy-spectroscopy characterization of ZnO nanobelts.* J. Vac. Sci. Technol. B, 2008. **26**(4): p. 1606-1608.
45. Wang, Z.L., *Nanobelts, Nanowires, and Nanodiskettes of Semiconducting Oxides—From Materials to Nanodevices.* Advanced Materials, 2003. **15**(5): p. 432-436.
46. Tarat, A., et al. *Nanocrystalline ZnO obtained from pyrolytic decomposition of layered basic zinc acetate: Comparison between conventional and microwave oven growth.* in *Nanotechnology (IEEE-NANO), 2012 12th IEEE Conference on.* 2012.
47. Huang, M.H., et al., *Room-temperature ultraviolet nanowire nanolasers.* Science, 2001. **292**(5523): p. 1897-1899.
48. Tong, H., B.-L. Wang, and Z.-C. Ou-Yang, *Electric potential generated in ZnO nanowire due to piezoelectric effect.* Thin Solid Films, 2008. **516**(9): p. 2708-2710.
49. Wang, Z.L. and J.H. Song, *Piezoelectric nanogenerators based on zinc oxide nanowire arrays.* Science, 2006. **312**(5771): p. 242-246.
50. Wagner, R.S. and W.C. Ellis, *VAPOR-LIQUID-SOLID MECHANISM OF SINGLE CRYSTAL GROWTH.* APPLIED PHYSICS LETTERS, 1964. **4**(5): p. 89-90.
51. Ramgir, N.S., I.S. Mulla, and V.K. Pillai, *Micropencils and Microhexagonal Cones of ZnO.* The Journal of Physical Chemistry B, 2006. **110**(9): p. 3995-4001.
52. Huang, M.H., et al., *Catalytic Growth of Zinc Oxide Nanowires by Vapor Transport.* Advanced Materials, 2001. **13**(2): p. 113-116.
53. Greyson, E.C., Y. Babayan, and T.W. Odom, *Directed Growth of Ordered Arrays of Small-Diameter ZnO Nanowires.* Advanced Materials, 2004. **16**(15): p. 1348-1352.
54. Jie, J., et al., *Synthesis and optical properties of well-aligned ZnO nanorod array on an undoped ZnO film.* APPLIED PHYSICS LETTERS, 2005. **86**(3): p. -.
55. Verges, M.A., A. Mifsud, and C.J. Serna, *Formation of rod-like zinc oxide microcrystals in homogeneous solutions.* Journal of the Chemical Society, Faraday Transactions, 1990. **86**(6): p. 959-963.
56. Vayssieres, L., et al., *Purpose-Built Anisotropic Metal Oxide Material: 3D Highly Oriented Microrod Array of ZnO.* The Journal of Physical Chemistry B, 2001. **105**(17): p. 3350-3352.
57. McPeak, K.M., et al., *Chemical Bath Deposition of ZnO Nanowires at Near-Neutral pH Conditions without Hexamethylenetetramine (HMTA): Understanding the Role of HMTA in ZnO Nanowire Growth.* Langmuir, 2011. **27**(7): p. 3672-3677.
58. Sun, Y., D.J. Riley, and M.N.R. Ashfold, *Mechanism of ZnO Nanotube Growth by Hydrothermal Methods on ZnO Film-Coated Si Substrates.* The Journal of Physical Chemistry B, 2006. **110**(31): p. 15186-15192.
59. Greene, L.E., et al., *Solution-Grown Zinc Oxide Nanowires.* Inorganic Chemistry, 2006. **45**(19): p. 7535-7543.

60. Song, J. and S. Lim, *Effect of Seed Layer on the Growth of ZnO Nanorods.* The Journal of Physical Chemistry C, 2006. **111**(2): p. 596-600.
61. Unalan, H.E., et al., *Rapid synthesis of aligned zinc oxide nanowires.* Nanotechnology, 2008. **19**(25).
62. Lin, C.C., H.P. Chen, and S.Y. Chen, *Synthesis and optoelectronic properties of arrayed p-type ZnO nanorods grown on ZnO film/Si wafer in aqueous solutions.* Chemical Physics Letters, 2005. **404**(1-3): p. 30-34.
63. Brahma, S., et al., *Low temperature and rapid deposition of ZnO nanorods on Si(100) substrate with tunable optical emissions.* Materials Chemistry and Physics, 2013. **140**(2–3): p. 634-642.
64. McCluskey, M.D. and S.J. Jokela, *Defects in ZnO.* Journal of Applied Physics, 2009. **106**(7): p. -.
65. Liu, J., et al., *Tailoring the visible photoluminescence of mass-produced ZnO nanowires.* Journal of Physics D: Applied Physics, 2009. **42**(9): p. 095401.
66. Lin, B., Z. Fu, and Y. Jia, *Green luminescent center in undoped zinc oxide films deposited on silicon substrates.* APPLIED PHYSICS LETTERS, 2001. **79**(7): p. 943-945.
67. Xu, P.S., et al., *The electronic structure and spectral properties of ZnO and its defects.* Nuclear Instruments and Methods in Physics Research Section B: Beam Interactions with Materials and Atoms, 2003. **199**(0): p. 286-290.
68. Wei, X.Q., et al., *Blue luminescent centers and microstructural evaluation by XPS and Raman in ZnO thin films annealed in vacuum, N2 and O2.* Physica B: Condensed Matter, 2007. **388**(1–2): p. 145-152.
69. Liao, Z.-M., et al., *Surface effects on photoluminescence of single ZnO nanowires.* Physics Letters A, 2008. **372**(24): p. 4505-4509.
70. Nikitenko, V., *Optics and Spectroscopy of Point Defects in ZnO*, in *Zinc Oxide — A Material for Micro- and Optoelectronic Applications*, N. Nickel and E. Terukov, Editors. 2005, Springer Netherlands. p. 69-81.
71. Lima, S.A.M., et al., *Luminescent properties and lattice defects correlation on zinc oxide.* International Journal of Inorganic Materials, 2001. **3**(7): p. 749-754.
72. Yang, Y., et al., *Photoluminescence and Raman studies of electrochemically as-grown and annealed ZnO films.* Solid State Communications, 2006. **138**(10–11): p. 521-525.
73. Heo, Y.W., D.P. Norton, and S.J. Pearton, *Origin of green luminescence in ZnO thin film grown by molecular-beam epitaxy.* Journal of Applied Physics, 2005. **98**(7): p. 073502.
74. Janotti, A. and C.G. Van de Walle, *Oxygen vacancies in ZnO.* APPLIED PHYSICS LETTERS, 2005. **87**(12): p. -.
75. Van de Walle, C.G., *Hydrogen as a Cause of Doping in Zinc Oxide.* Physical review letters, 2000. **85**(5): p. 1012-1015.
76. Can, M.M., et al., *Electrical and optical properties of point defects in ZnO thin films.* Journal of Physics D: Applied Physics, 2012. **45**(19): p. 195104.
77. Ra, H.W., et al., *Effects of surface modification of the individual ZnO nanowire with oxygen plasma treatment.* Materials Letters, 2009. **63**(28): p. 2516-2519.
78. Ra, H.-W., et al., *Ion bombardment effects on ZnO nanowires during plasma treatment.* APPLIED PHYSICS LETTERS, 2008. **93**(3): p. -.
79. Knutsen, K.E., et al., *Zinc vacancy and oxygen interstitial in ZnO revealed by sequential annealing and electron irradiation.* Physical Review B, 2012. **86**(12): p. 121203.
80. Ra, H.-W. and Y.-H. Im, *Effect of chemically reactive species on properties of ZnO nanowires exposed to oxygen and hydrogen plasma.* Nanotechnology, 2008. **19**(48): p. 485710.

81. Law, J.B.K. and J.T.L. Thong, *Improving the NH 3 gas sensitivity of ZnO nanowire sensors by reducing the carrier concentration.* Nanotechnology, 2008. **19**(20): p. 205502.
82. Ha, B., H. Ham, and C.J. Lee, *Photoluminescence of ZnO nanowires dependent on O2 and Ar annealing.* Journal of Physics and Chemistry of Solids, 2008. **69**(10): p. 2453-2456.
83. Banerjee, D., et al., *Synthesis and photoluminescence studies on ZnO nanowires.* Nanotechnology, 2004. **15**(3): p. 404.
84. Cross, R.B.M., M.M.D. Souza, and E.M.S. Narayanan, *A low temperature combination method for the production of ZnO nanowires.* Nanotechnology, 2005. **16**(10): p. 2188.
85. Hu, J.Q., et al., *Two-dimensional micrometer-sized single-crystalline ZnO thin nanosheets.* APPLIED PHYSICS LETTERS, 2003. **83**(21): p. 4414-4416.
86. Bai, W., et al., *Synthesis of zinc oxide nanosheet thin films and their improved field emission and photoluminescence properties by annealing processing.* Applied Surface Science, 2008. **254**(20): p. 6483-6488.
87. Tarat, A., et al., *Microwave-assisted synthesis of layered basic zinc acetate nanosheets and their thermal decomposition into nanocrystalline ZnO.* Nanoscale Research Letters, 2014. **9**(1): p. 11.
88. Stroscio, J.A. and W.J. Kaiser, *Scanning Tunneling Microscopy.* Methods of Experimental Physics. Vol. 27. 1993, San Diego: Academic Press INC.
89. *The Nobel Prize in Physics 1986.* 2014 [cited 2014 31st August]; Available from: http://www.nobelprize.org/nobel_prizes/physics/laureates/1986/.
90. Weiming, L., *Scanning tunneling microscopy and spectroscopy simulations of the silicon (111)-(7x7) surface*, in *Department of Physics.* 2007, University of Lethbridge: Atlanta.
91. Bonnell, D., *Scannign Probe Microscopy and Spectroscopy.* 2000, USA: Wiley-VCH.
92. Tang, C.L., *Fundamentals of Quantum Mechanics: For Solid State Electronics and Optics.* 2005: Cambridge University Press.
93. Pavesi, L., S. Gaponenko, and L.D. Negro, *Towards the First Silicon Laser.* 2012: Springer Netherlands.
94. Kittel, C., *Introduction to Solid State Physics.* 2004: Wiley.
95. Kuno, M., *Introductory Nanoscience Physical and Chemical Concepts.* 2012, New York: Garland Science
96. Feenstra, R.M., J.A. Stroscio, and A.P. Fein, *Tunneling spectroscopy of the Si(111)2 × 1 surface.* Surface Science Letters, 1987. **181**(1–2): p. A96.
97. Scienta, V. *Ion Gauges.* [cited 2014 23rd August]; Available from: http://www.vgscienta.com/productlist.aspx?MID=227.
98. Pendry, J.B., *Low Energy Electron Diffraction.* 1974, London: Academic Press.
99. High-Tech, H., *Let's Familiarize Ourselves with the SEM!* 2009.
100. Fadley, C.S., *Electron Spectroscopy: Theory, Techniques and Applications, Vol. 2*, ed. C.R. Brundle and A.D. Baker. Vol. 2. 1978: Academic Press.
101. Feibelman, P.J. and D.E. Eastman, *Photoemission spectroscopy—Correspondence between quantum theory and experimental phenomenology.* Physical Review B, 1974. **10**(12): p. 4932-4947.
102. Mahan, G.D., *Theory of Photoemission in Simple Metals.* Physical Review B, 1970. **2**(11): p. 4334-4350.
103. Plummer, E.W. and W. Eberhardt, *Angle-Resolved Photoemission as a Tool for the Study of Surfaces*, in *Advances in Chemical Physics.* 2007, John Wiley & Sons, Inc. p. 533-656.

104. Cohen-Tannoudji, C., B. Dui, and F. Laloë, *Quantum Mechanics, Vol. 2*. Vol. 2. 1977: J. Wiley & Sons
105. *Practical Surface Analysis, 2nd Edition, Volume 1 Auger and x-ray Photoelectron Spectroscopy*, ed. D. Briggs and M.P. Seah. Vol. 1. 1990: J. Wiley & Sons
106. Yeh, J.J. and I. Lindau, *Atomic Data and Nuclear Tables*. 1985(32): p. 1.
107. Carlson, T.A., *Photoelectron and Auger Spectroscopy*. 1976, New York Plenum.
108. Cobley, R.J., et al., *Quantitative analysis of annealed scanning probe tips using energy dispersive x-ray spectroscopy*. Applied Physics Letters, 2013. **102**(2).
109. Barnett, C.J., et al., *The role of probe oxide in local surface conductivity measurements*. Journal of Applied Physics, 2015. **117**(17): p. 174306.
110. Kryvchenkova, O., R.J. Cobley, and K. Kalna, *Self-consistent modelling of tunnelling spectroscopy on III–V semiconductors*. Applied Surface Science, 2014. **295**(0): p. 173-179.
111. *ATLAS User's Manual*. 2007.
112. Tsu, R. and L. Esaki, *TUNNELING IN A FINITE SUPERLATTICE*. Applied Physics Letters, 1973. **22**(11): p. 562-564.
113. Price, P. and J. Radcliffe, *Esaki tunneling*. Ibm Journal of Research and Development, 1959. **3**(4): p. 364-371.
114. Gundlach, K.H., *Zur berechnung des tunnelstroms durch eine trapezförmige potentialstufe*. Solid-State Electronics, 1966. **9**(10): p. 949-957.
115. Ferry, D.K., *Semiconductors*. 1991: Macmillan.
116. Rideout, V.L. and C.R. Crowell, *EFFECTS OF IMAGE FORCE AND TUNNELING ON CURRENT TRANSPORT IN METAL-SEMICONDUCTOR (SCHOTTKY-BARRIER) CONTACTS*. Solid-State Electronics, 1970. **13**(7): p. 993-&.
117. Matsuzawa, K., K. Uchida, and A. Nishiyama, *A unified simulation of Schottky and ohmic contacts*. Ieee Transactions on Electron Devices, 2000. **47**(1): p. 103-108.
118. Ieong, M., et al., *Comparison of raised and Schottky source/drain MOSFETs using a novel tunneling contact model*, in *International Electron Devices Meeting 1998 - Technical Digest*. 1998. p. 733-736.
119. Barnett, C.J., *Characterization of ZnO nanowires treated with non-thermal plasma using SEM, XPS, PL and AFM* in *College of Engineering*. 2011, Swansea University: Swansea.
120. Barnett, C.J., et al. *Investigation into the initial growth parameters of hydrothermally grown zinc oxide nanowires*. in *Nanotechnology (IEEE-NANO), 2012 12th IEEE Conference on*. 2012.
121. Brown, R.A., et al. *The viability of U-2 OS cells on Zinc Oxide nanowires observed via MTS assay in vitro*. in *Nanotechnology (IEEE-NANO), 2012 12th IEEE Conference on*. 2012.
122. Sugunan, A., et al., *Zinc oxide nanowires in chemical bath on seeded substrates: Role of hexamine*. Journal of Sol-Gel Science and Technology, 2006. **39**(1): p. 49-56.
123. Xu, S. and Z.L. Wang, *One-Dimensional ZnO Nanostructures: Solution Growth and Functional Properties*. Nano Research, 2011: p. 1-86.
124. Kim, H.-K., et al., *Electrical and Interfacial Properties of Nonalloyed Ti/Au Ohmic and Pt Schottky Contacts on Zn-Terminated ZnO*. Japanese Journal of Applied Physics, 2006. **45**(3R): p. 1560.
125. Evans, J.E., *Growth and Functionalisation of Zinc Oxide Nanowires for Biosensing Applications*, in *College of Engineering*. 2015, Swansea University: Swansea.
126. Barnett, C., et al., *Effects of Vacuum Annealing on the Conduction Characteristics of ZnO Nanosheets*. Nanoscale Research Letters, 2015. **10**(1): p. 1-6.
127. Barnett, C.J., et al., *The effects of surface stripping ZnO nanorods with argon bombardment*. Nanotechnology, 2015. **26**(41): p. 415701.

128. Smith, N.A., et al., *Forming reproducible non-lithographic nanocontacts to assess the effect of contact compressive strain in nanomaterials.* Semiconductor Science and Technology, 2015.
129. Liao, L., et al., *Tunable transport properties of n-type ZnO nanowires by Ti plasma immersion ion implantation.* Journal of Applied Physics, 2008. **104**(7).
130. Lord, A.M., et al., *Controlling the Electrical Transport Properties of Nanocontacts to Nanowires.* Nano Letters, 2015.
131. Kryvchenkova, O., K. Kalna, and R.J. Cobley. *Modelling heating effects due to current crowding in ZnO nanowires with end-bonded metal contacts.* in *Advanced Semiconductor Devices & Microsystems (ASDAM), 2014 10th International Conference on.* 2014.
132. Kryvchenkova, O., K. Kalna, and R.J. Cobley. *The Current Crowding Effect in ZnO Nanowires with an End-Bonded Metal Contact.* in *Conference on Advanced Nanomaterials (ANM 2014).* 2014.
133. Xu, C., J. Chun, and D.E. Kimb, *Electrical properties and near band edge emission of Bi-doped ZnO nanowires.* APPLIED PHYSICS LETTERS, 2007. **90**(083113): p. 1-3.
134. Babikier, M., et al., *Effect of annealing on lattice strain and near-band-edge emission of ZnO nanorods.* Electronic Materials Letters, 2014. **10**(4): p. 749-752.
135. Jagadish, C. and S.J. Pearton, *Zinc Oxide Bulk, Thin Films and Nanostructures: Processing, Properties, and Applications.* 2011: Elsevier Science.
136. Boehler, R. and M. Ross, *Melting curve of aluminum in a diamond cell to 0.8 Mbar: implications for iron.* Earth and Planetary Science Letters, 1997. **153**(3–4): p. 223-227.
137. Hanstrom, A. and P. Lazor, *High pressure melting and equation of state of aluminium.* Journal of Alloys and Compounds, 2000. **305**(1): p. 209-215.
138. Mayadas, A.F. and M. Shatzkes, *Electrical-Resistivity Model for Polycrystalline Films: the Case of Arbitrary Reflection at External Surfaces.* Physical Review B, 1970. **1**(4): p. 1382-1389.
139. Maffeis, T.G.G., et al., *XPS investigation of vacuum annealed vertically aligned ultralong ZnO nanowires.* Surface Science, 2012. **606**(1–2): p. 99-103.
140. Lee, C.Y., et al., *Growth of Zinc Oxide Nanowires on Silicon (100).* Journal of Science and Engineering, 2003. **6**(2): p. 127-132.